Search for Weakly-interacting, Long-lived particles that Decay to Displaced Hadronic Jets in Proton-Proton Collisions at $\sqrt{s} = 8$ TeV with the ATLAS Detector.

Daniel Blackburn

A dissertation submitted in partial fulfillment of the
requirements for the degree of

Doctor of Philosophy

University of Washington

2015

Reading Committee:

Henry Lubatti, Chair

Stephen Ellis

Gordon Watts

Program Authorized to Offer Degree:
Department of Physics

University of Washington

Abstract

Search for Weakly-interacting, Long-lived particles that Decay to Displaced Hadronic Jets in Proton-Proton Collisions at $\sqrt{s} = 8$ TeV with the ATLAS Detector.

Daniel Blackburn

Chair of the Supervisory Committee:
Professor Henry Lubatti
Department of Physics

A search is presented for the decay of the Standard Model Higgs boson or another scalar boson to a pair of weakly-interacting, long-lived particles in 20.3 fb^{-1} of proton-proton collisions at $\sqrt{s} = 8$ TeV recorded in 2012 by the ATLAS detector. The strategy requires that one of the long-lived particles decay inside the muon spectrometer. The second long-lived particle is required to decay in the inner detector or the muon spectrometer. No excess of events is observed above the expected background. Limits are derived on the scalar boson's production cross section times branching ratio as a function of the long-lived particle's proper decay length.

TABLE OF CONTENTS

LIST OF FIGURES

LIST OF TABLES

ACKNOWLEDGMENTS

I would like to express my gratitude to the many people who have helped me to complete my degree. My advisor, Henry Lubatti, has guided me with endless patience. Thanks to the many ATLAS physicists who helped me to be a better student, including: Ben Brau, Andrea Coccaro, Preema Pais, Rachel Rosten, Heather Russell, Dan Ventura, and Gordon Watts.

Having spent my life until now as a student, I am indebted to an interminable list of teachers. Naming only a few of the many who influenced me for the better: Sue Cronkhite, Donna Leininger, Jeff Berndt, John Verkade, Hector Avalos, and Jim Cochran.

Thanks to my family and friends: My parents, who have always provided me the encouragement and resources to pursue my interests. Ashlea, who has been a great inspiration in my life and who has put up with me at my worst.

Introduction

The goal of high-energy physics study is to understand the nature of the elementary particles that compose our empirical universe. The particles and their interactions are described by the *Standard Model*, originally formulated in the 1970's. It describes the elementary particles of matter - quarks and leptons - and three of the four classical forces of nature - electromagnetic, weak, and strong.

Although experimental results show that particles have mass, the Standard Model's Lagrangian cannot contain explicitly written mass terms. To circumvent this, the Higgs mechanism was proposed to give fundamental particles mass through electroweak symmetry breaking. A particle corresponding to this mechanism, called the Higgs boson, was discovered in 2012 by the experimental collaborations ATLAS and CMS. The discovered Higgs boson currently has properties that are consistent with those predicted by the Standard Model, although the uncertainty is large. More precise measurements may yield deviations from expectation and show that there is new physics that is not described adequately by the Standard Model. In fact, uncertainties on the current measurements allow for the Higgs to decay to new particles with a branching ratio of up to 30% [4]. One possibility, which is explored here, is that the Higgs boson decays with some probability to new particles that are long-lived and travel a few meters before decaying within the detector.

This thesis presents a search for long-lived neutral particles that decay to hadronic jets using data collected by the ATLAS detector in 2012. Long-lived neutral particles that decay in the ATLAS detector provide a unique physics signature. The charged tracks that the detector sees will originate some displaced distance from the point of proton collision, with the charged tracks coming from a common vertex position. Vertex reconstruction algorithms were designed for this purpose that can identify displaced decays in ATLAS' inner detector and muon spectrometer. The search presented here looks for proton collision events with two such displaced vertices. Events that have two displaced vertices should be very rare in a Standard Model world, but could be frequently observed in worlds that have physics that goes beyond the Standard Model.

The following is a description of this thesis' structure. The first chapter introduces the theory

of the Standard Model, details about proton-proton collisions, and a benchmark model that extends the standard model, containing long-lived neutral particles. The second chapter describes the Large Hadron Collider and ATLAS detector. Chapter 3 gives information on how collision simulation is performed. Chapter 4 describes the signatures of long-lived particles and the number of such signatures expected in a hypothesis with a long-lived particle signature. Chapter 5 gives the estimated background rate of long-lived particle signatures in the hypothesis of no long-lived particle signature. Chapter 6 reports limits on long-lived particle signatures based on measurements made from data.

Chapter 1

THEORETICAL BACKGROUND

This chapter introduces the Standard Model, a theory that accounts for the known particles and their interactions. Some details about how particles interact and are measured in hadron coliders is presented. The shortcomings of the Standard Model will be discussed, and other theories that extend beyond the Standard Model will be introduced, including Hidden Valley theories. Finally, a search method for a particular Hidden Valley model is outlined.

1.1 The Standard Model

The Standard Model (SM) is currently the best description of the universe at the level of fundamental particles. It is a mathematical description of the elementary particles that make up the material world and the forces by which particles interact. The SM was formulated during the 1970s to describe the particles and interactions that have been observed. Since its formulation, the SM's usefulness has been corroborated by the discovery of the top quark, tau neutrino, and Higgs boson. With the exception of neutrino oscillation and mass[1], no statistically significant experimental observations contradict SM predictions.

1.1.1 The particle content of the Standard Model

The particles of the standard model can be divided into spin-1/2 fermions, which are the particles of matter, gauge bosons, which mediate the forces, and a scalar boson, which is an excitation of the scalar field that gives fundamental particles their mass. The matter particles come in two classes,

[1]The SM incorrectly assumes that neutrinos are massless, but this is not a major failing of the SM. Neutrinos' mass is incredibly small, less than ~ 1 eV. The SM can be modified to accommodate neutrino mass, but there are multiple possible schemes. Until more experimental observations have been made that can motivate one formulation, any neutrino description in the SM is subject to change. [5]

quark and lepton. Leptons interact by the electromagnetic and weak force, but not the strong force. Quarks interact by electromagnetic, weak, and strong force. Leptons come in two varieties, neutral and -1 electric charge (with the magnitude of the electron's charge being considered a unit of charge). Quarks come in two varieties, up-type and down-type, which have electrical charge +2/3 and -1/3, respectively. Finally, the set of two quarks and two leptons comes in three generations of increasing mass. The first generation is comprised of the electron (e), the electron neutrino (ν_e), the up quark (u), and the down quark (d). These particles are stable and the ingredients of everyday matter. Table 1.1 lists the particles of matter by class and generation.

	1st generation	2nd generation	3rd generation
Quarks	u	c	t
	d	s	b
Leptons	e	μ	τ
	ν_e	ν_μ	ν_τ

Table 1.1: The matter of the Standard Model. All matter particles are spin-1/2 fermions. The particles of each generation are arranged in increasing mass. Higher mass quarks and charged leptons decay to lower mass states, so the matter of the everyday world is composed of electrons and u and d quarks.

Interactions between fermions are mediated by gauge bosons, of which more will be said in the following section. The gauge bosons come about as a consequence of a local $\mathrm{SU}(3)_C \times \mathrm{SU}(2)_L \times \mathrm{U}(1)_Y$ gauge invariance on the quantum fields, with the subscripts to be described in the following subsections. The gauge bosons' connection to the classical forces of nature are as follows. The electromagnetic force is mediated by the massless photon, γ. The weak force is mediated by the massive $\mathrm{W}^{\pm}$ and Z bosons. The strong force is mediated by the massless gluons, g. The SM does not describe gravity, which is too weak to be measured in interactions between fundamental particles.

Particle masses are a consequence of the mechanism of spontaneous symmetry breaking, which will also be described. In the simplest model, a scalar field called the Higgs field is introduced. This field has a non-zero expectation value in the ground state and interacts with massive particles; in fact, the masses of particles appear as a consequence of their interactions with the field. Such a field implies the existence of a scalar boson as an excitation of the field, and one such particle was recently discovered by ATLAS and CMS. It has properties that are so far consistent with the Higgs of the SM, though more precise measurements may yield deviations from expectation.

1.1.2 Gauge group theory of the Standard Model

The interactions of the SM are defined in the scope of quantum field theory by a Lagrangian density ($\mathscr{L}$) that is locally invariant under $\mathrm{SU}(3)_C \times \mathrm{SU}(2)_L \times \mathrm{U}(1)_Y$ gauge symmetry transformations. The importance of the SM's symmetries is motivated by Noether's theorem.

Noether's theorem gives a basis for connecting symmetries of nature to conservation laws. A familiar example is a free, non-relativistic particle with a Lagrangian $L = T - V = \frac{1}{2}m\dot{x}^2$. The dynamics of the particle do not depend on its position, a symmetry of invariance under spatial translation, and the corresponding conserved quantity is momentum ($m\dot{x}$).

The requirement of local invariance of $\mathscr{L}$ under the gauge symmetry groups uniquely determines the dynamics of the SM. The gauge groups are associated with the three fundamental interactions of the SM. The $\mathrm{SU}(3)_C$ symmetry defines the strong interaction's charge, called *color*, and the strong interactions between particles. The $\mathrm{SU}(2)_L \times \mathrm{U}(1)_Y$ symmetry defines the quantities *weak isospin* and *weak hypercharge* and the electric and weak interactions between particles. The $\mathrm{SU}(2)_L \times \mathrm{U}(1)_Y$ is spontaneously broken to a new $\mathrm{U}(1)_{em}$ symmetry that defines electric charge.

The strong interaction - quantum chromodynamics

The theory of strong interactions is called quantum chromodynamics (QCD). The $\mathrm{SU}(3)_C$ gauge group describes the color symmetry of the theory and is responsible for strong interactions, which are the interactions of color-charged particles [6, 7]. The subscript C emphasizes that this symmetry

relates to color. Quarks and gluons, collectively called *partons*, have color charge and interact by the strong force. The color charge of a quark is represented by a three-component vector of complex values, corresponding to the three conventional color charges blue, green, and red. In the same way that rotations of space will change the components of angular momentum of a particle, a generalized idea of a rotation in color charge can be imagined that changes the components of color of a quark or gluon.

The strength of the strong interaction is defined by the strong coupling constant $g_s = \sqrt{4\pi\alpha_s}$. This parameter is not precisely a constant. The quantity α_s is a so-called "running coupling constant" that varies as a function that depends on the interaction's momentum transfer, Q. The leading term in a perturbative expansion follows the relation $\alpha_s(Q^2) \sim \frac{1}{\ln(Q^2/\Lambda^2_{QCD})}$, where Λ_{QCD} is called the QCD scale and has a value of $\Lambda_{QCD} \approx 215MeV$. A consequence of this relation is that in interactions with comparatively high momentum transfer, $Q^2 \gg \Lambda^2_{QCD}$, the strong interaction is comparatively weak and the partons behave as though unbound in the nucleus. This feature of QCD, where forces between colored particles become weak for stronger interactions, is called *asymptotic freedom*.

The potential energy of a color singlet quark-antiquark pair is given by the relation $V_{q\bar{q}} \propto \frac{\alpha_s(r)}{r} + ... + \sigma r$. At short distances the Coulomb-like term $\frac{\alpha_s(r)}{r}$ dominates, and at large distance the linear term σr dominates and the attractive force approaches a constant. Because the potential between quarks increases linearly with separation distance, quarks carrying color charge can never exist in unbound states. Isolated color-charged particles are never observed. The property that quarks and gluons only exist within hadrons in a color singlet state is called *confinement*. Confinement is a consequence of the color connections between partons being fragile and prone to breaking. As quarks separate to lengths larger than the size of a ground-state hadron radius, $\sim 10^{-15}$ m, the potential energy stored in the color field grows and it is energetically favorable to produce quark-antiquark pairs. This results in the original two quarks becoming unbound to one another but forming their own hadronic states, neutral in color charge, with quarks pulled from the vacuum. This process is called *hadronization*. The hadronization process results in a narrow cone of hadrons and other particles that are called a *jet*.

Electroweak interactions - the weak and electric forces

The $SU(2)_L \times U(1)_Y$ gauge groups describe the weak force and electromagnetic force, called the *electroweak* force when unified.

The weak force is mediated by the electrically charged $W^{\pm}$ and the electrically neutral Z^0 gauge bosons, which are massive. The $W^{\pm}$ couples to all other particles except for gluons, since the $W^{\pm}$ carries no color charge and the gluon carries no electroweak charge. Similarly, the Z couples to all other particles except for gluons and photons. The $W^{\pm}$ forms vertices with a lepton and its neutrino pair or a up- and down-type quarks. The Z forms vertices with quark-antiquark or lepton-antilepton pairs. The SU(2) symmetry group is the group associated with spin, and it is valid to think of transformations by the weak force as "rotating" a up-type quarks into down-type quarks or leptons into neutrinos. In this sense, the SU(2) symmetry is called *weak isospin*. The SU(2) symmetry group is responsible for a convservation of a component of weak isospin, denoted T_3, which is analogous to angular momentum conservation.

The weak interaction, unlike the strong and electromagnetic, has interactions that depend on the chirality of the fermions. The state, ψ, of a particle has a chirality operator γ^5 with eigenvalues of +1/-1 for right-/left-handed fermions. Consequently, the field can be projected into its left- and right-handed components with the operators $\frac{(1-\gamma^5)}{2}$ and $\frac{(1+\gamma^5)}{2}$, respectively. The chirality of a particle is relevant because left-handed particles participate in weak interactions while right-handed particles do not. Within the mathematical framework of the SM, left-handed fermions transform as a fundamental representation of the $SU(2)$ group, whereas right-handed fermions do not transform. The $SU(2)$ group is therefore sometimes written as $SU(2)_L$, as above, to emphasize that only left-handed fermions interact with the weak interaction's gauge bosons.

As previously mentioned, the weak and electromagnetic force have been unified into an *electroweak* force. In doing so, a $U(1)$ group is added, giving the $SU(2) \times U(1)$ symmetry. The $U(1)$ symmetry is related to a conserved quantity called *weak hypercharge* and denoted Y_W. Since it is a symmetry of weak hypercharge, the $U(1)$ symmetry is sometimes written as $U(1)_Y$. The more familiar electric charge of a particle is calculated from T_3 and Y_W by the relation $Q = T_3 + \frac{Y_W}{2}$. The

charges of quarks and leptons are listed in Table 1.2.

	T	T_3	Y_W	Q
ν_L	1/2	+1/2	-1	0
l_L	1/2	-1/2	-1	-1
u_L	1/2	+1/2	+1/3	+2/3
d_L	1/2	-1/2	+1/3	-1/3
ν_R	0	0	0	0
l_R	0	0	-2	-1
u_R	0	0	+4/3	+2/3
d_R	0	0	-2/3	-1/3

Table 1.2: The charges of quarks and leptons. The symbols l and ν refer to all generations of leptons and neutrinos. Similarly, the symbols u and d refer to up-type and down-type quarks. The subscripts L and R refer to left- and right-handed particles.

The SM still has a lingering problem with particle mass. Adding a term to the SM Lagrangian to account for mass would be problematic for the gauge bosons. A Lagrangian mass term for the gauge bosons would be written as $\frac{1}{2}m^2A^\mu A_\mu$, where A_μ is the gauge field. Such a term must be invariant invariant under the U(1) transformation $A_\mu \rightarrow A'_\mu = A_\mu + \frac{1}{e}\partial_\mu\alpha$, but it would not be. Since the $W^\pm$ and Z bosons are known to have mass, the symmetry must be broken.

Fermion fields are also not gauge invariant if a mass term is present due to the chiral nature of the theory. A Lagrangian mass term for any fermion Ψ is written as the following:

$-m\bar{\Psi}\Psi = -m(\bar{\Psi}_L + \bar{\Psi}_R)(\Psi_L + \Psi_R) = -m(\bar{\Psi}_L\Psi_R + \bar{\Psi}_R\Psi_L)$, since $\bar{\Psi}_R\Psi_R = \bar{\Psi}_L\Psi_L = 0$

This quantity is not invariant under $SU(2)_L \times U(1)_Y$ gauge transformations because the fermions of different chirality transform differently under such rotations. Namely,

$\Psi_L \rightarrow \Psi'_L = e^{iY_L\theta(x)}U_L\Psi_L$

$\Psi_R \rightarrow \Psi'_R = e^{iY_R\theta(x)}\Psi_R$

Because the term is not invariant under gauge transformations, explicit Lagrangian mass terms for the fermions are forbidden. Since fundamental fermions are known to have mass, the point is still clear that the symmetry must be broken.

The Higgs mechanism

The Higgs mechanism spontaneously breaks the $\mathrm{SU}(2)_L \times \mathrm{U}(1)_Y$ electroweak symmetry. Before considering the Higgs mechanism in its full glory, we consider a simplified, example Lagrangian that illustrates spontaneous symmetry breaking.

$$\mathscr{L}_{ex} = \frac{1}{2}(\partial_\mu \phi)^2 - \frac{1}{2}\mu^2\phi^2 - \frac{1}{4}\lambda\phi^4 \tag{1.1}$$

The first two terms of $\mathscr{L}_{ex}$ describe a scalar field with mass μ and the third term gives a four-point self interaction. The parameter λ is positive to ensure that there's an absolute minimum in the potential (since as $\phi \rightarrow \pm\infty$, the potential $V = \frac{1}{2}\mu^2\phi^2 + \frac{1}{4}\lambda\phi^4 \rightarrow +\infty$). Note also that the Lagrangian has a reflection symmetry with respect to the operation $\phi \rightarrow -\phi$.

In this scenario, μ^2 can take a positive or negative value. The simplest view is that μ^2 is positive quantity and represents the squared mass of a scalar particle excitation of the field. In this scenario, the $\lambda\phi^4$ term represents the particle self-interaction. Suppose, however, that μ^2 has a negative value. This results in a modified shape to the potential with two minima at $\phi_{min} \equiv v = (\pm)\sqrt{-\frac{\mu^2}{\lambda}}$. The new minimum, v, is called the *vacuum expectation value* and has a value that is non-zero.

A new field $\eta = \phi - v$ is introduced that simply shifts the field ϕ to be centered on one of the minima. Substituting η in for ϕ to the original Lagrangian gives the following

$$\mathscr{L}_{ex} = \frac{1}{2}(\partial_\mu(\eta + v))^2) - \frac{1}{2}\mu^2(\eta + v)^2 - \frac{1}{4}\lambda(\eta + v)^4 \tag{1.2}$$

$$= \frac{1}{2}(\partial_\mu \eta)^2 - \lambda v^2\eta^2 - \lambda v\eta^3 - \frac{1}{4}\lambda\eta^4 + \frac{1}{4}\lambda v^4 \tag{1.3}$$

by noting $\partial_\mu v = 0$ and $\mu^2 = -\lambda v^2$. This Lagrangian represents a scalar field with mass $\sqrt{-2\mu^2}$. The scalar has self-interaction terms η^3 and η^4. This Lagrangian has lost its reflection symmetry with respect to the operation ($\eta \to -\eta$). Although the underlying theory (Equation 1.1) contains a reflection symmetry, the symmetry has been spontaneously broken by taking a non-zero vacuum expectation value ($v \neq 0$).

Understanding the example Lagrangian helps to understand the Lagrangian of the Higgs sector. A *Higgs field*, ϕ, is introduced that is a complex scalar field in the fundamental doublet representation of $\mathrm{SU}(2)_L$. The Higgs field is charged $Y_W = \frac{1}{2}$, which results in the first component having a positive electric charge while the second is electrically neutral.

$$\phi = \frac{1}{\sqrt{2}} \begin{pmatrix} \phi^+ \\ \phi^0 \end{pmatrix}$$

The Lagrangian for the Higgs sector is written

$$\mathscr{L}_{Higgs} = (D_\mu \phi)^\dagger (D_\mu \phi) + \mu^2 \phi^\dagger \phi - \lambda (\phi^\dagger \phi)^2 \tag{1.4}$$

$$D_\mu = \partial_\mu - igA^a_\mu \tau^a - ig' y_\phi B_\mu \tag{1.5}$$

where A^a_μ and B_μ are the $\mathrm{SU}(2)$ and $\mathrm{U}(1)$ gauge bosons and $y_\phi = \frac{1}{2}$.

As was the case in the example, the "mass" term, μ, is imaginary. Spontaneous symmetry breaking takes effect, resulting in a vacuum expectation value of

$$\phi = \frac{1}{\sqrt{2}} \begin{pmatrix} 0 \\ \sqrt{\frac{-\mu^2}{\lambda}} \end{pmatrix} \equiv \frac{1}{\sqrt{2}} \begin{pmatrix} 0 \\ v \end{pmatrix}$$

As before, the Lagrangian (Equation 1.4) is shifted to the minimum found at the vacuum expectation value. After doing this, the Lagrangian contains mass terms for the Higgs scalar boson as well as three of the four gauge bosons. The A^a_μ and B_μ gauge bosons are gone, mixed into the vector bosons we commonly identify as $W^\pm$, Z, and γ. The masses in these terms are as follows:

$$m_h = v\sqrt{2\lambda} \tag{1.6}$$

$$m_{W^\pm} = \frac{1}{2}vg \tag{1.7}$$

$$m_Z = \frac{v}{2}\sqrt{g^2+g'^2} \tag{1.8}$$

$$m_\gamma = 0 \tag{1.9}$$

Since the particles' masses contain free parameters, the symmetries of the SM make no prediction of these masses. There is, however, a relationship between g and g' that relates the mass of the $W^\pm$ to the Z:

$$\cos\theta_W \equiv \frac{m_W}{m_Z} = \frac{\frac{1}{2}vg}{\frac{v}{2}\sqrt{g^2+g'^2}} = \frac{g}{\sqrt{g^2+g'^2}} \tag{1.10}$$

The Higgs field also gives a mass to the fundamental fermions. As was previously discussed, a Lagrangian term $-m\bar{\Psi}\Psi$ contains terms like $\bar{\Psi}_L\Psi_R$, which are not invariant under $\mathrm{SU}(2)_L \times \mathrm{U}(1)_Y$ symmetry. However, with the scalar field included, it turns out that terms like $\bar{\Psi}_L\phi\Psi_R$ are invariant under the symmetry. Consequently, a Lagrangian term is added that couples the Higgs doublet to fermion fields:

$$\mathscr{L}_{fermion-mass} = -\lambda_f(\bar{\Psi}_L\phi\Psi_R + \bar{\Psi}_R\phi\Psi_L) \tag{1.11}$$

We will consider the effect of this coupling on the electron. For an electron,

$$\mathscr{L}_{electron-mass} = -\lambda_e[(\bar{\nu},\bar{e})_L \begin{pmatrix} 0 \\ v+h \end{pmatrix} e_R + \bar{e_R}(0, v+h) \begin{pmatrix} \nu \\ e \end{pmatrix}_L] \tag{1.12}$$

$$= -\frac{\lambda_e(v+h)}{\sqrt{2}}[\bar{e}_L e_R + \bar{e}_R e_L] \tag{1.13}$$

$$= -\frac{\lambda_e(v+h)}{\sqrt{2}}\bar{e}e \tag{1.14}$$

$$= -\frac{\lambda_e v}{\sqrt{2}}\bar{e}e + \frac{\lambda_e h}{\sqrt{2}}\bar{e}e \tag{1.15}$$

The first term gives the electron its mass, $m_e = \frac{\lambda_e v}{\sqrt{2}}$. The second term gives a coupling of left- and right-handed electrons to the Higgs field, a coupling which is a Yukawa coupling, one proportional to the electron's mass. The quarks can be given mass and a Yukawa coupling to the Higgs field in a similar fashion.

1.1.3 Higgs production

In hadron colliders, the Higgs can be produced in various ways [8, 9]. The production rate is inherently linked to the Higgs' coupling strength, which is proportional to the mass of particles coupling to it. Figure 1.1 shows a few such production mechanisms. The Higgs boson is most frequently produced by gluon fusion, where two gluons form a top loop that annihilates to produce the Higgs boson[2].

The relative probability of a process occurring is characterized in terms of a quantity called a cross section and measured in units of barns (b), where 1 b = 10^{-28} m^2. The total cross section of p-p collisions at $\sqrt{s} = 8$ TeV is about 102 mb [11]. A quarter of the total cross section, 27 mb, is due to elastic $pp \to pp$ scattering events. The remaining inelastic collisions produce new particles from the dissociation of one or both protons. In contrast, interesting physics processes with high mass, high energy particles being created have a much smaller cross section, beginning on the order of 10^{-12} b.

With this in mind, the primary modes of Higgs production can be quantified [12]. For a SM Higgs with $m_H = 125.0$ GeV at center-of-mass collision energy $\sqrt{s} = 8$ TeV, the production cross section of gluon fusion is $\sigma_{ggH} = 19.27 \pm 10\%$ pb. The other forms of production are vector-boson (WW, ZZ) fusion with a cross section of $\sigma_{VBF} = 1.58 \pm 3\%$ pb, vector-boson (W, Z) bremsstrahlung with $\sigma_{W/ZH} = 1.12 \pm 3\%$ pb, and top fusion with $\sigma_{ttH} = 0.13 \pm 12\%$ pb. The large cross section of gluon fusion production makes a search for Higgs production through this mechanism useful.

---

[2]Gluon fusion includes loops of all fermions, but the top quark is the most massive, with the largest coupling to the Higgs boson, and consequently has the dominant contribution. The next strongest production cross section, due to the bottom quark, is smaller by a factor of $\sim 1/35^2$[10].

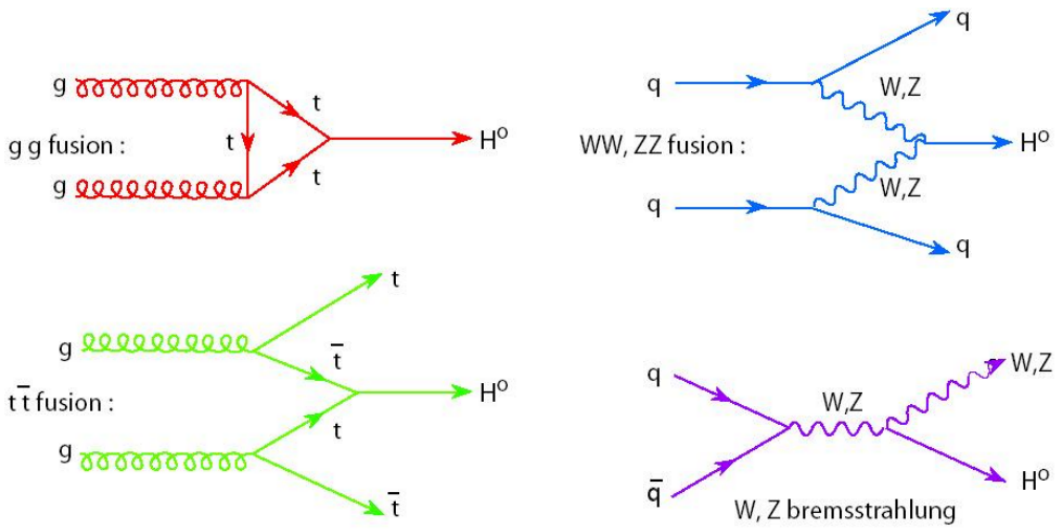

Figure 1.1: The four leading mechanisms of Higgs boson production at the LHC.

1.2 Proton Collisions

1.2.1 The hard scatter

Hard interactions in proton-proton collisions take place between the proton's parton constituents. The momentum of the parton constituents have a probabilistic fraction of the hadron's total energy, with its fraction defined by a parton (probability) distribution function (PDF). The value $f_a(x)$ is the probability for a parton, a, to have a fraction of the proton's total momentum, x. The PDF varies with the squared energy scale (Q^2) of the interaction. The x-dependence of PDFs are determined by experimental data. The CTEQ6M PDF incorporates measurements from various past experiments including H1, ZEUS, D0, and CDF [1].

The parton distributions of CTEQ6M are shown is Figure 1.2. As the PDF shows, u and d quarks dominate interactions at high x. Gluons and virtual quarks, called "sea quarks", exist in the partons' color field. Interactions with the gluons are most dominant at low x. The sea quarks,

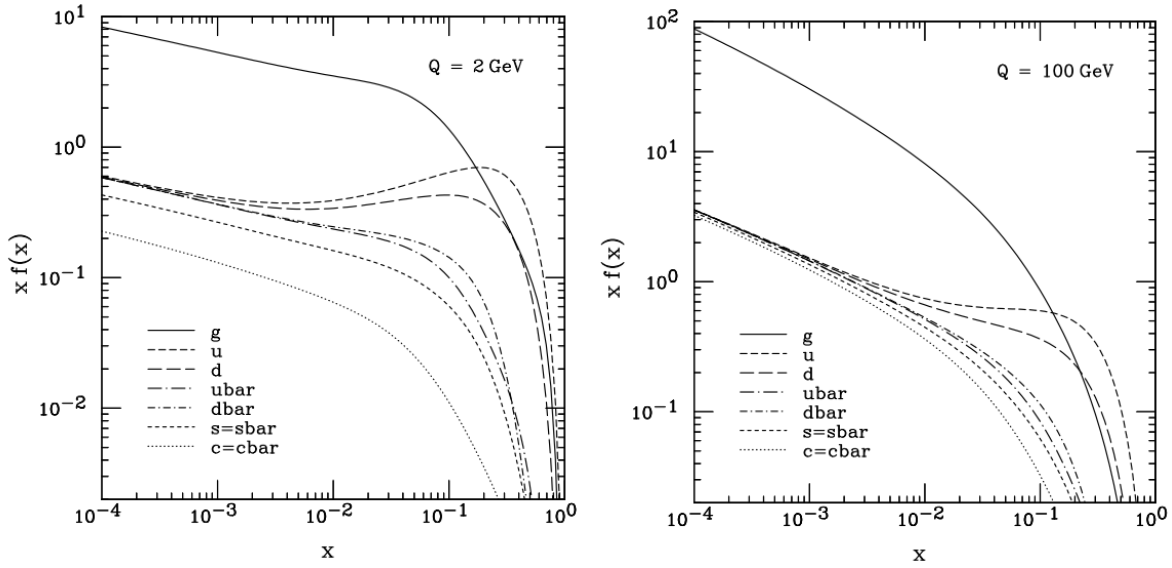

Figure 1.2: The parton distribution functions for CTEQ6M momentum transfers of $Q^2 = 2$ GeV (left) and $Q^2 = 200$ GeV (right). [1]

such as $\bar{u}, \bar{d}, s, \bar{s}, c, \bar{c}$, are pair-produced out of gluons in the color field. A consequence of the PDF is that hard scatters, which require a large x, are more common for quark-quark interactions and soft scatters are more typically gluon-gluon interactions. A quark-gluon interaction falls somewhere between. In calculating a process' cross section, the PDF must be convoluted with the hard scattering cross section of the constituents.

1.2.2 Beam remnant

The most typical sort of collisions between hadrons consist of multiparton interactions leading to multi-particle production at small p_{T}, approximately uniformly distributed in rapidity. When a hard interaction occurs, partons have scattered out from each proton and the remaining partons, collectively called *the beam remnant* no longer form a color singlet - they must interact. Consequently, a hard collision contains a multi-particle production that is essentially overlaid on the hard

parton scatter.

1.2.3 Initial and final state radiation

The highly accelerated, color and electrically charged particles in a hadronic collision can emit radiation in the form of gluons and photons. If the incoming partons radiate before interacting, the radiation is termed initial state radiation (ISR). Similarly, if the collision's outgoing particles radiate, the radiation is termed final state radiation (FSR). Radiation, both ISR and FSR, is most probable to exist as low energy gluons that are collinear with the parton that emitted it. When the radiation is low energy and collinear with outgoing particles, it may appear to be part of the outgoing partons' hadronic jet. If the radiation is more energetic and not collinear, it may be separated enough that the detector sees separated regions of energy in the calorimeter, potentially resulting in additional jets being reconstructed in the event.

1.3 Beyond the Standard Model

The Standard Model as presented accounts for essentially all observed particle interactions to date[3]. However, there are central questions that the SM doesn't and cannot address. The following briefly describes them.

The hierarchy problem

The observation of a Higgs boson mass of 125 GeV indicates an issue in the formulation of the SM. The mass of the Higgs boson is calculated as a sum of loop corrections, terms of which are much, much larger than 125 GeV. Either the terms must cancel to arrive at 125 GeV, an unlikely "just so" scenario that is called *fine tuning*, or there is another natural principle responsible for the precise cancellation of large terms. Extensions to the SM have been proposed that could explain

[3]The observation of neutrinos being massive and oscillating is not a part of the SM, but such a modification is possible in a way that doesn't resolve the other issues described in this section.

this cancellation. The most famous extension is supersymmetry (SUSY), which proposes for every particle in the SM there exists a new "superpartner" particle, called a *sparticle*.

In the SUSY scheme, each fermion particle's sparticle would be a boson and each boson particle's sparticle would be a fermion. A consequence of SUSY theory is that each large term in the calculation of the Higgs boson's mass has an accompanying large term due to the superpartner, except that the term has opposite sign resulting in an automatic cancellation of terms that avoids the need for fine tuning. Figure 1.3 shows an example of cancelling Feynman diagrams. Unfortunately, no sparticles have yet been experimentally observed.

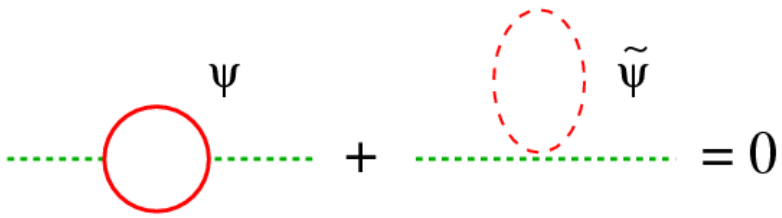

Figure 1.3: Feynman diagrams representing the cancellation of quadratic terms of Higgs' mass due to SUSY superpartners. [2]

Dark matter

Dark matters' existence is inferred from cosmological observation. Galaxies are observed to rotate more quickly than is predicted based on the amount of mass observed within them. Said another way, there is not enough observed mass to gravitationally bind the galaxy with the observed rotation. The faster rotation is consistent with a galaxy that contains more matter than what is observed, and such non-observed matter is referred to as *dark matter*. The existence of dark matter is corroborated by observations of clusters of galaxies, where gravitational lensing, galactic radial velocities, and x-ray emission measurements provide three independent measurements of mass that exceeds that of visible matter. Dark matter is assumed to be one or more particles that have not yet been

detected. The particles interact with normal matter gravitationally and could also interact at the weak scale by other forces. Figure 1.4 shows the measured velocity of visible matter and shows a discrepancy from the expected distribution in the hypothesis of no dark matter existing.

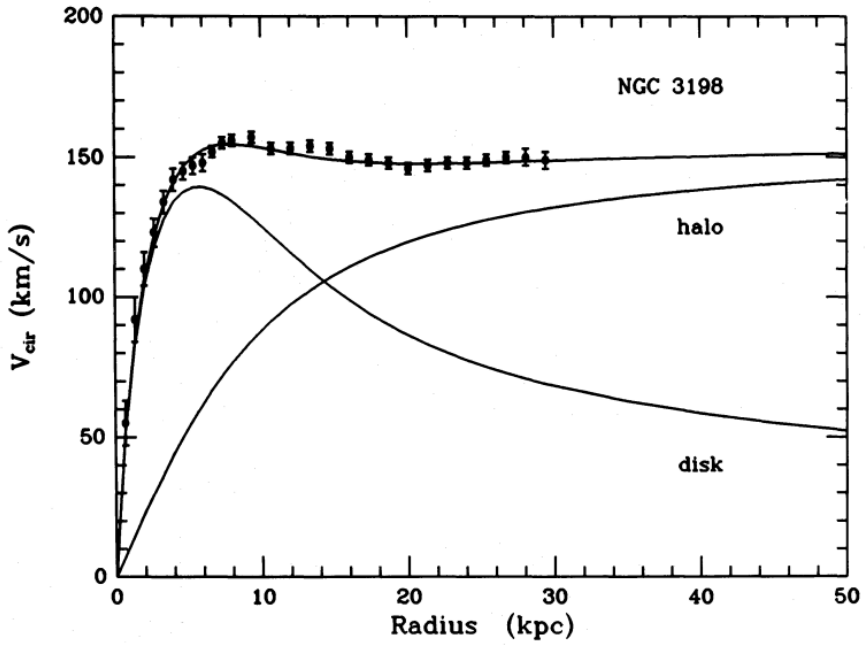

Figure 1.4: Relationship between radial distance and velocity of visible matter in the galaxy NGC 3198. The data points with error bars and best-fit line show the measured data, which is consistent with a flat distribution from $\sim 8-30$ kpc. The curve labeled "disk" shows the expected relationship when the galaxy's visible matter is approximated as a continuous, exponentially falling disk-shaped distribution of mass. The discrepancy between the measured distribution and disk prediction can be corrected by adding a spherical dark matter halo to the galaxy, which is the distribution labeled "halo". [3]

1.3.1 The Hidden Valley Model

Beyond the particles contained in the SM, there could exist additional particles and interactions that have not yet been observed. An extant particle that has low mass ($<\sim$ 100 GeV) that was energetically accessible in a previous experiment would need to be produced in low abundance to have escaped observation. The low abundance implies that such a low mass particle must couple very weakly to the known particles of the SM. If new particles that are more massive exist, they could couple more strongly to SM particles. These more massive particles' non-observation could be a consequence of accelerator (production) energies that had not yet been reached. Whether a new particle's mass is low or high, such particles as described above are referred to as *hidden* or *dark* due to their status of having gone unobserved thus far. Models that incorporate these particles and interactions are referred to as Hidden Valley (HV) models, in analogy to a person looking out over a landscape that looks complete but could contain a valley that is out of sight over a hillcrest. Objects in this new sector are denoted with a v- prefix or v subscript, as in v-quark or q_v.

Two HV models are considered here that extend the SM by introducing a hidden sector with a non-abelian group G_v. The SM particles are neutral to G_v and hidden sector particles are neutral to G_{SM}. Interactions between the SM and hidden sector are possible through a massive, neutral mediator such as a new Z' gauge boson or Higgs bosons. Two specific HV benchmark models are considered for this analysis. Both models assume a QCD-like hidden sector.

The first HV benchmark model involves the production of a SM Higgs boson or another more massive scalar[4] that can mix into a hidden sector scalar via a $|\Phi|^2|\Phi_{hs}|^2$ coupling[5]. The v-sector scalar, Φ_{hs}, decays to v-quarks. The v-quarks are assumed to hadronize into a pair of pseudo-scalar v-mesons called π_v^0. The two π_v^0, of course, have opposite momenta and travel out back-to-back in the scalar Φ_{hs} boson center of mass frame. The π_v^0 have an unknown lifetime and, if they live long enough, can lead to displaced decays in a detector. The π_v^0 decays via a hidden sector heavy Z':

[4]Additional scalars are possible in BSM physics scenarios, such as the Two-Higgs-doublet model [13]. In this scenario, the scalar boson discovered in 2012 is one of five Higgs particles, with four remaining at large.

[5]The Φ generically refers to the SM Higgs boson or another scalar boson. When the discovered 125 GeV scalar is specifically referred to, h will instead be used.

$\pi_v^0 \to Z' \to f\bar{f}$. The π_v^0 decay preferentially to the heaviest kinematically allowed fermion pair.[6] For $2m_b < m_{\pi_v} < 2m_t$, the dominant decay product is $b\bar{b}$ pairs. This process is shown in Figure 1.5.

The second model has a heavy Z' boson produced by quark-antiquark annihilation. The Z' decays to the hidden sector by $Z' \to q_v\bar{q}_v$. The v-quarks hadronize, and the v-hadrons decay immediately into showers of v-pions, π_v^0 and $\pi_v^\pm$. The relatively high mass of the Z' results in a high multiplicity of π_v^0 and $\pi_v^\pm$ produced. Here, the $\pm$ and 0 superscripts indicate a charge under the v-sector $\mathrm{U}(1)'$ gauge group, and not SM electric charge. The $\pi_v^\pm$ could be permanently stable or decay, depending on the physics of the HV. Here, the $\pi_v^\pm$ are allowed to decay, though the process allowing the decay is not specified in detail. For the $\pi_v^\pm$ to decay, they are are constrained to having the following properties. First, it should be weakly coupled to the Standard Model particles to insure that $\pi_v^\pm$ are long-lived. Second, the $\mathrm{U}(1)$ symmetry must be spontaneously broken to allow the non-conservation of v-electric charge, perhaps through a v-Higgs mechanism. Third, the final couplings to the SM quarks should be approximately diagonal in flavor so as to avoid the rather stringent Flavor Changing Neutral Current limits. A simple mechanism to satisfy these constraints is to include a v-Higgs field with an appropriate vacuum expectation value, which mixes with the Standard Model Higgs (as discussed in the scalar scenario section). In any case, it is expected that, to a good approximation, the coupling of the charged $\pi_v^\pm$ to Standard Model quarks will scale like the Yukawa couplings of the Standard Model Higgs, resulting in decays predominantly to b-quarks for $2m_b < m_{\pi_v} < 2m_t$. For simplicity, this model assumes π_v^0 decay promptly, and the lifetime of the $\pi_v^\pm$ is treated as a free parameter. This process is shown in Figure 1.6.

The analysis presented in this thesis focuses on the search for a SM Higgs or other scalar boson produced by gluon fusion that decays into two π_v^0 which each decay to fermion pairs. The efficacy

---

[6] The π_v^0 decays preferentially to heavy fermions due to the same helicity suppression that causes SM π^+ to preferentially decay to $\mu^+\nu_\mu$ versus $e^+\nu_e$. The SM π^+ (spin-0) decays into fermions (spin-1/2) with opposite spins. In the frame of the SM π^+, both decay products must have either right-handed or left-handed helicity. However, the weak force couples to left-handed chiral fermions and right-handed chiral anti-fermions. The relation between helicity handedness and chirality handedness is given by $u_\uparrow = \frac{1}{2}(1+\frac{p}{E+m})u_R + \frac{1}{2}(1-\frac{p}{E+m})u_L$, where $u_\uparrow$ is the right-handed helicity state, and u_R and u_L are the right- and left-handed chirality states. Consequently, massive fermions in the right-handed helicity state have a nonzero left-handed chiral component. Due to the above relation, decay fermions that are less massive have a smaller "opposite" chiral component and are unfavored to be produced by the decay of a scalar particle a process called *helicity suppression*.

of reconstructing long-lived particle decays in the Z' model is shown to demonstrate the ability of long-lived particles being identified in a busier detector environment. The general label π_v will be used to represent the long-lived particle, which refers to π_v^0 when referring to the π_v^0 of the HV scalar boson model and $\pi_v^\pm$ when referring to the $\pi_v^\pm$ of the HV Z' model. The search presented is not highly specific to the precise nature of physics in the hidden sector. Consequently, results will be presented in terms of the physical parameters m_{π_v}, τ_{π_v}, m_h or m_Φ, and the production cross section times branching ratio, $\sigma_{gg\to h_{SM}} \times BR(h_{SM} \to \pi_v\pi_v)$ or $\sigma_{gg\to\Phi} \times BR(\Phi \to \pi_v\pi_v)$.

Although the search presented in this thesis gives results in terms of the HV benchmark models, the results may be interpreted in the context of any model with long-lived neutral particles that have a displaced decay. Many models that extend the SM could have long-lived neutral particle decays, including gauge-mediated supersymmetry breaking (GMSB) models [14], the minimal supersymmetric standard model (MSSM) with R-parity violation [15], inelastic dark matter models [16], stealth supersymmetry (Stealth SUSY) models [17, 18], two Higgs doublet models (2HDM) [13], and a baryogenesis model [19].

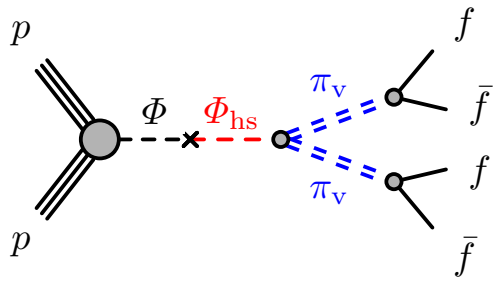

Figure 1.5: Diagram of the Higgs boson or scalar boson benchmark model. The long-lived particles in these processes are represented by double lines and labeled π_v.

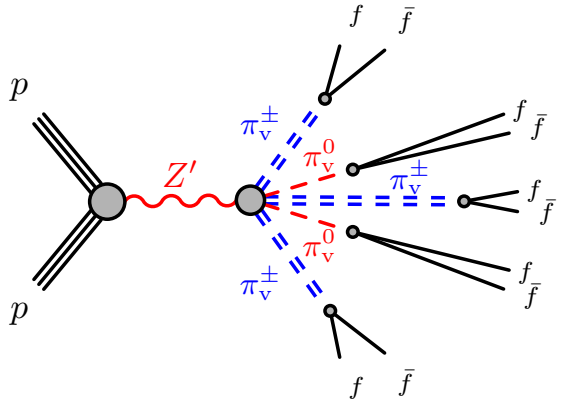

Figure 1.6: Diagram of the Hidden Valley Z' benchmark model. The long-lived particles in this process are represented by doubled lines and labeled $\pi_{\mathrm{v}}^{\pm}$. The π_{v}^{0} particles have short lifetime and decay promptly. The $\pm$ and 0 superscripts for the π_{v} indicate a charge under the v-sector gauge group, not electric charge.

Chapter 2

EXPERIMENTAL APPARATUS

2.1 The Large Hadron Collider

The Large Hadron Collider (LHC) is an underground hadron collider at CERN, the European Organization for Nuclear Research. It accelerates and collides two beams of protons (or sometimes lead ions) at the highest energies yet achieved. It is the world's largest collider, 27 km circumference, located about 100 m underground in France and Switzerland, crossing the Swiss-French border at four points. The LHC was designed to collide protons at a center of mass energy of 14 TeV at an instantaneous luminosity of $10^{34}\text{cm}^{-2}\text{s}^{-2}$, although proton collisions in 2011 and 2012 had a center of mass energy of 7 and 8 TeV, respectively.

Bringing the proton beam up to the collision energy requires a series of accelerators that sequentially accelerate the protons. The protons originate from a duoplasmatron source, which ionizes hydrogen. The protons are separated from electrons by an electric field, which produces an initial 92 keV proton beam. Protons from this beam are bunched together and injected into LINAC (linear particle accelerator) and accelerated to an energy of 50 MeV. Next, they are passed into the PSB (proton sychrotron booster) that accelerates the beam to 50 MeV. The protons are subsequently passed into the PS (proton sychrotron), accelerating them further to 25 GeV. The protons are then transferred to the SPS (super proton synchrotron), accelerating them to 450 GeV. The protons are finally injected into the LHC, which accelerates them to the final beam energy. The LHC complex is illustrated in Figure 2.1.

The LHC ring layout is shown in Figure 2.2. It is composed of eight straight 528 m sections, identified as Point 1 through Point 8. There are 1232 superconducting dipole magnets that generate a magnetic field of up to 8 T distributed along the ring to bend the beam around its circular path. There are 392 quadrapole magnets along the straight sections that focus the beam. The SPS injects

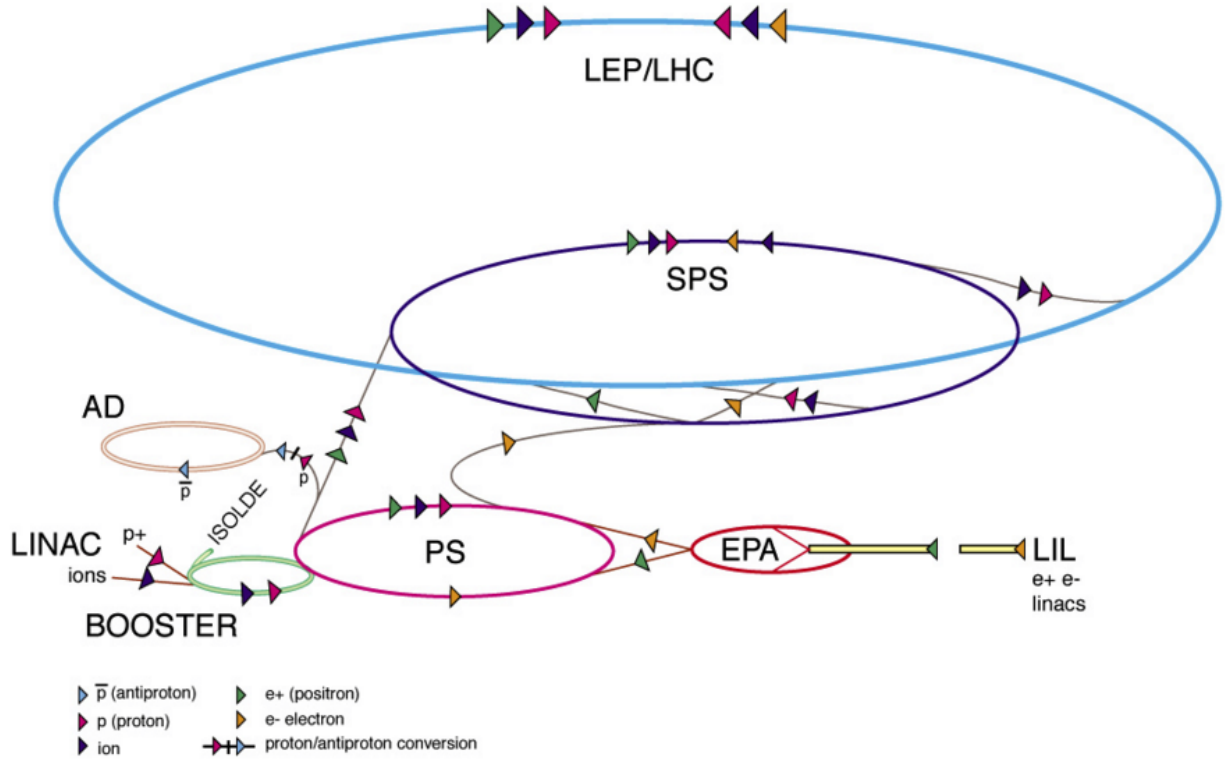

Figure 2.1: Illustration of the LHC accelerator complex. Protons are accelerated in series through the LINAC, SPS (labeled BOOSTER in figure), PS, SPS, and LHC rings. The AD (antiproton decelerator) storage ring can eject antiprotons to one of several connected antimatter experiments. The EPA (electron-positron accumulator) ring stored electrons and positrons produced by the LIL (LINAC injector for LEP) before they were accelerated and injected into LEP. The AD and EPA are not used by the LHC.

protons into the LHC ring near Point 1. Beam acceleration takes place in radio frequency (RF) cavities at Point 4. The beam is collimated at Points 3 and 7. Collisions occur where the beams are made to collide at Points 1, 2, 5, and 8, where the four major LHC experiments are located. The beam is "dumped" at Point 6 by ejecting it into a graphite target capable of absorbing the beam's energy.

In an accelerator, the particles are collected into "bunches" rather than as a continuous stream.

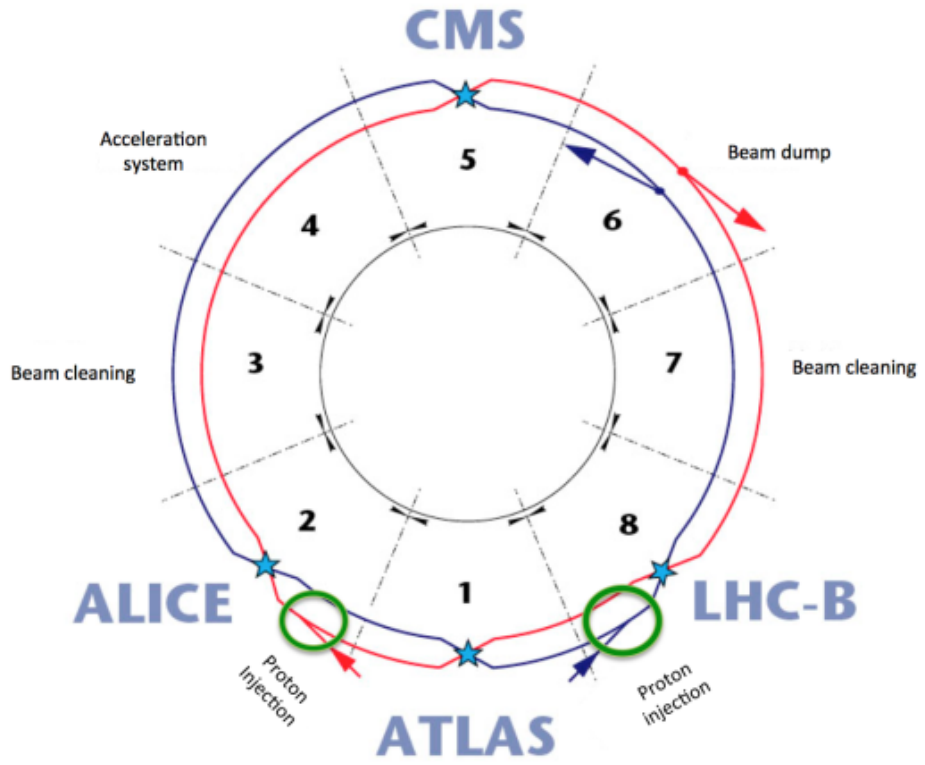

Figure 2.2: Schematic of the LHC showing the locations of the beam injection, four interaction points, beam focus (labeled "Beam cleaning"), and beam dump.

This is done because the beam is accelerated by RF cavities that operate at about 400 MHz, giving rise to 35640 potential wells in the RF field. Propogating at nearly the speed of light, this corresponds to bunches that have 2.5 ns spacing. The LHC design fills about one out of every 10 potential wells, resulting in 3564 bunches within each beam and a spacing of 25 ns.

Since LHC collision events contain bunches of protons, multiple proton-proton interactions are possible in each bunch crossing. The majority of proton-proton interactions result in low-p_{T} scatters that can produce tracks and jets that overlap with the high-p_{T} event of interest. The additional interactions present in an event of interest in known as *pileup*. The mean number of

interactions per bunch crossing typically ranged from about 10 to 35. The full distribution of the mean number of interactions per bunch crossing is shown in Figure 2.3.

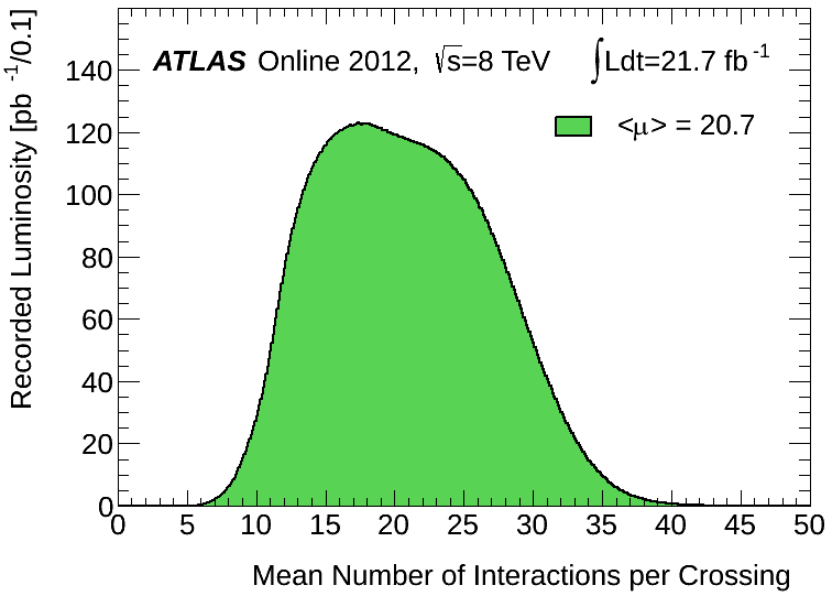

Figure 2.3: Distribution of the mean number of proton-proton interactions per bunch crossing at the LHC in 2012.

The LHC has two large, general-purpose detectors: A Toroidal LHC Apparatus (ATLAS) and the Compact Muon Solenoid (CMS). On July 4, 2012 both experiments announced the observation of a scalar boson with a mass of about 125 GeV [20, 21]. Five more specialized detectors are built along the LHC ring: A Large Ion Collider Experiment (ALICE), the Large Hadron beauty (LHCb) detector, TOTal Elastic and diffractive cross section Measurement (TOTEM), the Large Hadron Collider forward (LHCf), and the Monopole and Exotics Detector at the LHC (MoEDAL).

Experiments such as ATLAS must interface with the LHC to ensure safe operation of their machines. The LHC supplies experiments with information on the beam and bunch intensities, the beam's position, and the 40.08 MHz bunch clock of the accelerator, which is used by experiments for accurate event triggering. In turn, experiments such as ATLAS provide information on lumi-

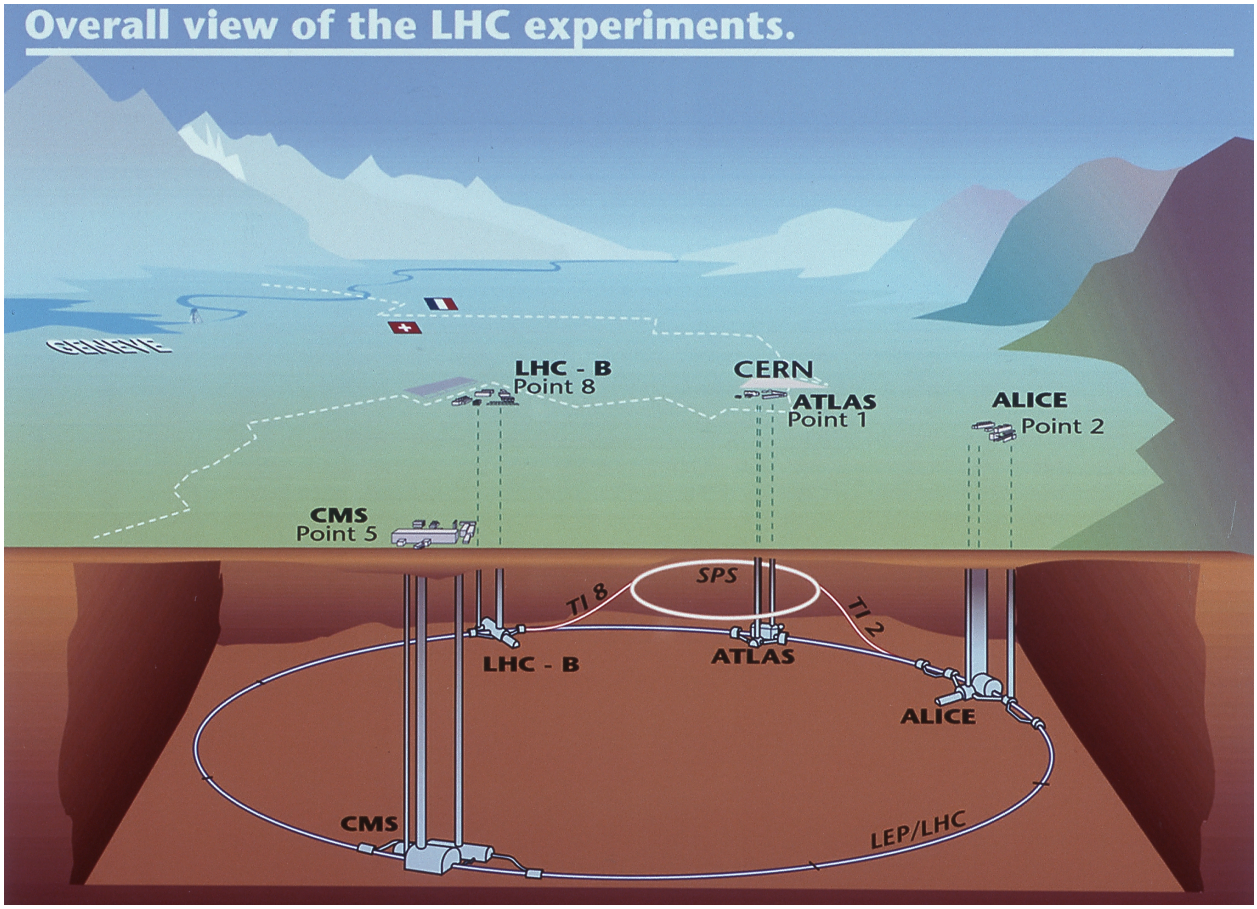

Figure 2.4: Diagram of the Large Hadron Collider. ATLAS is located on the south side of the ring at point 1.

nosity from their luminosity detectors, quality of collisions from beam conditions monitors, and whether or not to safely inject or dump the beams or move between modes of operation, such as filling to ramping.

2.2 The ATLAS Detector

The ATLAS detector is a general-purpose detector on the LHC [22]. It is composed of three major detector systems, from innermost to outermost: the inner detector, calorimeter, and muon spectrometer. Figure 2.5 shows a cut-away view of ATLAS.

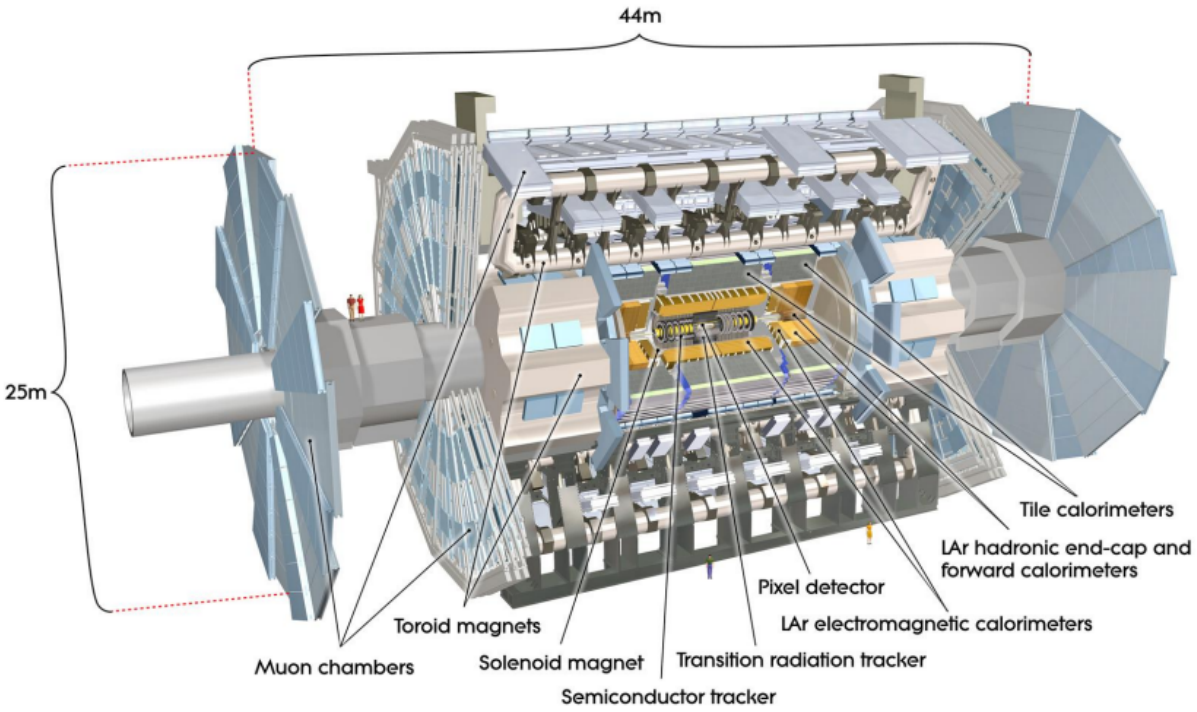

Figure 2.5: Three dimensional overview of the ATLAS detector.

2.2.1 Coordinate System

The ATLAS coordinate system is defined with the origin $(x,y,z) = (0,0,0)$ at the center of the detector, which is the nominal proton-proton interaction point (IP). The direction of $\hat{x}$ is toward the center of the LHC ring, and the direction of $\hat{y}$ is upward. The coordinate system is right-handed, defining the longitudinal or direction $\hat{z}$ to point along the beampipe according to $\hat{z} = \hat{x} \times \hat{y}$. The half of the detector with $|z| > 0$ is referred to as the "A-side"; the other half is the "C-side".

The x-y plane is perpendicular to the beam line and referred to as the transverse plane. The azimuthal angle around the transverse plane, ϕ, is measured from the x-axis. The radial distance, $r = \sqrt{x^2 + y^2}$, is the distance of a point from the beam line. A polar angle θ measures the angle of a point from the z-axis. Instead of the polar angle, the pseudurapidity $\eta = -\ln[\tan(\theta/2)]$ is used. To describe angular separation, $\Delta R = \sqrt{\Delta\eta^2 + \Delta\phi^2}$ is often used.

ATLAS uses *natural units*, where the speed of light, c, is defined as one (unitless). In this system, energy, momentum, and mass are all measured in units of energy. This can be a useful convention for highly relativistic particles, since when $p \gg mc$, $E \approx p$ and the particle's energy or magnitude of momentum are described by the same quantity. In natural units, time (e.g. mean proper lifetime) similarly has units of distance.

2.2.2 Inner Detector

The inner detector (ID) is designed to measure the momentum of charged particles originating at or near the IP. It is immersed in a 2 T solenoid magnetic field and consists of three complementary sub-detectors: the pixel detector, semiconductor tracker (SCT), and transition radiation tracker (TRT). The inner detector efficiently measures charged particles with $p_{\mathrm{T}} > 0.5$ GeV and $|\eta| < 2.5$. It physically extends within the space of a cylinder defined by $|z| < 3512$ mm, $r < 1150$ mm. Figure 2.6 shows how the ID's sub-detectors are arranged.

Pixel Detector

The pixel detector is a detector made up of about 80 million individual pixels, each of size 50 x 400 μm. The detector can be separated into its barrel and endcap sub-detector regions. The barrel has three layers concentric with the beamline covering $|z| < 400.5$ mm, at radii of 50.5, 88.5, and 122.5 mm. Each endcap has three disk layers located at $|z| = 495$, 580, and 650 mm, extending in the radial direction extending through the region 88.8 mm $< R <$ 149.6 mm. The pixels have an intrinsic accuracy of 10 μm in $(R-\phi)$, 115 μm in z in the barrel and 10 μm in $(R-\phi)$, 115 μm in R in the endcaps. The detector layers are arranged to provide good angular coverage so that a charged particle typically leaves hits across three pixel layers. It is the innermost detector system, designed with the greatest granularity of any ATLAS subdetector, and provides high precision measurements for identifying the location of the primary and secondary vertices.

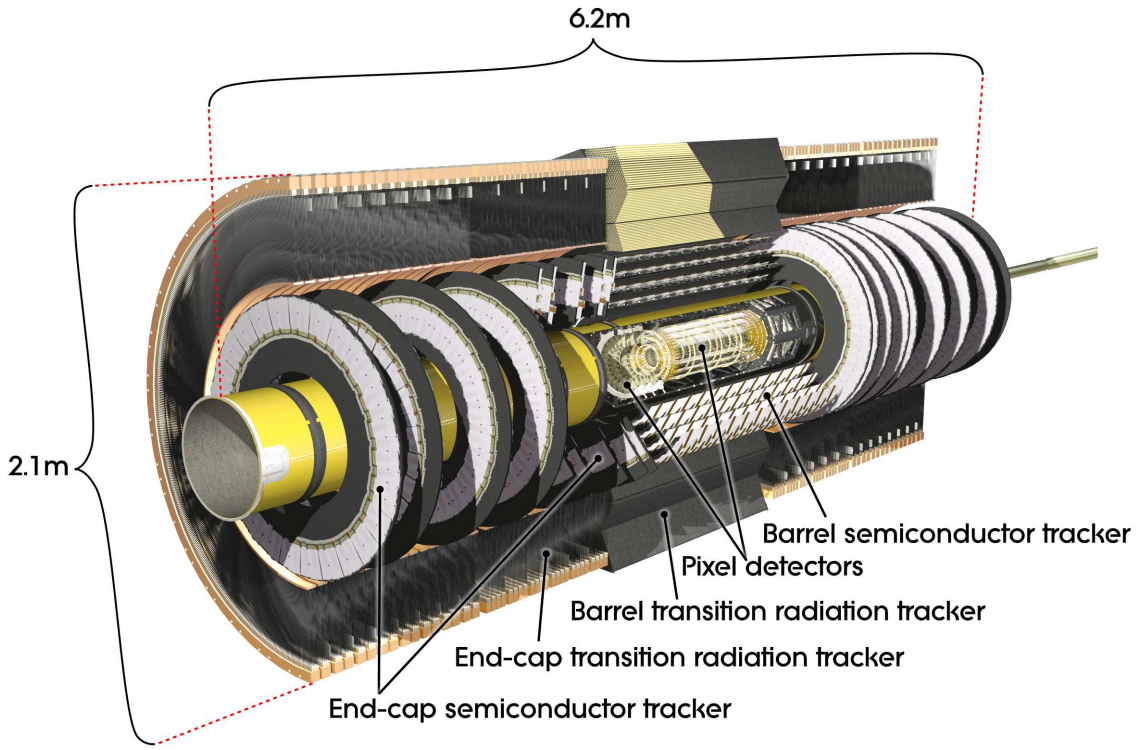

Figure 2.6: Cut-away view of the ATLAS inner detector.

Semiconductor Tracker

The SCT detector is assembled from silicon microstrip sensors. In the barrel, strips are assembled across four layers longitudinally and in the endcap across nine layers radially. Each layer has stereo angle wire pairs that are arranged to overlap with the slight angular offset of 40 mrad, and the coincidence of two hits gives a precise space point measurement in r, ϕ, and z of a charged particle. In the barrel, hits have an intrinsic accuracy of 17 μm in (r-ϕ) and 580 μm in z. In the endcap, hits have an intrinsic accuracy of 17 μm in (z-ϕ) and 580 μm in r.

Transition Radiation Tracker

The TRT detector is built of straw-tubes containing Xe-based gas mixture and a central wire at +1560 V electric potential, that collects electrons from gas ionization. In the barrel, the straw tubes

are 144 cm in length and arranged in 73 concentric layers in the barrel; in each endcap, they are 37 cm in length and arranged in 160 radial wheels. The straw tubes can only measure precisely in the coordinate perpendicular to the tube's orientation - $(r-\phi)$ in the barrel and $(z-\phi)$ in the endcaps. Hits are measured with an intrinsic accuracy of 130 μm. In addition to tracking the path of charged particles, the TRT aids in particle identification. Electrons deposit additional radiation when transitioning between materials compared to other charged particles such as muons or pions. An electron may typically give 7 to 10 hits with significantly increased charge collected, called "high-threshold" hits, allowing the TRT to identify it.

2.2.3 Calorimetry

The calorimeter systems in ATLAS are comprised of sampling detectors that are symmetric in ϕ about the beam axis. The calorimeter is composed of an inner electromagnetic calorimeter and an outer hadronic calorimeter. The ATLAS calorimeter is illustrated in Figure 2.7.

The innermost calorimetry systems use liquid argon as the active detector medium, chosen for intrinsic linear behavior, stability of response over time, and radiation-hardness. In the barrel, this is the electromagnetic barrel calorimeter, which is housed in a barrel cryostat. Each of the endcaps has an cryostat that houses an electromagnetic endcap calorimeter (EMEC), a hadronic endcap calorimeter (HEC) behind the EMEC, and a forward calorimeter (FCal).

The electromagnetic calorimeters, lead-liquid argon detectors, have accordion-shaped absorbers and electrodes. They are arranged in several layers outward from the IP. There are three layers in the electromagnetic calorimeter's precision-measurement region ($|\eta| < 2.5$) and two layers in the forward region ($2.5 < |\eta| < 3.2$) and the overlap region, which bridges the gap between the barrel and EMEC. The FCal provides electromagnetic coverage even farther in the forward region ($3.1 < |\eta| < 4.9$). In the $|\eta| < 1.8$ region, an instrumented argon layer presampler is used to provide a measure of the energy lost to interactions in the inner detector.

The hadronic calorimeter is outward from the liquid argon electromagnetic calorimeters and composed of a sampling medium of scintillator tiles and steel absorber material. Scintilator tiles are used to provide maximum interactions length at the lowest cost of construction. A nuclear

interaction length is the mean material distance required to reduce the amount of particles travelling through the material by a factor of $1/e \approx 0.37$. The tiles are used in the central barrel and two extended barrels and together cover the region $|\eta| < 1.7$.

Calorimeters must stop electromagnetic and hadronic showers from punching through into the muon system in order to fully measure the shower energy and allow good measurements with the MS system. The depth of the EM calorimeter is greater than 22 radiation lengths (X_0) and the hadronic calorimeter has greater than 9 interaction lengths (λ). The total thickness reduces the rate of punch-through to less than that of muons that originate promptly or from jet showers. The quantity $E_{\mathrm{T}}^{\mathrm{miss}}$ is a measure of the imbalance of transverse energy calculated by taking the negative of the vector sum of transverse energies measured in the detector. A good measurement of $E_{\mathrm{T}}^{\mathrm{miss}}$ requires good coverage across η and ϕ and enough depth to contain the energy of showers. The thickness of the calorimeter systems is shown in Figure 2.8 as a function of η.

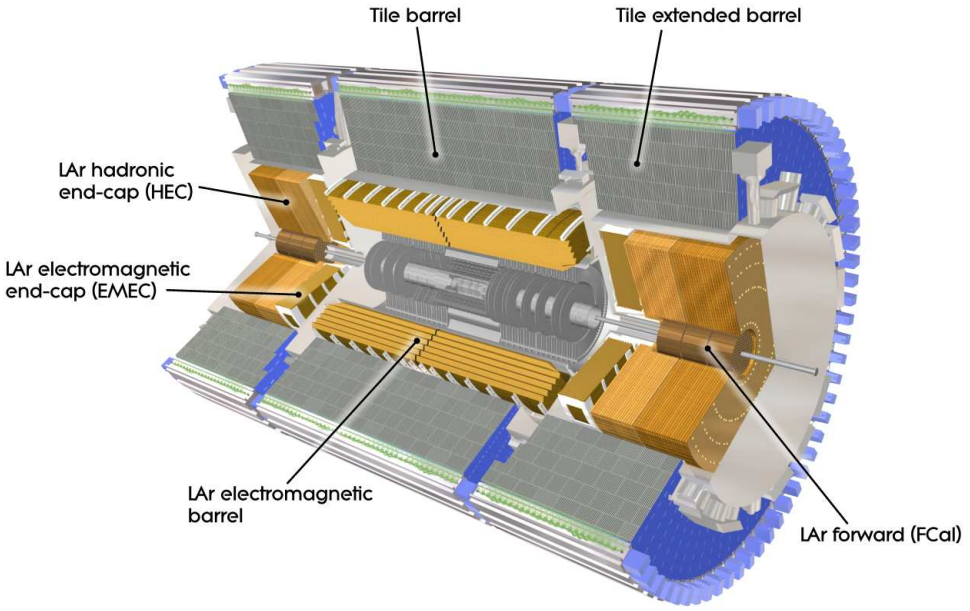

Figure 2.7: Illustration of the ATLAS calorimeter.

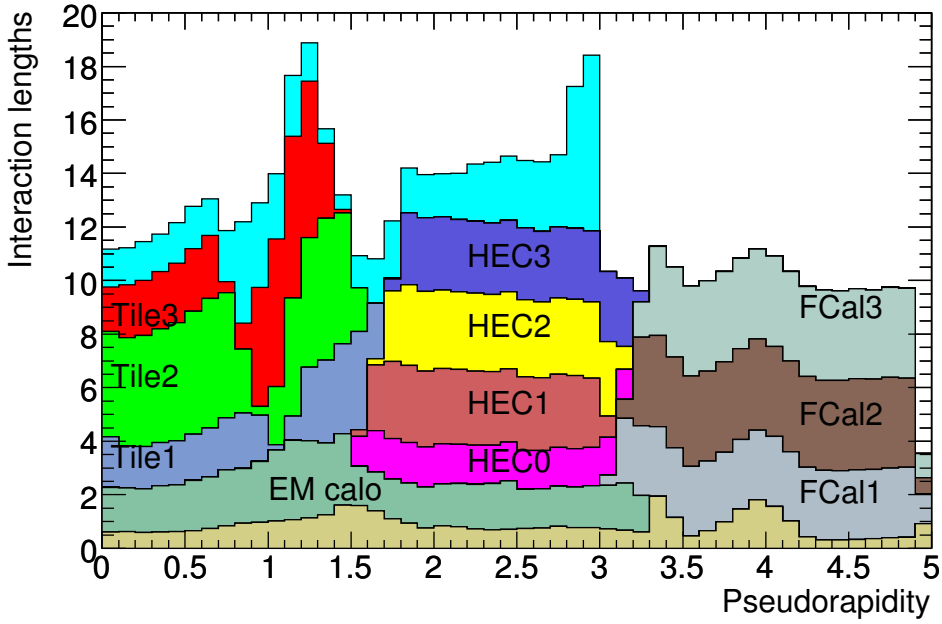

Figure 2.8: Total amount of material in units of interaction length as a function of $|\eta|$. Shown is the material before the calorimetry, the electromagnetic and hadronic calorimeters, and material in front of the first active layer of the muon spectrometer.

2.2.4 Muon Spectrometer

The muon spectrometer (MS) is the largest, outermost major detector system. It is designed to measure charged particles that escape the calorimeter. It measures muon momentum in the region $|\eta| < 2.7$ and provides a trigger in the region $|\eta| < 2.4$. Hits in the muon spectrometer are collected with four principle technologies. Monitored drift tubes (MDTs) and cathode strip chambers (CSCs) provide precision hit measurements. Resistive plate chambers (RPCs) and thin gap chambers (TGCs) provide fast hit information used for triggering in the barrel and endcaps respectively.

The bending of tracks in the magnetic field allows the muon spectrometer to measure the transverse momentum of muons. The magnetic fields are achieved by three large "air-core" superconducting toroidal magnets. The barrel toroid is 25 m in length in the direction of the beam-pipe

and radially ranges between 4.7 and 10 meters. Each endcap's toroid is 5 meters in the beam-pipe direction and extends radially to 5 meters. Figure 2.9 shows the magnetic field path integral of an infinite-momentum charged particle travelling through the MS. Except for the barrel-endcap transition region, the field path integral is between 2 and 8 T$\times$m. The air-core toroid design is chosen to minimize the detector material that charged particles travel through. To reach the muon spectrometer, muons must traverse the inner detector and calorimeter. Figure 2.10 shows the most probable energy lost by a muon originating at the IP before it reaches the muon spectrometer. Further, muons travelling through the muon spectrometer may still encounter support structures, magnet coils, and muon chambers. Figure 2.11 shows an illustration of the passive MS material and the number of radiation lengths traversed by muons as a function of (η, ϕ). For much of the barrel, there is about 1.3 X_0 of material.

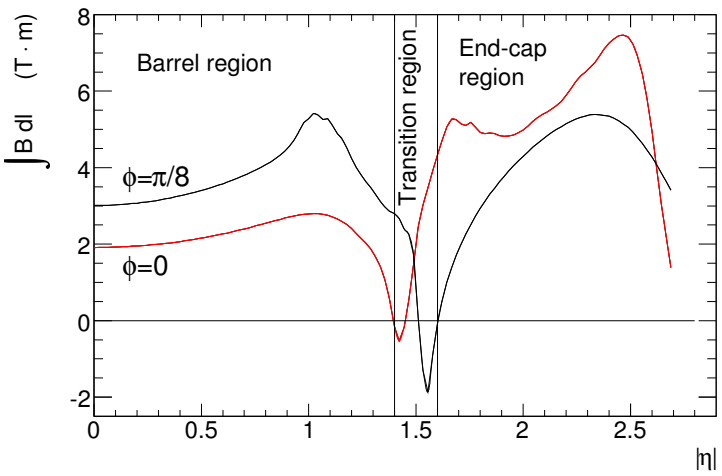

Figure 2.9: Line integral of the predicted magnetic field from the innermost to outermost MDT layer as a function of $|\eta|$ for infinite-momentum charged particles. The red and black curves correspond respectively to the azimuthal angles $\phi = 0$ and $\pi/8$.

The barrel region of the muon spectrometer covers $|\eta| < 1.05$ and is comprised of three concentric cylinders with radii of 5, 7.5, and 10 meters from the interaction point. A gap in detector

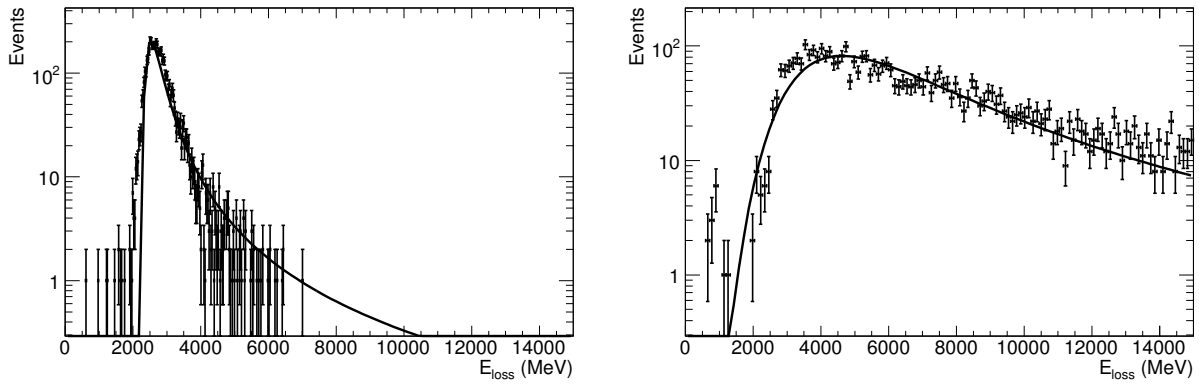

Figure 2.10: Energy loss of $|\eta| < 0.15$ muons with energy of 10 GeV (left) and 1 TeV (right) before reaching MS. The line represents a Landau fit.

coverage exists near $|\eta| = 0$ to provide services for other detectors and the solenoid magnet system. The endcap region of the muon spectrometer covers $1.0 < |\eta| < 2.8$ and is comprised of three wheels at $|z|$ = 7.5, 14, and 21.5 meters. The barrel and endcaps are separated into sixteen chambers, eight large and eight small. Figure 2.12 illustrates the layout of the detector.

The MS is organized into chambers that are identified by their sector. Eight large sectors and eight small sectors are arranged alternatingly radially around the detector with overlap to provide complete angular coverage. Large sectors are between the toroidal coils and small sectors azimuthally overlap the toroidal coils. Chambers are named with a three letter schema, such as BIL or EMS. For most chambers, the first letter refers to whether the chamber is in the barrel or endcap (B or E); the second letter to inner inner, middle, or outer layer (I, M, or O); the third letter to large or small sector (L or S).

Monitored drift tubes

Monitored drift tubes provide precision measurements of muons in the bending (R-Z) plane. The principle of the design is a drift tube 30 mm in diameter, filled with Ar/CO_2 gas in a 93:7 ratio at

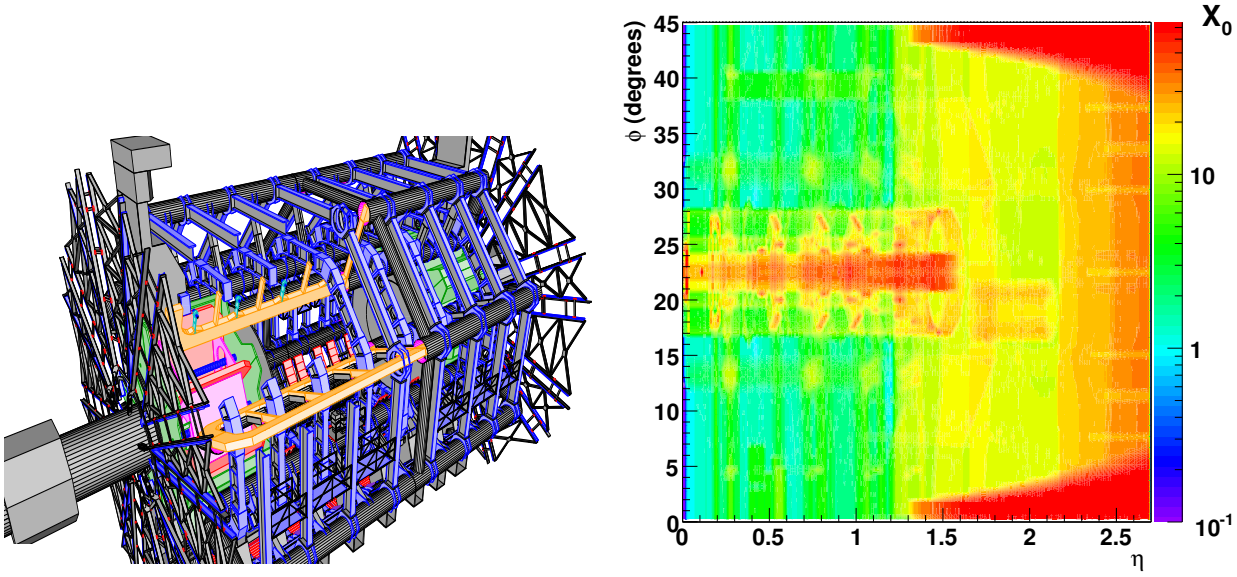

Figure 2.11: Left: Three dimensional view of the passive material in the muon spectrometer. Items included are the barrel and end-cap toroid coils and vacuum vessels and support structures for the calorimeters, muon spectrometer, and toroidal magnets. Right: Material in units of radiation lengths (X_0) traversed by muons after exiting the calorimeter as a function of η and ϕ.

an absolute pressure of 3 bar, with a concentric tungsten-rhenium anode wire of diameter 50 μm. The cross-section of an MDT is shown in Figure 2.13. Tube length ranges from 2 to 5 m, with the tube kept at ground potential and +3080 V maintained on the wire. A muon traveling through the tube will ionize the gas along its trajectory. Electrons from the ionized gas accelerate toward the positive anode wire, colliding with and ionizing the neutral gas along its path resulting in an electron avalanche. The high pressure of the gas gives more interactions and ions than if lower pressure were used. The time delay for the first charges of the avalanche to accumulate on the wire is referred to as the drift time, which is the primary measured physical quantity of MDTs. A drift radius, which represents the distance of closest approach of the particle to the center wire, is computed from the drift time. In the absense of a magnetic field, drift time is approximately proportional to drift radius. The presence of the magnetic field introduced a *coordinate shift*,

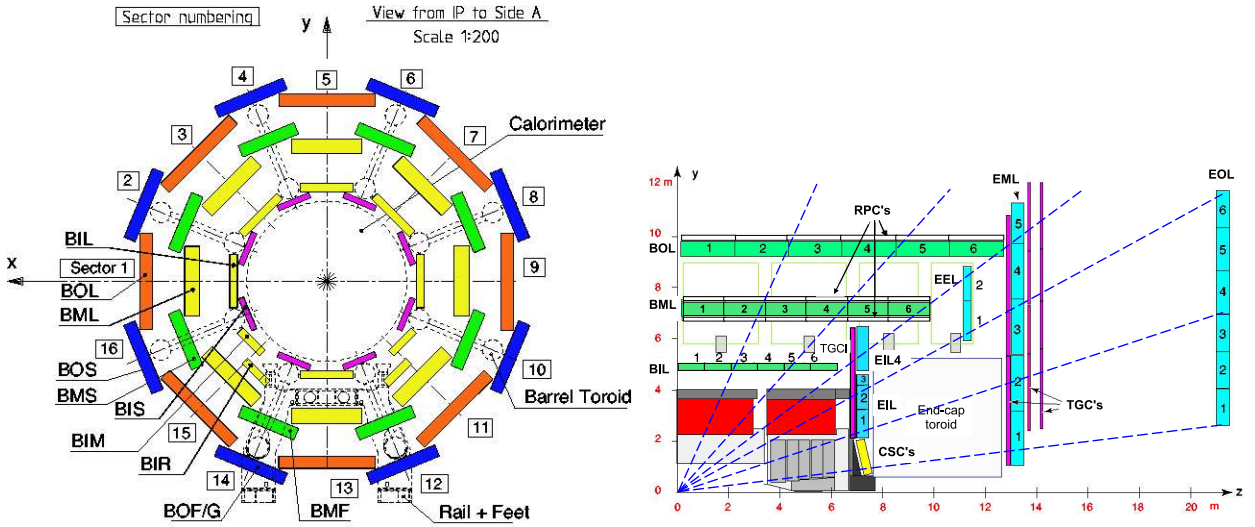

Figure 2.12: Left: Cross section of the barrel muon spectrometer perpendicular to the beam axis. The detector consists of three concentric layers and sixteen chambers. Right: Cross section of the muon spectrometer in the beam axis plane. Straight dashed lines show the trajectory of (non-bending) particles of infinite momentum, illustrating that muons typically traverse three muon stations.

which needs to be applied to the drift radius for accurate MDT measurements [23]. The drift time relation and coordinate shift are shown in Figure 2.14. Within MDTs, the magnetic field is oriented roughly parallel with the wire. The effect of this magnetic field on the charge avalanche is a small reduction on the apparent drift velocity. The circle defined by the drift radius is referred to as the drift circle. The drift time can be as long as 700 ns, which makes the MDT hit response too slow for efficient triggering.

MDT chambers contain two MDT multilayers separated by up to 31 cm. Each MDT multilayer consists of three or four layers of MDTs. Figure 2.15 shows the arrangement of MDTs in a chamber and the drift circles found by a muon traversing the chamber. The MDTs are arranged to provide a high resolution measurement in the R-Z plane, but because they are two to five meters long they cannot measure accurately in the azimuthal direction. The position in ϕ is determined by

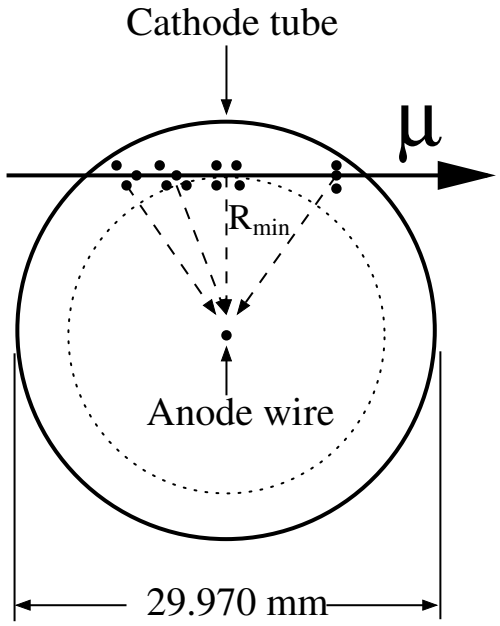

Figure 2.13: The cross-section of an MDT. The drift radius, R_{min}, represents the distance of closest approach of the muon to the anode wire.

combining MDT hits with the azimuthal measurement made by RPCs or TGCs.

Cathode Strip Chambers

The CSCs are multiwire proportional chambers with anode wires oriented in the radial direction in a gas gap with cathode strips on either side. The cathode strips are oriented parallel and perpendicular to the wire, providing measurements of the transverse coordinate and the precision coordinate respectively. A charged particle traversing the chamber creates a charge avalanche that is spread over three to five cathode readout strips. Charges collected on sequential strips is interpolated to provide a measurement of the charged track position, and the charge collected on the wire is not read out. The layout of a CSC gas gap is illustrated in Figure 2.16. Each CSC contains four independent gas gaps, resulting in four independent η and ϕ measurements for each track.

CSC chambers are used in the innermost layer of the MS endcaps in the region $2.0 < |\eta| < 2.7$.

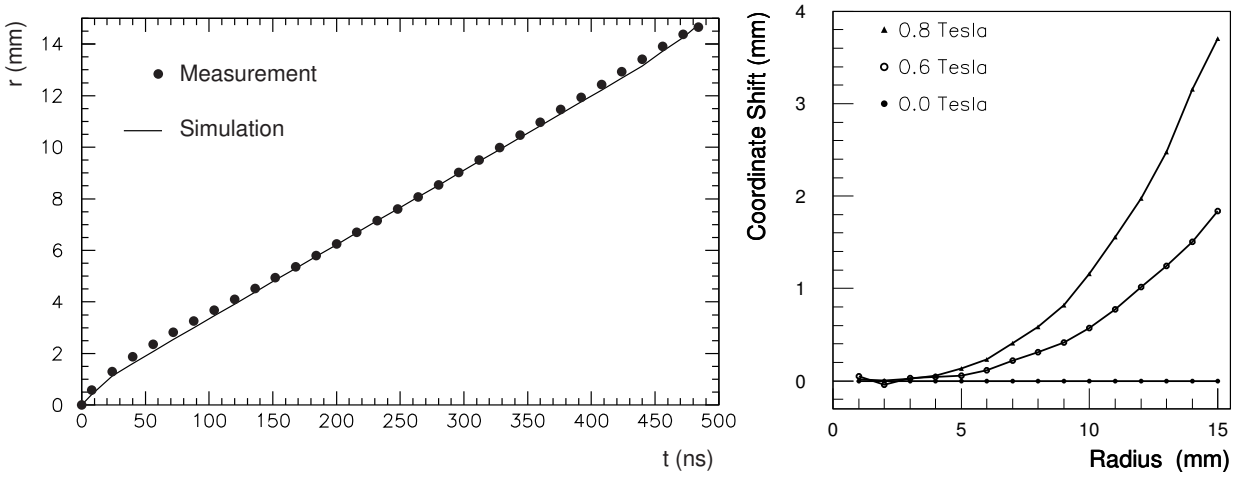

Figure 2.14: Left: Relationship of measured drift time and cooresponding drift radius in the absence of a magnetic field. Right: Correction to drift radius caused by a magnetic field as a function of the drift radius for various field strengths.

The use of CSCs in this detector region is due to the very high rates in the inner layer, forward region of the detector. Safe operation for MDTs requires a hit rate of less than 150 Hz/cm^2; for CSCs the upper rate is about 1000 Hz/cm^s. CSCs make measurements with a resolution of 60 μm.

Resistive Plate Chambers

The RPCs are gaseous parallel-plate (wireless) detectors that provide triggers and azimuthal angle measurement in the barrel MS. Two parallel plates are separated by 2 mm of insulating spacers. An electric field of 4.9 kV/mm allows ionizing tracks to produce charge avalanches that are collected on the anode. The 2 mm gas gap consists of a mixture of $C_2H_2F_4/\mathrm{Iso}-C_4H_{10}/SF_6$ (94.7/5/0.3). The cross-section of an RPC chamber is shown in Figure 2.17.

Three RPC chambers are arranged on the middle and outer barrel MS stations. Two chambers are present in the middle MS station, on either side of the MDT chamber. A third RPC chamber is located on the outer MS station. RPC chamber locations are indicated in Figures 2.12 and 2.18. The three stations are called RPC1, RPC2, and RPC3 to refer to the inner, middle, and outer station.

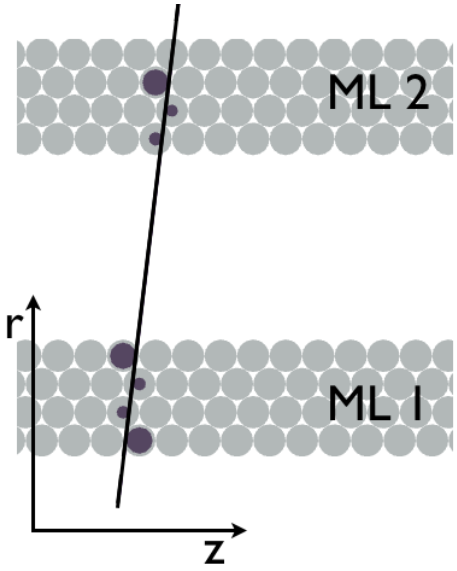

Figure 2.15: Arrangement of the MDTs in a the BIS chamber with two multilayers and four layers of MDTs per multilayer. The line represents the segment of a muon passing through the chamber, and the circles are reconstructed drift circles.

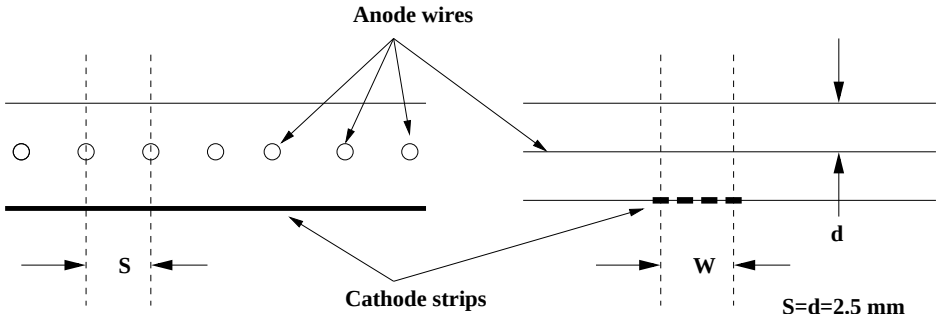

Figure 2.16: Structure of the CSC chamber in the plane of the wire. The same distance, 2.5 mm, is used for wire spacing (s) and distance between cathode and wire (d).

The small distance between RPC1 and RPC2 provides a low-p_{T} trigger in the range 6-9 GeV. The longer lever arm between RPC1 and RPC3 permits the trigger to select high momentum tracks

with p_{T} of at least 9 GeV. Each RPC chamber consists of two layers, each measuring η or ϕ. A track going through three layers delivers six hits, and the redundancy of hits allows loosening the hit requirements to trigger. A low-p_{T} track can reconstruct even if one of the four hits is not reconstructed in the RPC1 or RPC2 stations. Similarly, a high-p_{T} track can reconstruct even if one of the two hits is not reconstructed in the RPC3 station. This coincidence scheme results in low fake rates from noise while keeping trigger efficiency high with a $\sim$3% detection inefficiency per layer.

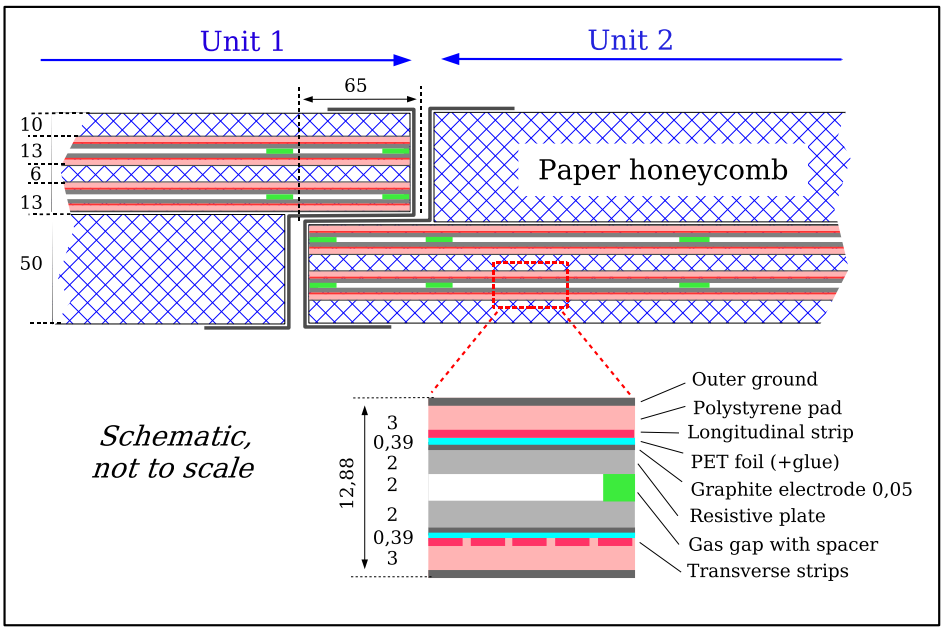

Figure 2.17: Cross section through an RPC where two units are joined when forming a chamber. Each unit has two gas volumes, each supported by a spacer. Four resistive electrodes and readout plates read in the transverse and longitudinal directions. Dimensions are given in mm.

Thin Gap Chambers

The TGCs are multi-wire proportional chambers that provide triggering and azimuthal angle measurements in the endcaps. They consist of a gas volume that contains a wire plane and two cathodes.

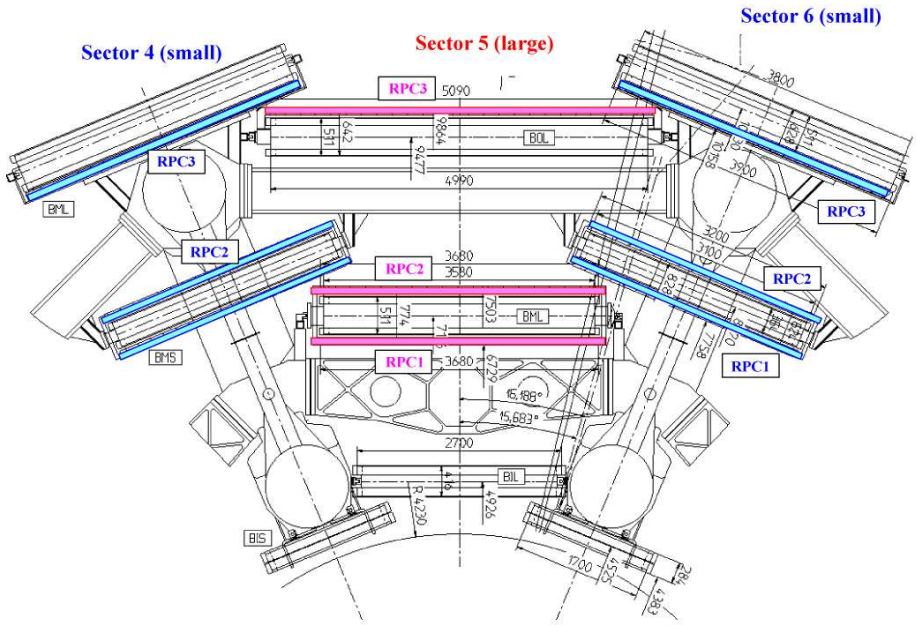

Figure 2.18: Arrangement of the RPC chambers. RPC1 and RPC2 are on the inner and outer edges of the middle MDT layer. RPC3 is outside the MDT chamber in large sectors and inside in small sectors.

The gas volume is a (55:45) mixture of $CO_2 : n-C_5H_{12}$, with a +2900 V potential on the wires. The wires are oriented for measuring the longitudinal coordinate, η, and the cathode is divided into strips perpendicular to the wire for measuring the azimuthal angle.

One layer of TGCs is present on the inner MS layer and two on the middle layer. In the inner layer, there is one plane of doublet units. In the middle chamber, seven layers are arranged in one plane of triplet chambers called M1 and two plains of doublet chambers called M2 and M3. The M3 doublet is referred to as the pivot plane and its layout is optimized that, to a good approximation, there are no overlaps or holes in the plane. The arrangement of TGC chambers is shown in Figure 2.19.

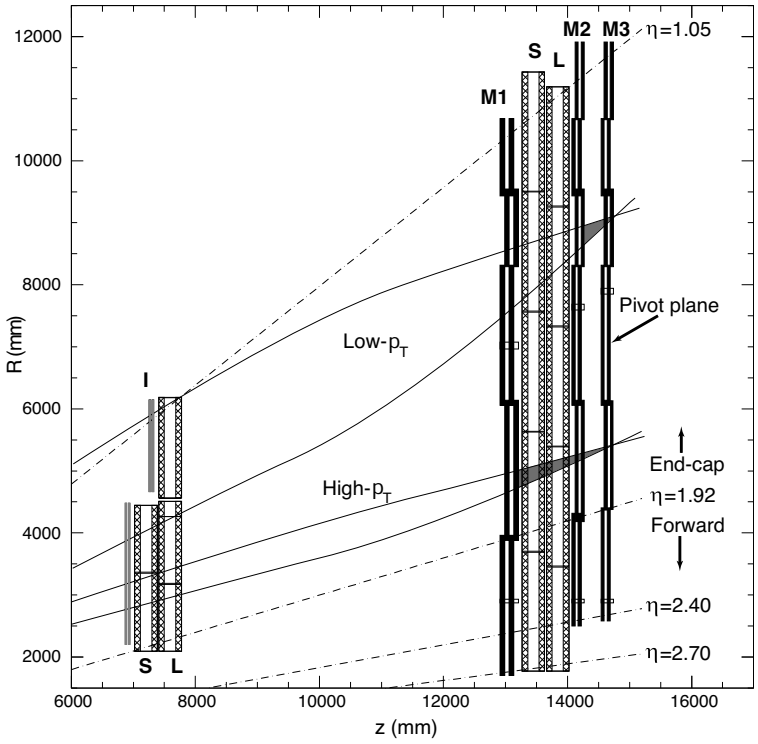

Figure 2.19: Arrangement of TGC chambers on the inner (marked I) and middle (marked M) MS layers. The location of MDT chambers in small (S) and large (L) is shown for reference.

2.2.5 Luminosity Detectors

Luminosity is primarily measured in ATLAS using the LUCID and BCM systems. Both detectors measure particle flux in the forward beam direction, giving an inelastic interaction rate, which is proportional to instantaneous luminosity.

LUCID

The luminosity measurements using the Cerenkov integrating detector (LUCID) aids in determining the instantaneous luminosity of collisions as well as monitoring the collision conditions. Two such detectors are installed, one in each end-cap, at $|z| \approx 17$ m from the interaction point with

a radial distance from the beam line of 10 cm, corresponding to the very forward region of the detector at $|\eta| \approx 5.8$. Each detector is composed of twenty tubes that are 1.5 m long, 15 mm in diameter. The tubes are filled to an absolute pressure of about 1.3 bar with C_4F_{10}, which provides a Cerenkov threshold of 2.8 GeV for pions and 10 MeV for electrons. When a particle traverses the tube, Cerenkov light is emitted that reflects internally and until reaching the end of the tube where it is detected by a photomultiplier tube, which allows for the number of particles per tube to be measured.

BCM

The beam conditions monitor (BCM) is built in two stations, each with four modules. Each module has two radiation-hard diamond sensors that are read out by radiation-tolerant electronics. The stations are placed around the interaction point at $|z| = \pm 184$ cm, $R = 5.5$ cm, corresponding to $|\eta| = 4.2$. In addition to measuring luminosity, the BCM can use timing measurements to identify whether a particle comes from the interaction point or a background process, and can request beam dumps in the scenario that an unstable beam could damage ATLAS.

2.3 Trigger System

Proton collisions in ATLAS took place every 50 ns in 2012, and writing a measured event to disk requires approximately 1.3 Mbytes. The amount of processing and disk space necessary to keep all events is impractical, so a trigger scheme is implemented to select the events with physics significance and discard the large background of low-energy scattering events.

The trigger systems selects events in three sequential steps, called level 1 (L1), level 2 (L2), and the event filter (EF). Each level is a refinement on the last level's requirements and can add additional selection requirements. The first level uses limited detector information to make a decision within 2.5 μs, which reduces the rate to 75 kHz. The L2 and EF are able to access more detector information and reduce the final trigger rate to about 300 Hz.

2.3.1 The Level-1 Trigger

The L1 trigger rapidly reduces the event rate using reduced detector information. As previously mentioned, the L1 trigger is fed events at up to 40 MHz and selects events at 75 KHz. Each event is processed within 2 μs by considering a subset of detector data at reduced granularity. Objects identified at L1 are jets (including electrons, photons, τ-leptons), muons, and $E_{\mathrm{T}}^{\mathrm{miss}}$.

Jets are constructed from so-called "trigger towers", which are the sum of calorimeter cell energies in reduced granularity bins of size 0.1 x 0.1 in η x ϕ. Sliding window algorithms are in place that make requirements on adjacent trigger towers to select calorimeter regions of interest that are identifies as electrons/photons or τ/hadrons. The calorimeter information is also used to make global sums of scalar and missing transverse energy.

Muons are identified by looking for coincidences between layers in RPC or TGC hits. The muon p_{T} is estimated by the muon's deviation from a straight trajectory. In the barrel, the L1 muon trigger algorithm operates by finding a hit in the middle RPC station, sometimes called the pivot plane. For low-p_{T} muons, a search is then made in the inner RPC layer on a road whose center is a line connecting the pivot plane hit with the interaction point. The width of the road is defined by the desired muon p_{T} cut (i.e. a high p_{T} cut results in a narrow road). A similar approach is employed in the endcaps. The doublet of TGCs farthest from the interaction point, referred to as M3, acts as the pivot plane. Roads are opened up on the M1 and M2 TGC layers to look for coincidence. Low p_{T} muons are identified with coincidence hits in the M2 layer, whereas high p_{T} muons require coincidence hits in M1 and M2. The barrel and endcap roads are shown in Figure 2.20. No more than two L1 Muon RoIs can be identified per MS chamber; the two highest p_{T} RoIs are used downstream by the central trigger processor.

The L1 trigger identifies Regions of Interest (RoIs) associated with calorimeter towers and muon roads. These RoIs are used in later stages of trigger selection, as will be seen. A trigger menu, a list of triggers, is defined to choose what events are accepted by the L1 trigger based on the scalar energy sum, $E_{\mathrm{T}}^{\mathrm{miss}}$, and the presence of jets, electrons, photons, τ-leptons, and muons that exceed assigned p_{T} requirements.

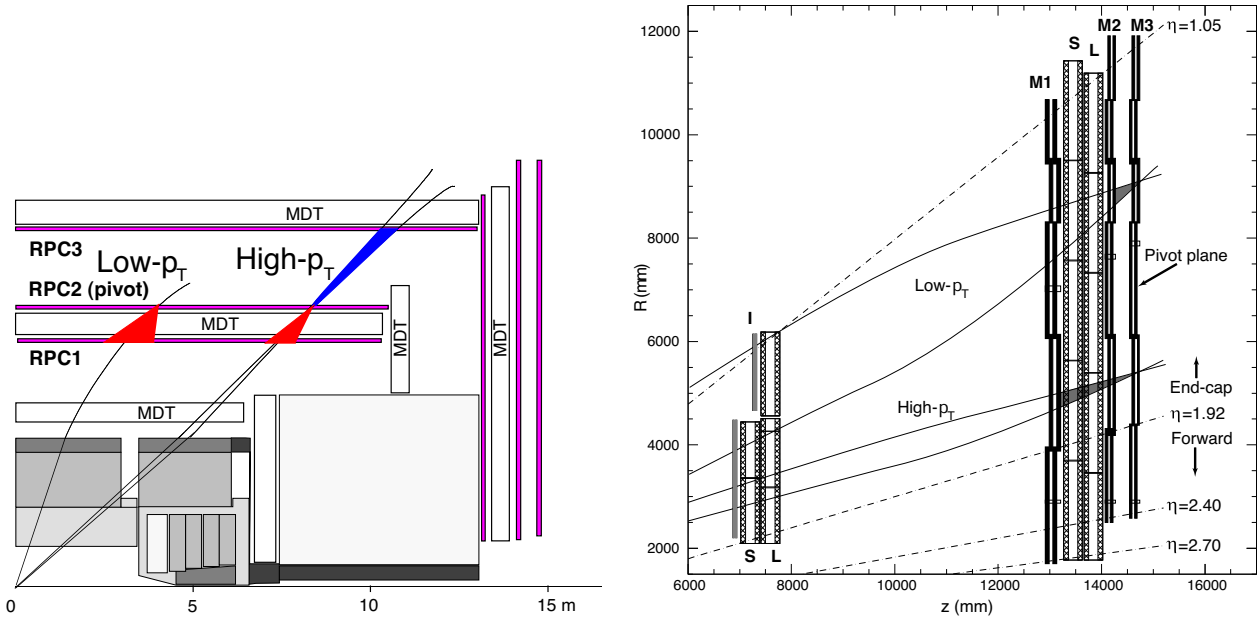

Figure 2.20: Illustration of L1 muon trigger coincidence schemas. Left: A trigger hit in the middle RPC plane opens up regions of coincidence in the inner plane for low p_{T} muons and both inner and outer plane for high p_{T} muons. Right: A trigger hit in the M3 TGC plane opens up regions of coincidence in the M2 plane for low p_{T} muons and in the M1 and M2 plane for high p_{T} muons.

The Level-2 Trigger and Event Filter

The L2 trigger is seeded by L1 RoIs. At L2, information at full detector granularity is available in regions around the L1 RoIs, corresponding to about 2% of the total detector information. The L2 trigger uses the more detailed information it has available to better refine event selection and reduce selection rate to about 3.5 kHz.

After passing the L2 trigger, events are finally selected by the EF. The EF has information at full detector granularity for the entire detector. The EF selects events at a rate of about 300 Hz, and events selected by the EF are designated for permanent storage to disk and processed using more time-consuming offline reconstruction algorithms for use in analyses.

Chapter 3

EVENT SIMULATION

Signal events must be simulated in order to understand what the detector sees in the case that a theoretical physics model exists in nature. Physics events are simulated by a Monte Carlo (MC) method, which is to say detector events are simulated by sampling particle properties from a probability distribution. The events are taken through the consecutive steps called *event generation*, *simulation*, and *digitization* in order to arrive at a fully simulated signal that is in the same format as data. Event generation accounts for the hard interaction taking place within the collision and includes the underlying event. Simulation places the hard interaction at the collision point within the detector. The particles' trajectories through the magnetic field and interactions with detector material are simulated, as well as the detector's response. Digitization then takes the detector hits from the simulated process, adds to it hits from pileup events that are present in the same bunch crossing, and transforms those hits into the digital signature that would be present in an actual collision event.

For most simulation in ATLAS, the added pileup is comprised of minimum bias events that are also produced by MC simulation. However, for this analysis zero bias data[1] events are overlaid on the simulated hard MC event; for this reason the MC used in this analysis is sometimes referred to as "overlay MC" [24]. Since overlay MC's pileup events are taken from actual data, the events will contain backgrounds that would otherwise not be included in the simulation. These include cavern background[2], cosmic interactions, and beam halo.

---

[1]Zero bias events are randomly chosen proton-proton collisions. Bunches are selected by identifying an event containing L1 electron with $p_{\mathrm{T}} > 14$ GeV, chosen since it is a relatively high-p_{T} trigger. This bunch's next crossing, on its next pass around the accelerator, is the zero bias event. The use of a high-p_{T} trigger gives a rate proportional to instantaneous luminsosity in that bunch crossing. The zero bias trigger is highly prescaled so as to make a trigger rate of $\sim$1 Hz.

[2]The cavern background is a buildup of low energy neutrons and photons in the ATLAS detector cavern due to

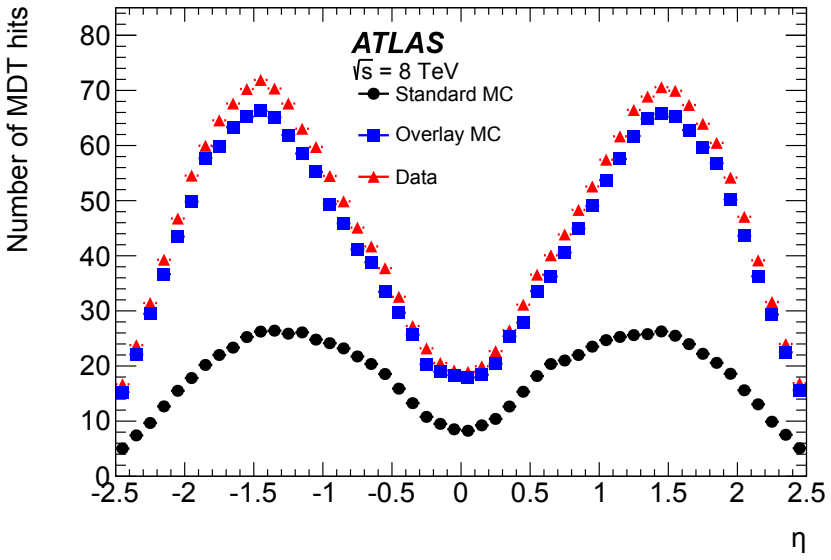

Figure 3.1: Average number of MDT hits from non-collision backgrounds within a $\Delta R < 0.6$ cone as a function of η for standard MC, background overlay MC, and data events.

The need for zero bias overlay is demonstrated by looking at background MS hits. The MS background is quantified by studying regions of the detector with no calorimeter activity. Events from the good run list are selected that pass the EF_j360_a4tchad trigger[3], which requires a leading jet with $E_{\mathrm{T}} > 360$ GeV, and have two good back-to-back leading jets ($|\Delta\phi| > 2.14$). For each event, a random (η, ϕ) is chosen. If there are no jets with $E_{\mathrm{T}} > 25$ GeV within $\Delta R < 1.6$ of the (η, ϕ) axis, then the number of MDT hits within $\Delta R < 0.6$ of the (η, ϕ) axis is recorded. The comparison of data and MC, shown in Figure 3.1, demonstrates that without zero bias overlay the distribution of MDT hits in data is not accurately reproduced by MC. The slight discrepancy that

the intense, high energy proton beams collided there. These particles' interactions with the detector give rise to increased number of random detector hits, sometimes called *detector hit occupancy*.

[3]The "a4tchad" suffix denotes the anti-k_t jet-finding algorithm [25] with a cone radius of 0.4 ("a4') using topological clusters ("tc") and calibrated at the hadronic scale ("had"). These suffixes are appended to the trigger names in order to avoid confusing them with triggers that have identical thresholds but different reconstruction algorithms or tunings.

remains after background overlay is likely the result of the overlay procedure, which converts the digital measurement of zero bias events to an estimated electrical pulse in the detector and, after adding the hard MC process, re-digitizes the event.

For this analysis, two theoretical benchmark models and five "multijet MC samples" are simulated. Zero bias overlay samples are used for each signal MC and multijet MC sample. Each sample contains 400,000 events except for the lowest energy multijet MC sample, for which two million events were generated in order to reduce statistical uncertainty. Overlay MC uses zero bias data that is sampled throughout 2012, resulting in a pileup distribution μ that constructed to match the distribution observed in 2012 data.

3.1 Simulation of Long-Lived Particle Benchmark Models

A range of MC samples have been produced for the Scalar boson and Z' models. The Scalar boson and Z' samples include different Scalar boson, Z', and π_v masses and different π_v proper lifetimes. The chosen benchmark samples are listed in Tables 3.1 and 3.2. The masses are chosen to explore the effect of kinematics on the detection of long-lived particles. The proper lifetime values are chosen to give a significant fraction of decays throughout the entire ATLAS detector volume. The final analysis is not dependent on the simulated mean proper lifetime of the long-lived particle. For the Z' model, two lifetimes are simulated for each Z', π_v mass point combination.

The scalar boson model events are generated in PYTHIA8 [26, 27]. The scalar boson is produced via gluon fusion because the standard model Higgs production is dominated by gluon fusion for the scalar masses considered. The process is simulated using the production process "HiggsBSM:gg2H2", built into PYTHIA8. With this option, Pythia produces an MSSM scalar H^0 by gluon fusion that decays to two pseudoscalars A^0. Since these particles' properties match that of the scalar boson model we consider, it is convenient to treat A^0 as our model's π_v and H^0 as our model's scalar boson. For each simulation, the mass of the scalar boson and π_v as well as the π_v's lifetime are specified. Pythia correctly simulates the A^0's branching fraction to fermion pairs with a branching ratio that is proportional to the fermion's mass squared.

The Z' events are simulated in a two-step process. An external generator, HvGen, is used to

Dataset number	Scalar boson mass [GeV]	π_v mass [GeV]	proper lifetime [cm]
159220	100	10	450
159221	100	25	1250
159222	126	10	350
159223	126	25	900
159224	126	40	1850
159225	140	10	275
158346	140	20	630
159226	140	40	1500
188548	300	50	800
188549	600	50	500
188550	600	150	1700
188551	900	50	500
188552	900	150	1300

Table 3.1: Mass parameters for the simulated Scalar boson benchmark models.

simulate Z' production and its decay to hidden-sector particles with the model's v-QCD hadronization. The decay of π_v to SM particles and subsequent decay, showering, and hadronization of SM partons are simulated using PYTHIA8. All generated events include production and decay kinematics. The parametrization at leading order used for the proton parton distribution function for the Scalar boson and Z' simulations is MSTW 2008.

3.2 Simulation of Multijet Samples

Simulated multijets are produced in eight sample varieties, refered to as JZXW where $X = 0, 1, ..., 7$. The multijet events are generated across a broad range of leading jet energy and assigned a cor-

Dataset number	Z' mass [TeV]	π_v mass [GeV]	π_v mean proper lifetime [m]
158745	1	50	0.5
158746	1	50	1.5
158747	2	50	0.5
158748	2	50	1.5
158749	2	120	0.5
158750	2	120	1.5

Table 3.2: Mass and mean proper lifetime parameters for the simulated Z' benchmark models.

Minimum Jet E_T [GeV]	Maximum Jet E_T [GeV]	Offline Prescale
0	80	50
80	140	30
140	200	20
200	300	10
300	400	5
400		1

Table 3.3: DESD_CALJET offline prescale used for selecting data events for storage in ESD format. Jet E_T corresponds to a cut on AntiKt4TopoEMJets at the EM+JES scale.

JZXW	AntiKt6 TruthJet PT range [GeV]	Cross-section (nb)	Filter efficiency	Number of events
JZ3W	200-500	5.4419E+02	1.2187E-03	2,000,000
JZ4W	500-1000	6.4453E+00	7.0821E-04	400,000
JZ5W	1000-1500	3.9740E-02	2.1521E-03	400,000
JZ6W	1500-2000	4.1609E-04	4.6843E-03	400,000
JZ7W	2000+	4.0636E-05	1.4600E-02	400,000

Table 3.4: Summary table of default MC multijet samples.

responding statistical weight. The samples JZ1W-JZ6W are generated with uniform statistics in leading truth jet p_{T}, and consequently an MC generation per-event weight must be applied to give the p_{T} spectrum that is found in data. The samples JZ0W and JZ7W are generated with falling leading truth jet p_{T} spectrum to match data, so the MC generation per-event weight has a value of 1 for every event in those samples. Because MC events are generated with uniform p_{T} distributions in each JZXW sample and the different slices have different production cross sections and efficiencies, a per-event weight must be applied. Each event's relative weight is calculated by the following equation:

$$\text{Event Weight} = (\text{MC Per-Event Weight}) \times (\text{Filter Efficiency}) \times (\text{Cross-section}) \div (\text{Num Events Generated})$$

The MC generation event weight has been constructed so the event weight can be scaled to data by multiplying the event weight by the integrated luminosity of the data sample.

The multijet samples are used to understand how well simulation can represent data events. In the context of reconstructing vertices in the MS, this is a question of how well simulation can simulate charged particles that shower in the MS. To select events with showers in the MS, a comparison between data and MC must be performed on events with jets that punch through the calorimeter and continue to shower in the MS. These "punch-through" jets are studied because

there are no known long-lived particles for making such a study.

The properties of punch-through jets can be compared between simulation and data. Events are selected from the multijet samples by using the EF_j360_a4tchad trigger, which requires a leading jet with $E_{\mathrm{T}} > 360$ GeV. This effectively removes all events from JZ0W-JZ2W. The selected events are then required to have a punch-through jet. An event is identified to contain a punch-through jet if the leading or sub-leading jet is located in the "punch-through region" of the calorimeter, $0.7 < |\eta| < 1.0$ or $1.5 < |\eta| < 1.7$, and has at least 30 GeV of $E_{\mathrm{T}}^{\mathrm{miss}}$within $|\Delta\phi| < 0.6$ of the jet axis. The jet is further required to have 250 (300) MDT hits within a cone of $\Delta R < 0.6$ of the jet axis.

Figure 3.2 shows the pT distribution of the punch-through jet and the jet recoiling opposite the punch-through jet. Figure 3.3 shows the number of tracklets in a cone around the punch-through jet when the jet is in the barrel or endcaps. Reasonable agreement in structure is seen between the two samples, demonstrating the validity of using punch-through jets.

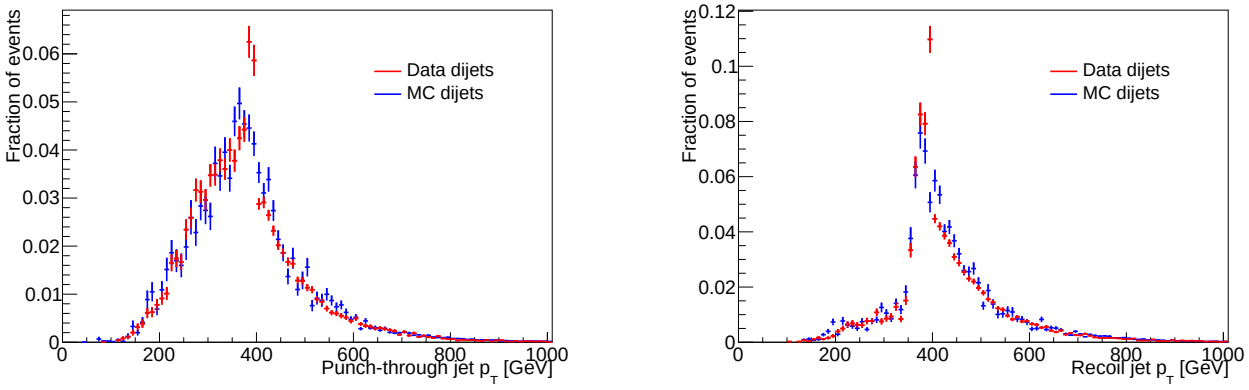

Figure 3.2: Jet energy spectrum of punch-through jets in data and MC.

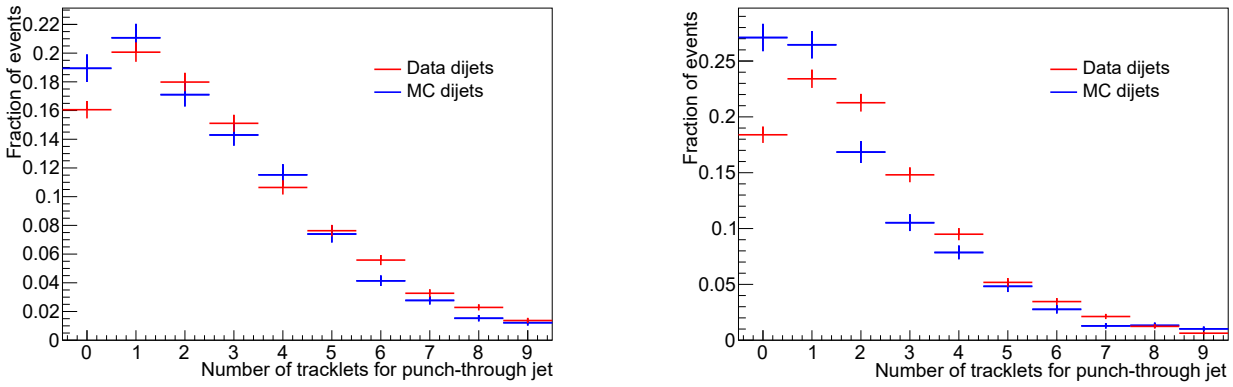

Figure 3.3: Number of tracklets within a cone of $\Delta R < 0.6$ of a punch-through jet in data and MC for the barrel (left) and endcaps (right).

Chapter 4

SIGNATURES OF DISPLACED DECAYS

Long-lived particles can have lifetimes comparable to the ATLAS detector dimensions. Due to the exponential distribution of time before particle decay, this results in decays throughout the detector volume for a range of LLP lifetimes. Figure 4.1 shows the probability for a long-lived π_v particle to decay in the fiducial detector volume as a function of its mean proper lifetime. It shows that for a large range of lifetimes a significant fraction of decays occur throughout the ATLAS detector.

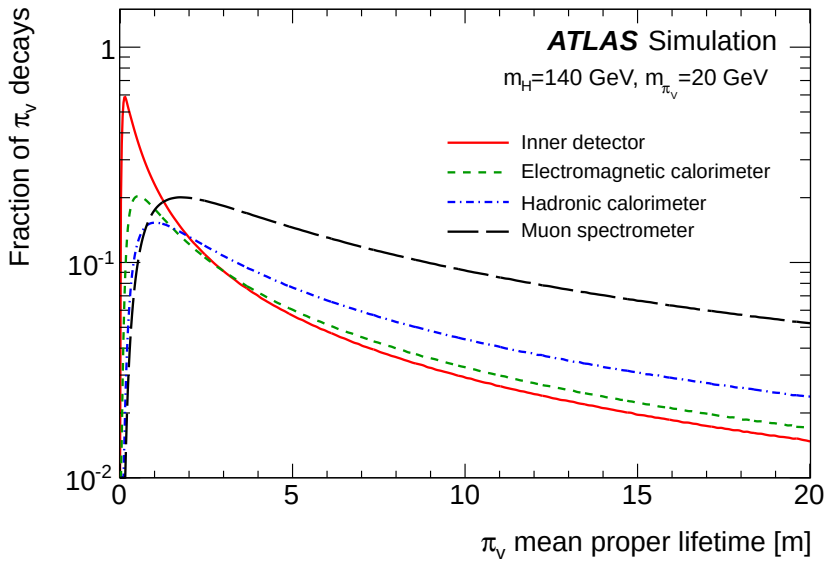

Figure 4.1: The probability of a long-lived π_v particle to decay in different regions of the ATLAS detector as a function of its proper lifetime.

Most ATLAS triggers are designed to select physics signatures that originate at the IP. Events

with displaced decays may be highly prescaled or not selected at all by these IP-centric triggers since they may not contain high energy tracks, jets, or other standard physics signatures. Special long-lived particle triggers have been implemented to select the physics signatures of a long-lived particle decaying far from the IP. Similarly, standard offline objects may not correctly reconstruct an identifiable displaced decay signature. To avoid this avenue of failure, displaced vertex reconstruction in the ID and MS has been implemented. The displaced decay trigger and vertex reconstruction techniques are described in the following sections.

4.1 Decays in the Muon Spectrometer

Decays occuring within the MS result in a large number of charged hadrons contained in a narrow detector region. In such events, a large number of L1 muon RoIs are reconstructed from the hits of the hadrons. Figure 4.2 shows the distribution of number of L1 muon RoIs reconstructed in a $\Delta R = 0.4$ cone around a π_v decay in the MS. Figure 4.3 shows the average number of RoIs reconstructed in a $\Delta R = 0.4$ cone as a function fo the decay position of the π_v. When many L1 Muon RoIs are present in an event, a cluster of RoIs can be identified. A Muon RoI Cluster is defined in the barrel (endcaps) as a cone of $\Delta R = 0.4$ that contains at least 3 (4) L1 muon RoIs, each with $p_T \geq 10$ GeV.

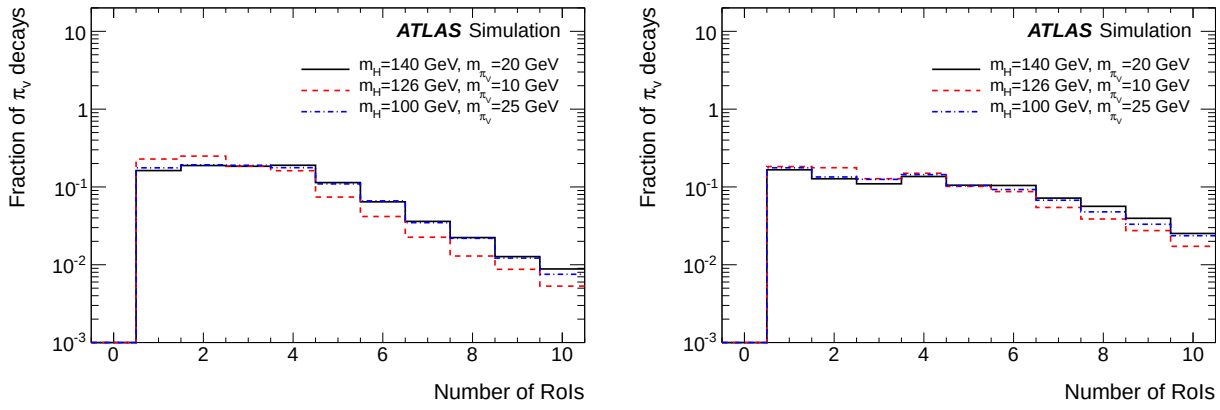

Figure 4.2: Distribution of the number of L1 muon RoIs in a $\Delta R = 0.4$ cone around a π_v that decays in the MS in the barrel (left) and endcaps (right).

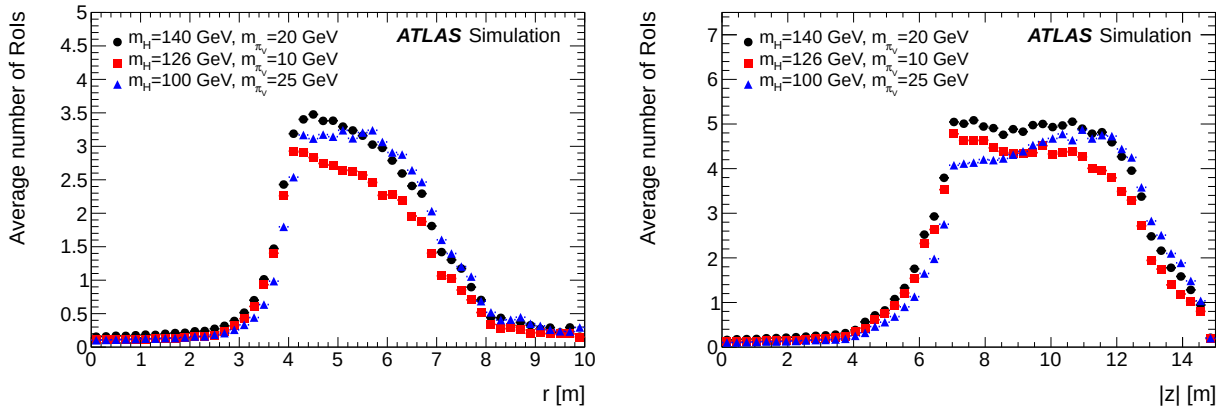

Figure 4.3: The average number of L1 muon RoIs in a ΔR = 0.4 cone as a function of the position of π_v decay in the barrel (left) and endcaps (right).

When a long-lived neutral particle decays in the MS, it produces a jet shower that travels outwardly from its decay position. Consequently, the long-lived particle does not leave ID hits or calorimeter energy deposits between the collision point and its decay position. Tracks or calorimeter energy exist at low levels due to pileup and the underlying event, but they are not strongly correlated with the path of flight of the LLP. Figure 4.4 shows the fraction of events that have no L2 ID tracks with $p_T > 5$ GeV within a ΔR cone of the π_v decay position. Figure 4.5 shows the fraction of events that have no L2 jets with $E_T > 30$ GeV and $\log_{10}(E_{HAD}/E_{EM}) < 0.5$ within a ΔR cone of the π_v decay position. Jets with primarily hadronic energy are allowed in order to increase acceptance in the case of a LLP decaying in the hadronic calorimeter.

4.1.1 The Muon RoI Cluster Trigger

To select events decaying within the HCal or MS, a trigger called the Muon RoI Cluster trigger was implemented [28]. The trigger selects events using L1 muons, L2 tracks, and L2 jets. The centroid of a Muon RoI Cluster containing the largest number of L1 Muon RoIs of $p_T \geq 10$ GeV is found. If an ID track with $p_T > 5$ GeV is found within ΔR < 0.4 of the Muon RoI Cluster centroid, the trigger is not passed. Similarly, if a L2 jet with $E_T > 30$ GeV, $\log_{10}(E_{had}/E_{EM}) < 0.5$

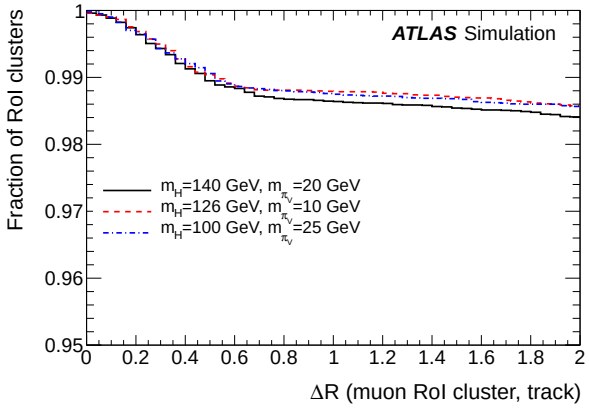

Figure 4.4: Fraction of RoI clusters in signal events with no L2 ID tracks with $p_{\mathrm{T}} > 5$ GeV within a cone of size ΔR.

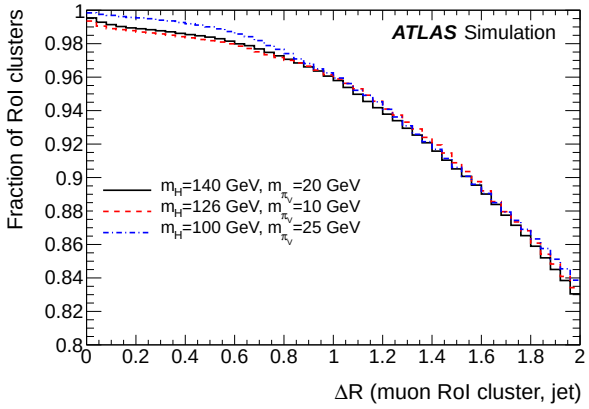

Figure 4.5: Fraction of RoI clusters in signal events with no L2 jets with $E_{\mathrm{T}}>$ 30 GeV, $\log_{10}(\mathrm{E_{had}/E_{EM}}) < 0.5$ with jet axes within a cone of size ΔR.

is found within $\Delta\mathrm{R} < 0.7$ of the Muon RoI Cluster centroid, the trigger is not passed. Otherwise, the Muon RoI Cluster is considered isolated with respect to ID tracks and jets, and the trigger logic is satisfied. A schematic of the trigger sequence is shown in Figure 4.6.

To understand how effective the Muon RoI Cluster trigger is at selecting LLP decays, the

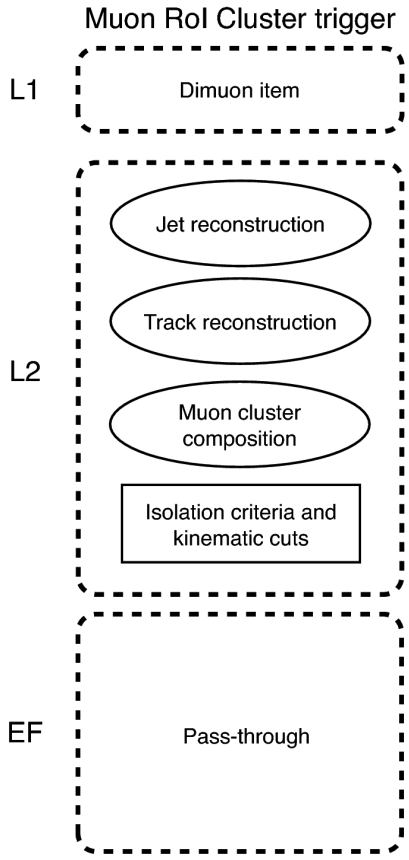

Figure 4.6: Schematic diagram of the sequence of Muon RoI Cluster trigger algorithm. The ovals represent trigger algorithms to reconstruct features and rectangles represent trigger algorithms that apply cuts using the reconstructed features.

trigger's efficiency is measured for the simulated scalar boson samples. Since the Muon RoI Cluster trigger identifies a single region of significant MS activity and the LLPs are typically well separated in the scalar boson sample, efficiency is shown on a per-LLP basis. The efficiency is defined as the fraction of decaying events that pass the RoI Cluster trigger. Figure 4.7 shows the trigger's efficiency in the barrel and endcaps as a function of LLP decay position.

Locations of Muon RoI Cluster in 2012 data events selected by the Muon RoI Cluster trigger is shown in Figure 4.8. The relatively low quantity of clusters near $\eta = 0$ is partially due to a gap

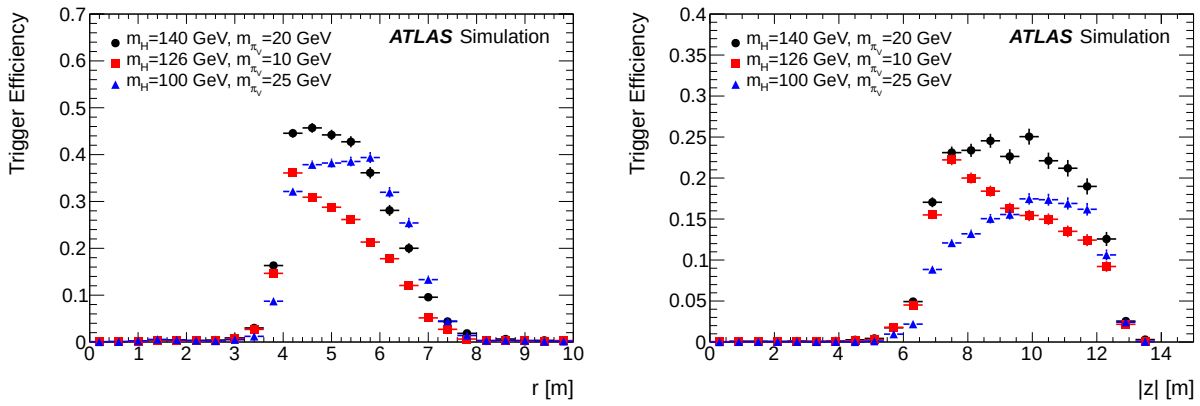

Figure 4.7: Efficiency of the Muon RoI Cluster trigger in the barrel (left) as a function of radial decay position, r, and in the endcaps (right) as a function of the longitudinal decay distance, $|z|$. The uncertainty bars show only statistical uncertainty.

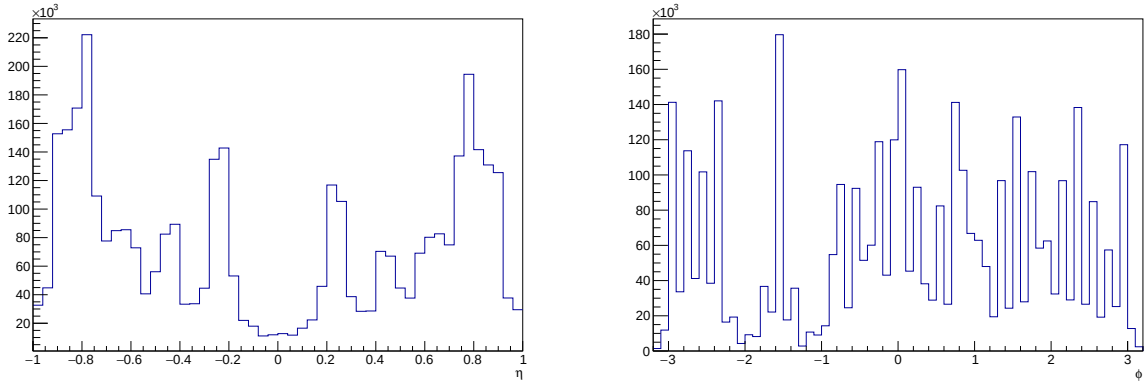

Figure 4.8: Location of barrel Muon RoI Clusters from 2012 data passing the RoI Cluster trigger. The left figure shows the distribution of clusters in η and the right figure shows the location in ϕ.

in the RPC system. The presence of more vertices in $\eta < 0$, near $\phi = 0$, is attributed to beam halo background.

4.1.2 Muon Spectrometer Vertex Reconstruction

When neutral particles decay in the MS, their decay products will produce charged particles. Since ATLAS' MS has an air-core toroid, there is relatively little material in this section of the detector. The lack of significant material allows hadrons produced in LLP decays to travel with relatively few material interactions and showers. This makes it possible to reconstruct these charged tracks and find a common point of origin of the hadrons, called a vertex. A novel pattern finding algorithm is implemented to achieve this goal [29].

MS vertices are reconstructed in a series of steps to logically categorize the MS activity and recognize the pattern of an MS vertex. The sequence is composed of reconstructing the MDT hits into multi-layer segments, combining multi-layer segments into tracklets, and finally building tracklets into MS vertices. These steps are described in the following sections.

Multi-Layer Segment and Tracklet Reconstruction

The MDT hits within a single MDT multi-layer are reconstructed into multi-layer (ML) segments from three or more collinear hits. The segments are reconstructed using a modified version of the MOORE[1][30] segment finding algorithm. The algorithm keeps all ML segments if the χ^2 probability of the hits being consistent with a straight-line segment is greater than 5%.

Tracklets are reconstructed by combining two ML segments, one from the first and one from the second MDT multi-layers. The separation between the MDT multi-layers provides a powerful pattern recognition tool, since in the barrel regions that contain a magnetic field the charged particles bend giving a measurement of the p_{T}.

Segments from the first and second multi-layer are combined to make a tracklet if they pass cuts on two parameters, $\Delta\alpha$ and Δb. The parameter $\Delta\alpha$ measures the difference in angle of the two segments in the chamber. For well-reconstructed tracklets in regions with no magnetic field,

[1]The Muon Object Oriented REconstruction (MOORE) algorithm is a software package designed for ATLAS MS track reconstruction. In Hough space, the coordinates represent a hypothesis track. The Moore algorithm performs a coordinate change and Hough transform on hits, allowing candidate tracks to be identified as the maxima in Hough space.

namely the endcaps and the BIS and BOS chambers, $\Delta\alpha$ should be consistent with zero within measurement uncertainty. In the barrel, $\Delta\alpha$ represents the bending of the charged track and allows a measurement of tracklet p_{T}. The parameter Δb measures the shorter of the two distances of closest approach of one ML segment to the point that the other ML segment crosses the midway point of the MDT chamber. Figure 4.9 illustrates how Δb is measured.

ML segments and tracklets are reconstructed from MDT hits, which can not give a precise measurement in ϕ. For reconstructed muons, the track position is measured in ϕ by taking advantage of precision ϕ measurements in the RPC or TGC systems. A similar procedure can't be used for LLP decays in the MS since the system contains hundreds of trigger hits and ambiguity exists in which MDT hits are associated with which hits in the trigger system. Lacking more precise information, tracklets are assigned the ϕ coordinate of the MDT chamber's center.

The cut value on $\Delta\alpha$ used for tracklet reconstruction vary by chamber. Tracklets with $|\Delta\alpha| <$ 12 mrad are consistent to within uncertainties with straight-line tracks. When a straight-line track is identified, all of the hits across both layers are refit and kept if the χ^2 probability is better than 5%. The cut $\Delta\alpha_{max}$ = 12 mrad is applied in regions with no magnetic field (BOS and BIS chambers and endcap chambers). Since bending is expected in the other barrel chambers, the cut is looser there. The cut chambers within a magnetic field varies because the different chambers have different spacing between their multilayers. The cut value for $|\Delta b_{max}|$ is set to 3 mm, which is chosen based on a distribution of Δb made after applying $\Delta\alpha$ cuts that shows a signal peak over a flat background. Distributions of Δb are shown in Figure 4.9.

MS Vertex Reconstruction in the Endcaps

Tracklets are reconstructed in the endcaps as straight lines since the MS chambers there are not immersersed in a magnetic field. Consequently, reconsructing vertices in the endcaps is done differently than for the barrel. Decays in the endcaps can be detected just before or within an endcap toroid. For these decays, the charged particles' path are bent in the magnetic field, but their paths are straight beyond the toroid, through the MS detector chambers. Therefore, in the endcaps, tracklets are back-extrapolated as simple straight lines.

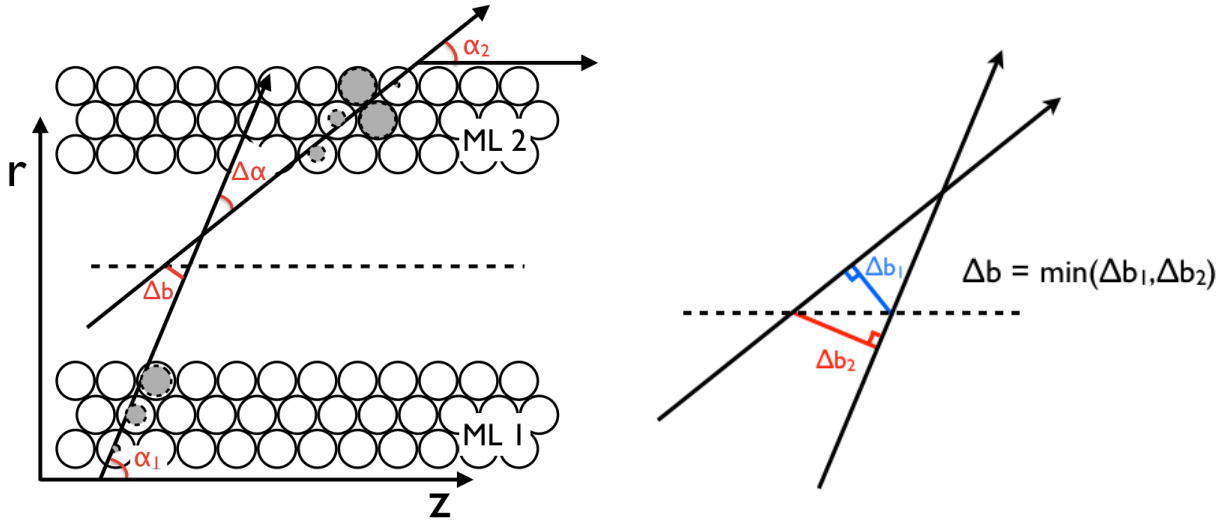

Figure 4.9: Left: Illustration of the bending angle, $\Delta\alpha$, and the closest approach distance Δb. Right: Illustation showing how Δb is the shorter of the two distances of ML segments' closest approach.

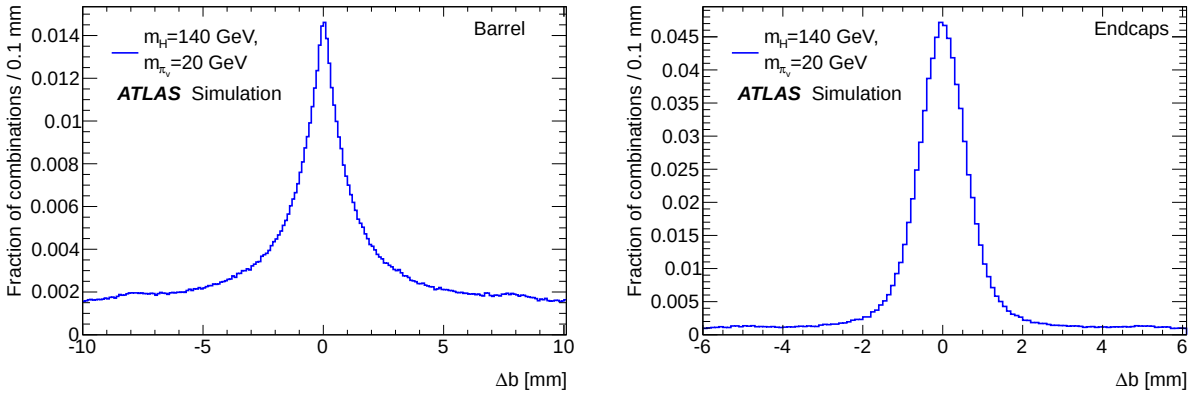

Figure 4.10: Distribution of Δb for segment combinations in the barrel (left) and endcap (right) MS regions for MC signal events at mass point $m_H = 140$ GeV, $m_{\pi_v} = 20$ GeV. For inclusion, the segment combinations are required to pass their chamber's respective cut on $\Delta\alpha$.

These tracklets are arranged into tracklet clusters as is done in the barrel. For each cluster, each tracklet provides a constraining equation of the form $\beta_i = -r\tan\alpha_i + z$, where (r, z) represent the coordinates of the vertex and (β_i, α_i) represent the z-intercept and angle in the (r,z) plane of the ith tracklet. For a collection of tracklets, a preliminary vertex can be found using a least squares regression fit. If the distance of closest approach for all tracklets is less than 30 cm from the vertex, then the preliminary vertex is accepted.

For an analysis done on 2011 data [31] and described in the MS vertex reconstruction publication [29], a simpler version of the endcap vertex reconstruction algorithm was used. This algorithm finds a preliminary vertex using all tracklets in the cluster. If the preliminary vertex were not accepted (because at least one tracklet's impact parameter to the preliminary vertex was greater than 30 cm), then the tracklet with the largest impact parameter would be removed and the regression repeated with the remaining tracklets until a vertex was accepted or fewer than 3 tracklets remained.

For this analysis, this algorithm was changed to increase acceptance while keeping computational cost under control. First, a preliminary vertex is made from every combination of three tracklets in the cluster. For n tracklets in the cluster, there are n-choose-3, or $\frac{n!}{(6*(n-3)!)}$, such combinations to consider. Since a cluster of tracklets is not permitted to contain more than 40 tracklets, the computational time of this operation even in the worst case is tens of seconds. If there are no preliminary 3-tracklet vertices that are accepted, then the algorithm fails to find a vertex in the endcap; otherwise, the algorithm tries to combine additional tracklets with those tracklets that make acceptable 3-tracklet vertices.

The algorithm has two different approaches for adding additional tracklets to an accepted 3-tracklet vertex that has been found. For a tracklet cluster containing 20 or fewer tracklets, the following computation-heavy procedure is used. For each accepted three-tracklet vertex that was found, the algorithm adds one more tracklet to the vertex, recomputes the vertex position, and determines if the vertex is still accepted. The algorithm tries this for each tracklet that's not already associated with the vertex. For each accepted vertex that's had a tracklet added, the procedure is repeated until no tracklets can be added to form an acceptable vertex. The accepted vertex that has the most tracklets associated with it is selected as the vertex found in the tracklet cluster.

This procedure can take tens of minutes since in the worst case it is finding the largest number of tracklets associated with a vertex k out of n total tracklets, with up to n-choose-k $= \frac{n!}{k!*(n-k)!}$ preliminary vertices to be checked for each value of k from 3 up to n (as long as an acceptable preliminary vertex is found for the current iteration of k).

Due to combinatorics, the modified algorithm has a long processing time when many tracklets are present in the cluster. To avoid this long computation, if there are more than 20 tracklets in the cluster, the algorithm from the 2011 data analysis is used. In order to preserve signal acceptance, if the 2011 reconstruction algorithm fails to find a vertex but an acceptable 3-tracklet vertex is present, then the algorithm returns a 3-tracklet vertex that was found.

MS Good Vertex Criteria

The MS vertex reconstruction algorithm was designed with the goal of identifying LLP decay signatures in the MS by studying simulated signal events. In order for these objects to be useful for a search analysis, the algorithm must be optimized against background. To this end, a good vertex criteria (GVC) is defined. Jets that punch through the calorimeter and shower in the MS are a leading source of background, so the GVC is developed to reject punch-through jets. Punch-through jets will have tracks and jets in the same region of the detector as the reconstructed MS vertex, so by requiring track and jet isolation, the ratio of signal to background can be enhanced. Punch-through jets typically have far fewer MS hits than the LLPs searched for in this analysis, so cuts on the number of MS hits is an additional handle for rejecting background while preserving signal.

The algorithm is optimized against the background of MC dijet events. Background events are taken from MC dijet samples with dijet events generated across a broad range of jet truth p_{T}. Event selection consists of requiring a good collision at the IP (at least 3 tracks with $p_{\mathrm{T}} > 1$ GeV) and two leading jets to be approximately back-to-back ($\mid \Delta\phi \mid > 2.14$) in events that pass a single-jet trigger with jet $E_{\mathrm{T}} > 360$ GeV. When looking at MC signal, the jet trigger and back-to-back jet requirements are not applied because neither are necessary in signal LLP events.

The metric $S/\sqrt{B}$ is used to optimize the cut selection, where S and B are the fraction of signal

and background events that survive after imposing a particular cut. In many cases, the final cut is chosen where $S/\sqrt{B}$ begins to stabilize, rather than reach a maximum.

Dijet events that contain vertices, unlike events with LLP decays, should have tracks and jets that connect the vertex to the IP. Consequently, cuts are applied on how near a jet or ID track may be to an MS vertex. No ID tracks with $p_{\mathrm{T}} > 5$ GeV may be within $\Delta R < 0.3(0.6)$ of a MS vertex in the barrel (endcaps). Additionally, the sum of all ID tracks' p_{T} must be less than 10 GeV within $\Delta R < 0.2$ of a barrel or endcap MS vertex. In the calorimeter, no jets with $E_{\mathrm{T}} > 30$ GeV with $\log_{10}(E_{\mathrm{HAD}}/E_{\mathrm{EM}}) < 0.5$ may be within $\Delta R < 0.3(0.6)$ of a MS vertex in the barrel (endcaps).

Cuts are applied on the number of MDT and RPC/TGC hits in the MS. An MS vertex originating from a displaced decay typically has many more hits than an MS vertex from a jet that punches through the calorimeter, so a minimum of 300 MDT hits and 250 RPC/TGC hits are required within $\Delta R < 0.7$ of the MS vertex. A maximum number of 3000 MDT hits is also applied to remove events caused by coherent noise bursts in the MDT chambers. The requirements on MDT hits and RPC/TGC hits are both applied since a noise burst in the MDT system is not expected in coincidence with one in a trigger system.

The MS GVC cuts are summarized in Table 4.1. The number of MDT hits in a cone around a displaced decay in the MS barrel is shown in Figure 4.12. The affect of cuts on RPC and TGC hits are shown in Figures 4.13 and 4.14. The affect of isolation cuts on tracks and jets is shown in Figures 4.15-4.20. In total, the MS GVC preserves 60-70% of MS vertices in the scalar boson MC sample and reduces background from multijet events to a negligible level. The effect on total signal selection is shown in Figure 4.11.

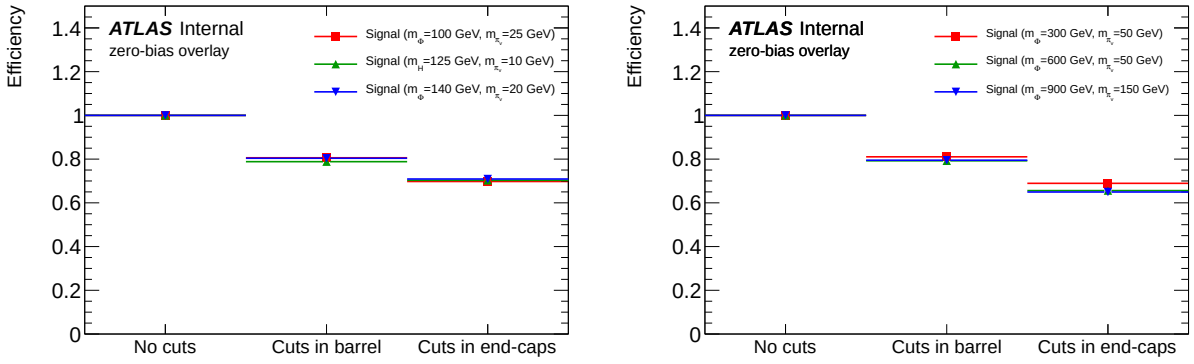

(a) (b)

Figure 4.11: Effect on the signal efficiency after applying all the cuts for good MS vertices for low-mass scalar boson samples (left) and high-mass scalar boson samples (right).

MS Vertex Performance

The performance of the MS Vertex routine is studied by finding the difference in position between the known decay location and the reconstructed vertex position.

Figure 4.21 shows that the reconstructed θ of the π_v line of flight is within 12 mrad of the MC true value and that the reconstruction in ϕ is within 50 mrad, which corresponds to $\sim$1/8 of an MDT chamber extent in ϕ. The decay vertex position (Figure 4.22) is reconstructed with a resolution of 20 cm in z and 32 cm in r.

Figure 4.23 shows the position resolution of the reconstructed vertices in the MS endcaps. Because the tracklets are measured outside the magnetic field region and do not have momentum or charge measurements, the position of the vertex is systematically shifted towards smaller values of r_{reco} and the resolution is degraded with respect to the vertices found in the barrel region.

Locations of MS vertex reconstruction were studied on data that passes the RoI Cluster trigger. Figure 4.24 shows the location of reconstructed vertices in the detector. Figure 4.25 shows the projection in η and the barrel and endcap projections in ϕ. A slight asymmetry is present with more MS vertices reconstructed in $\eta < 0$. This behavior originates from the Muon RoI Cluster

Description	Barrel Cut	Endcap Cut
Number of MDT hits	$300 \leq \text{nMDT} < 3000$	$300 \leq \text{nMDT} < 3000$
Number of RPC/TGC hits	$\text{nRPC} \geq 250$	$\text{nTGC} \geq 250$
High p_{T} track isolation	$\Delta R < 0.3$	$\Delta R < 0.6$
Σp_{T} for nearby tracks	$\Sigma p_{\text{T}} < 10$ GeV	$\Sigma p_{\text{T}} < 10$ GeV
Jet isolation within	$\Delta R < 0.3$	$\Delta R < 0.6$

Table 4.1: Summary of good MS vertex criteria requirements in barrel and endcap regions.

trigger's bias for selecting clusters in $\eta < 0$.

4.2 Decays in the Inner Detector

4.2.1 ID Vertex Reconstruction

Standard ATLAS tracking in the ID is done to identify charged tracks originating from near the IP. Standard ATLAS tracking is done in two stages. The first stage uses "inside-out" track reconstruction to find tracks in the silicon region of the ID, and then the tracks are extended to find matching hits in the TRT. The second stage uses "outside-in" track reconstruction to find segments in the TRT that are interpolated to the IP and match with silicon hits. Since tracks are assumed to originate at the IP, cuts are placed on the impact parameters and hit requirements that limit the number of possible hypothesis tracks. These restrictions help to keep processing time low since they limit the number of hypothesis tracks that are computed.

Displaced decays in the ID will result in tracks that originate from the LLP's decay position. In general, such tracks do not have small impact parameters with respect to the IP. To reconstruct such tracks, a technique called "secondary track reconstruction" is employed. Secondary track reconstruction attempts to reconstruct tracks from those ID hits that were not found associated with tracks in standard ATLAS tracking. Only inside-out track reconstruction is used in secondary track reconstruction. By restricting reconstruction to the unassociated hits and only using inside-out

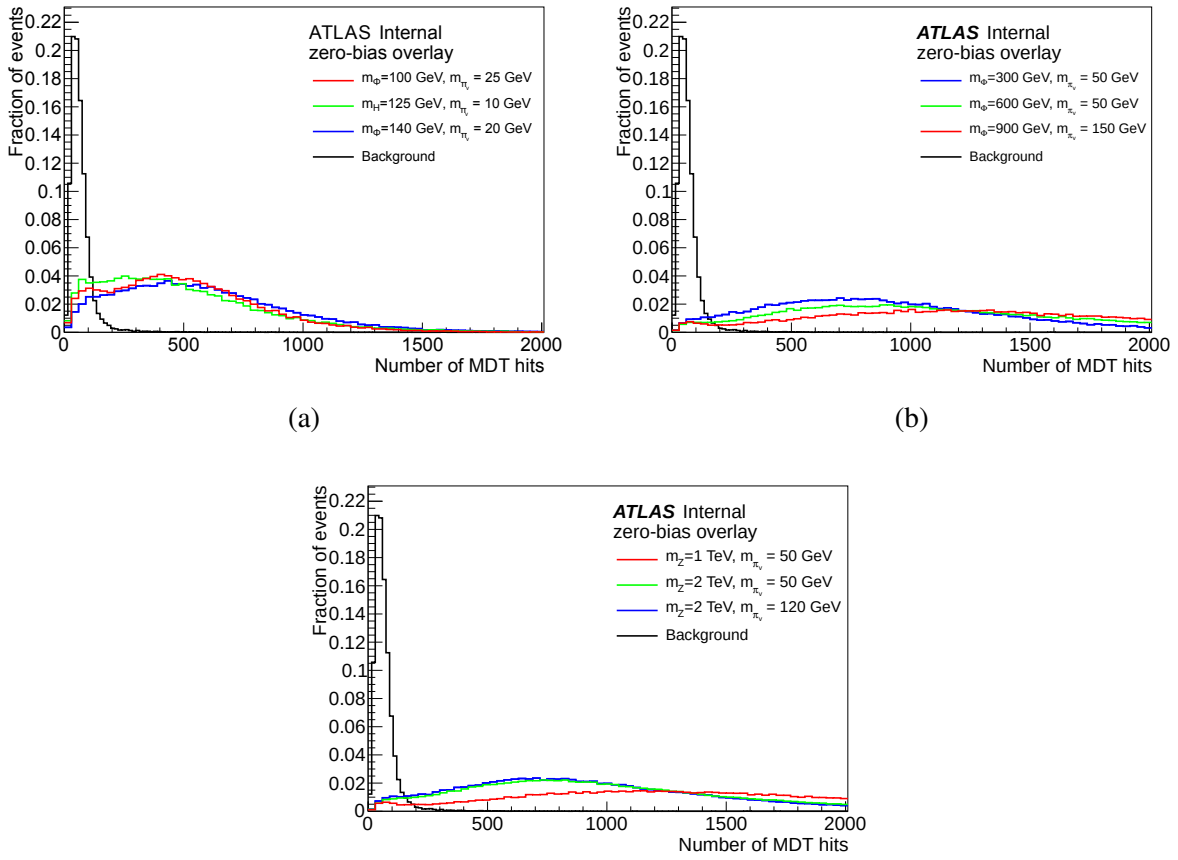

Figure 4.12: The number of MDT hits in a cone of $\Delta R < 0.6$ around a displaced decay or punch-through jet in the barrel. The signals are (a) Scalar boson, (b) high mass Scalar boson, and (c) Z' benchmark samples. The background is MC di-jet events. The chosen value for the minimum number of MDT hits in the barrel is ≥ 300.

tracking, secondary track reconstruction can tolerate hypothesis tracks with looser cuts without being too computationally intensive. The impact parameter and hit requirements for standard ATLAS and secondary track reconstruction are listed in Table 4.2. A comparison of impact parameters of standard ATLAS tracking and the secondary tracking is shown in Figure 4.26.

A displaced ID vertex reconstruction tool was developed to identify LLPs decaying in the ID.

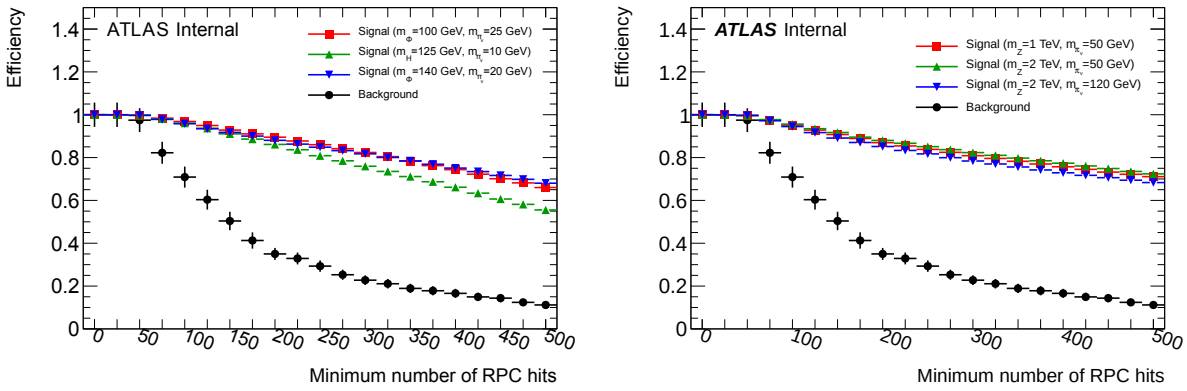

(a) (b)

Figure 4.13: MS vertex reconstruction efficiency in the barrel as a function of the minimum number of RPC hits for various signals. The signals are (a) Scalar boson and (b) Z' benchmark samples. The background is MC di-jet events. The chosen value for the minimum number of RPC hits is ≥ 250. Because of these distributions and to improve performance, an internal cut of nRPC ≥ 200 was added to the MS vertex reconstruction algorithm in the barrel.

The reconstruciton algorithm is derived from the ATLAS primary vertex reconstruction algorithm. It finds a group of secondary tracks that can be fit to a point, with the point identified as the location of the secondary, displaced ID vertex (ID vertex).

Unlike primary vertices, ID vertices are not found within the beam spot. Consequently, ID vertices are reconstructed with loosened cuts compared to primary vertices. An additional track transverse impact parameter cut requiring $d_0 > 10$ mm was added to remove any tracks that come from the IP. The cuts on tracks used for primary vertex reconstruction and displaced ID vertex reconstruction are summarized in Table 4.3.

ID Good Vertex Criteria

ID vertices were created with the goal of identifying LLP decays. Any source of ID vertices

Parameter	Standard value	Secondary value
maximum d_0	10 mm	500 mm
maximum z_0	320 mm	1000 mm
minimum number of silicon hits	6	2
maximum number of shared hits	1	2

Table 4.2: Track finding selection cuts on standard ATLAS track reconstruction and secondary track reconstruction.

	Primary	Secondary
min d_0	-	10 mm
$d_0/\sigma(d_0)$	5	removed
$z_0/\sigma(z_0)$	10	removed
min Si hits	6	4
min Pixel hits	1	0
min SCT hits	4	2
χ^2	3.5	5

Table 4.3: Selection cuts on tracks used for primary vertex reconstruction and ID vertex reconstruction.

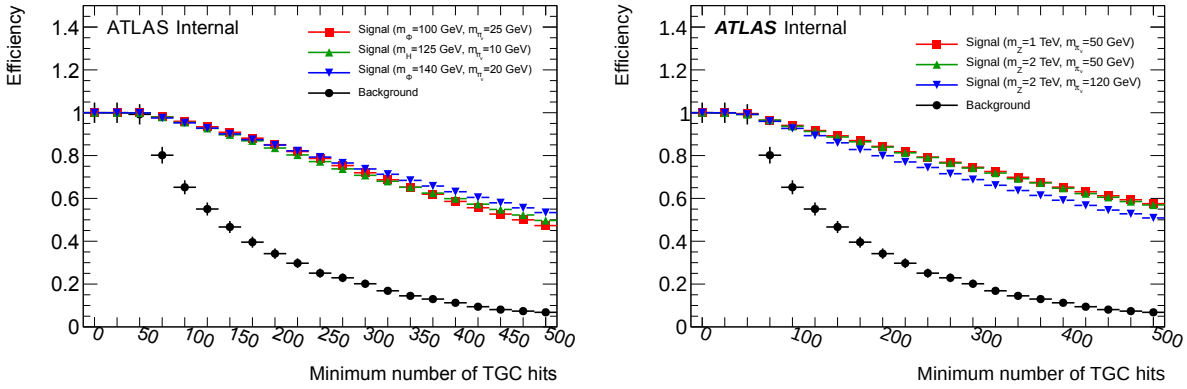

(a) (b)

Figure 4.14: MS vertex reconstruction efficiency in the endcaps as a function of the minimum number of TGC hits for various signals. The signals are (a) Scalar boson and (b) Z' benchmark samples. The background is MC di-jet events. The chosen value for the minimum number of TGC hits in the endcaps is ≥ 250. As a consequence of these distributions, an internal cut of nTGC $\geq$ 200 was added to the MS vertex reconstruction algorithm in the endcaps.

that isn't due to a neutral LLP decay is a source of background, and an ID vertex from a background source is considered a fake ID vertex. An ID GVC is defined that preferentially removes background vertices and preserves vertices reconstructed from signal LLP decays. Consequently, the ID GVC improves significance of ID vertex observation.

The primary background for the ID GVC comes from hadrons created at the IP that interact with detector material in the pixel and SCT detectors. This source of background is removed by vetoing ID vertices that overlap known ID material. The material veto uses an algorithm that calculates the distance between an ID vertex and the closest known detector material. Two separate material models are used for the ID. In the pixel layers, the location of each pixel module is known, and each pixel module has a defined 3-D material shape. In the pixel support structure and SCT layers, a material map is used that was originally developed for a SUSY R-parity violating search [32]. The material map was determined from studies of hadronic interactions in data following methods

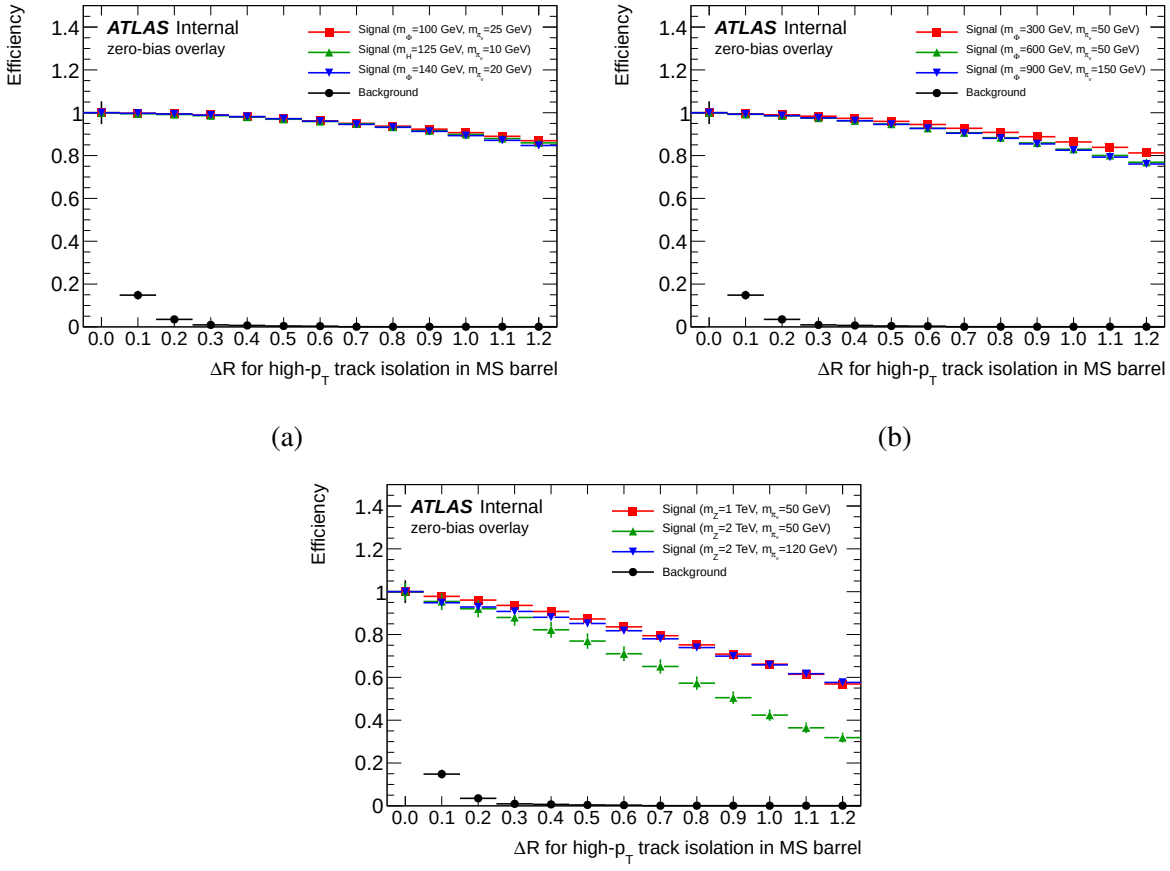

Figure 4.15: MS vertex reconstruction efficiency in the barrel as a function of ΔR for the high-p_{T} track isolation requirement for various signals. The signals are (a) Scalar boson, (b) high mass Scalar boson, and (c) Z' benchmark samples. The background is MC di-jet events. The chosen value for the high-p_{T} track isolation requirement in the barrel is $\Delta\mathrm{R} < 0.3$.

described in [33]. The endcap material map was constructed using data collected in 2010, and the barrel uses an updated map constrcuted using 2012 data. With the position of the ID vertex and the nearest material known, a variable d/σ is calculated where d is the distance from the vertex to nearest material layer and σ is the vertex position uncertainty along the direction of the material. Vertices are vetoed when $d/\sigma < 6$.

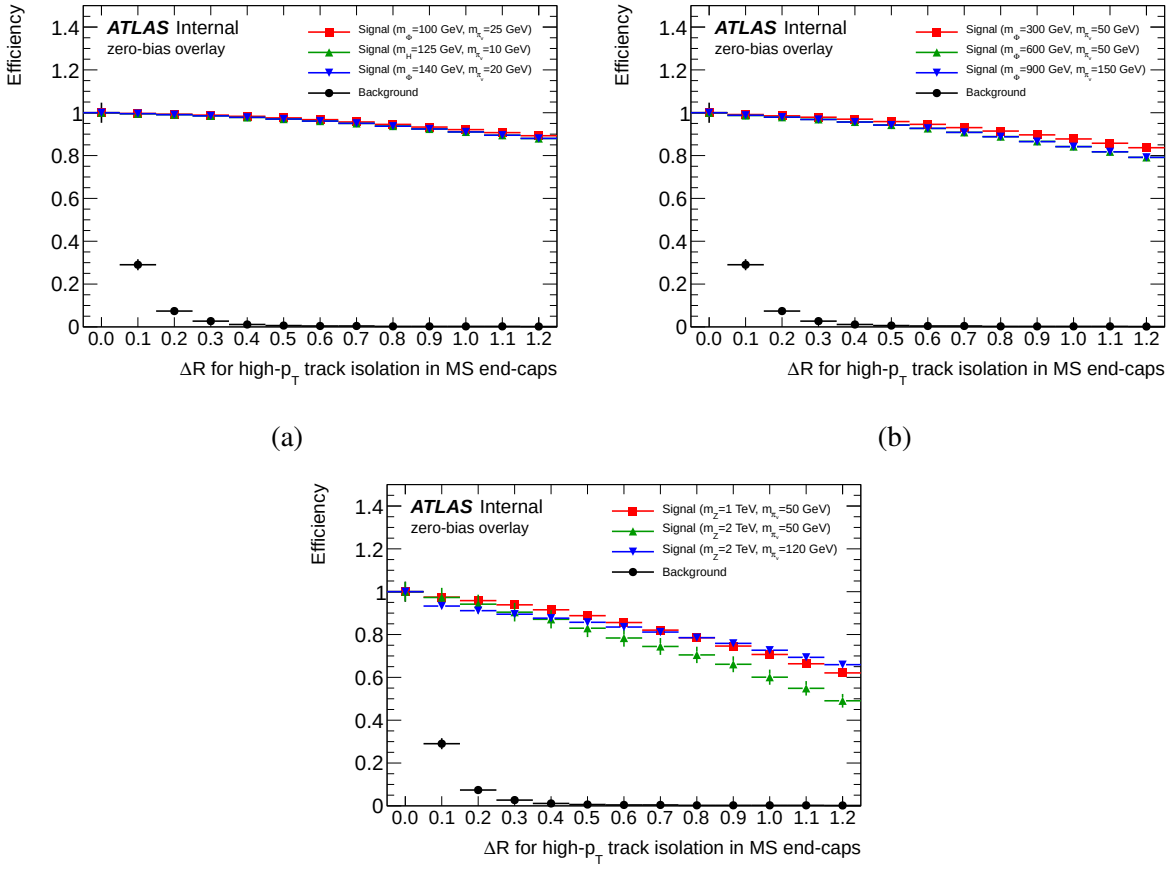

Figure 4.16: MS vertex reconstruction efficiency in the endcaps as a function of ΔR for the high-p_{T} track isolation requirement for various signals. The signals are (a) Scalar boson, (b) high mass Scalar boson, and (c) Z' benchmark samples. The background is MC di-jet events. The chosen value for the high-p_{T} track isolation requirement in the endcaps is $\Delta\mathrm{R} < 0.6$.

The ID GVC is further optimized by requiring a jet to be reconstructed within a ΔR cut of the ID vertex and the vertex to have a minimum number of tracks. Both cuts were optimized by comparing MC signal to multijet data events. For optimizing signal with the scalar boson sample, the multijet events were selected by requiring a good collision IP (> 3 tracks with $p_{\mathrm{T}} > 1$ GeV), $E_{\mathrm{T}}^{\mathrm{miss}} < 75$ GeV, and passing the EF_j220_a4tchad trigger. On average, background vertices have

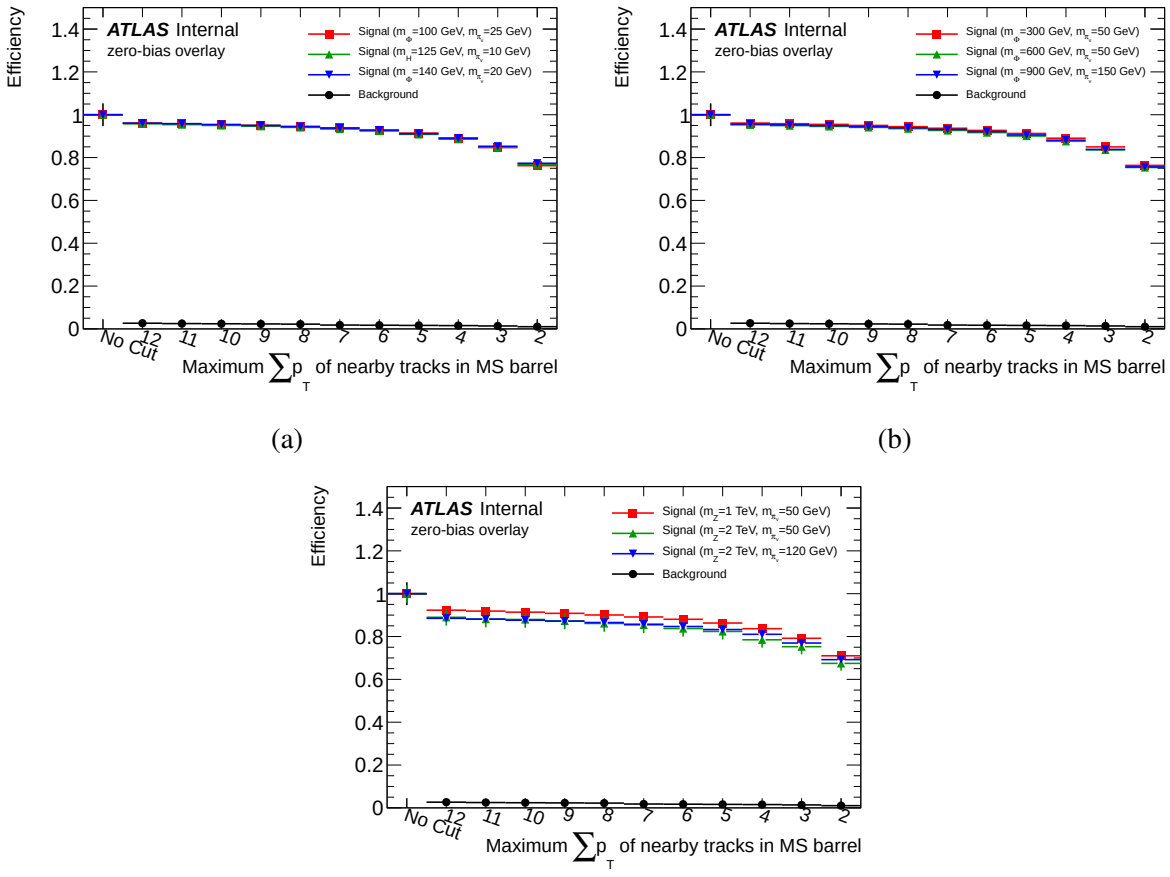

Figure 4.17: MS vertex reconstruction efficiency in the barrel as a function of the maximum $\sum p_{\mathrm{T}}$ of nearby tracks for various signals. The signals are (a) Scalar boson, (b) high mass Scalar boson, and (c) Z' benchmark samples. The background is MC di-jet events. The chosen value for the maximum $\sum p_{\mathrm{T}}$ of nearby tracks in the barrel is $\sum p_{\mathrm{T}} < 10$ GeV.

a lower track multiplicity than signal vertices, so a cut requiring vertices to have at least 5 tracks was used. Background ID vertices can be caused by interactions of low-energy particles that don't result reconstructed jets. A cut was defined, requiring a jet with $p_{\mathrm{T}} > 20$ GeV, $|\eta| < 4.5$, and $\Delta R_{IDVx,jet} < 0.4$. A summary of the ID GVC is presented in Table 4.4.

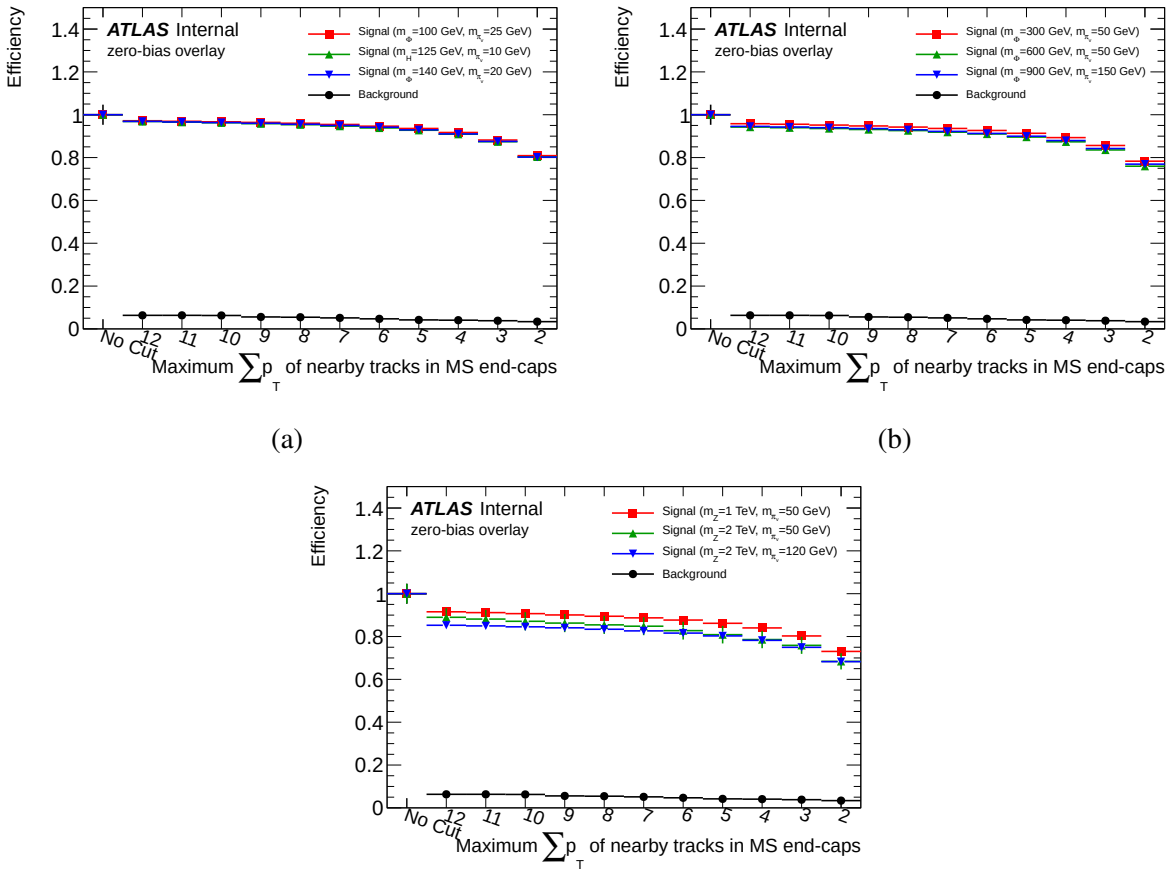

Figure 4.18: MS vertex reconstruction efficiency in the endcaps as a function of the maximum $\sum p_{\mathrm{T}}$ of nearby tracks for various signals. The signals are (a) Scalar boson, (b) high mass Scalar boson, and (c) Z' benchmark samples. The background is MC di-jet events. The chosen value for the maximum $\sum p_{\mathrm{T}}$ of nearby tracks in the endcaps is $\sum p_{\mathrm{T}} < 10$ GeV.

4.3 Efficiency of Identifying Displaced Decays

The efficiency of MS vertex reconstruction is determined in the simulated Scalar boson samples. Since MS vertices are reconstructed from tracklets in a limited region of significant MS activity and the LLP are typically well separated in the scalar boson sample, efficiency is shown on a per-LLP

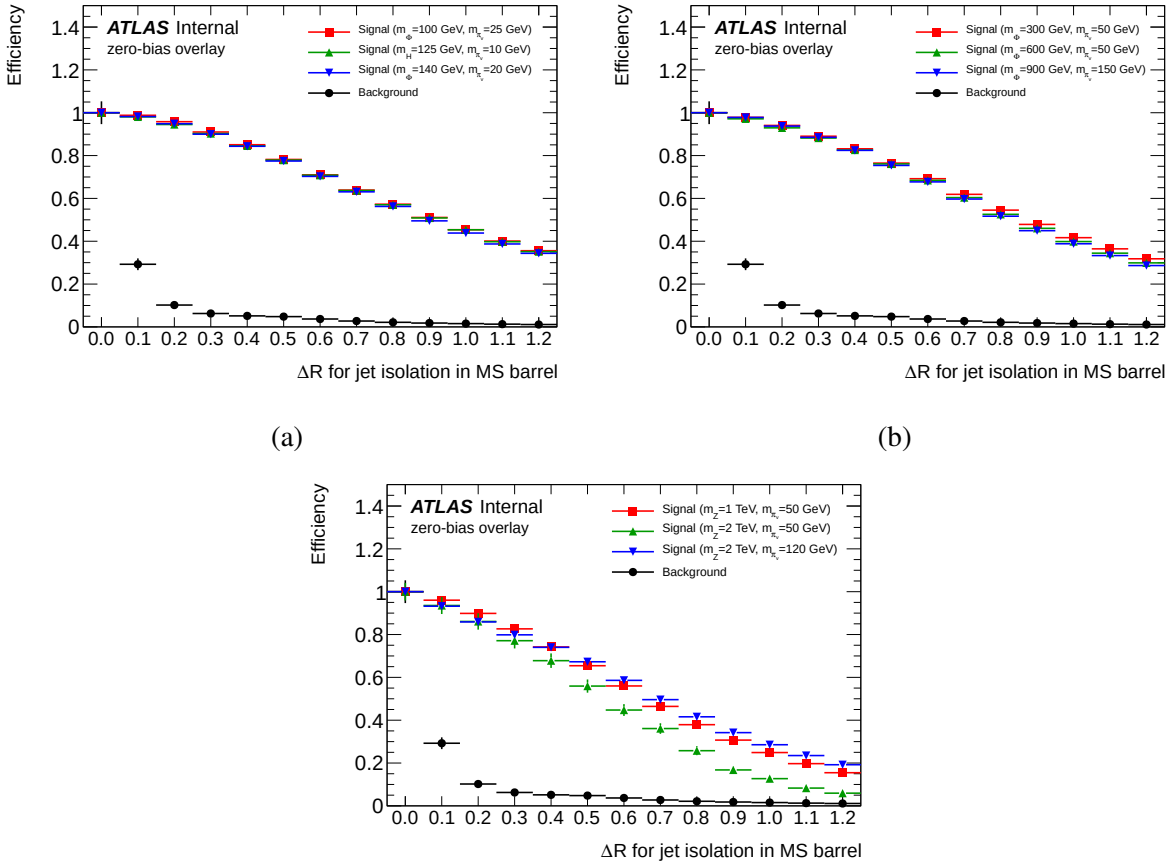

Figure 4.19: MS vertex reconstruction efficiency in the barrel as a function of ΔR for the jet isolation requirement for various signals. The signals are (a) Scalar boson, (b) high mass Scalar boson, and (c) Z' benchmark samples. The background is MC di-jet events. The chosen value for the jet isolation in the barrel is $\Delta R < 0.3$.

basis. The efficiency is defined as the fraction of LLPs decaying in a position bin that have a good MS vertex within a cone of ΔR = 0.4 of the LLP decay position. The efficiency of reconstructing MS vertices in the barrel and endcaps is shown in Figure 4.27.

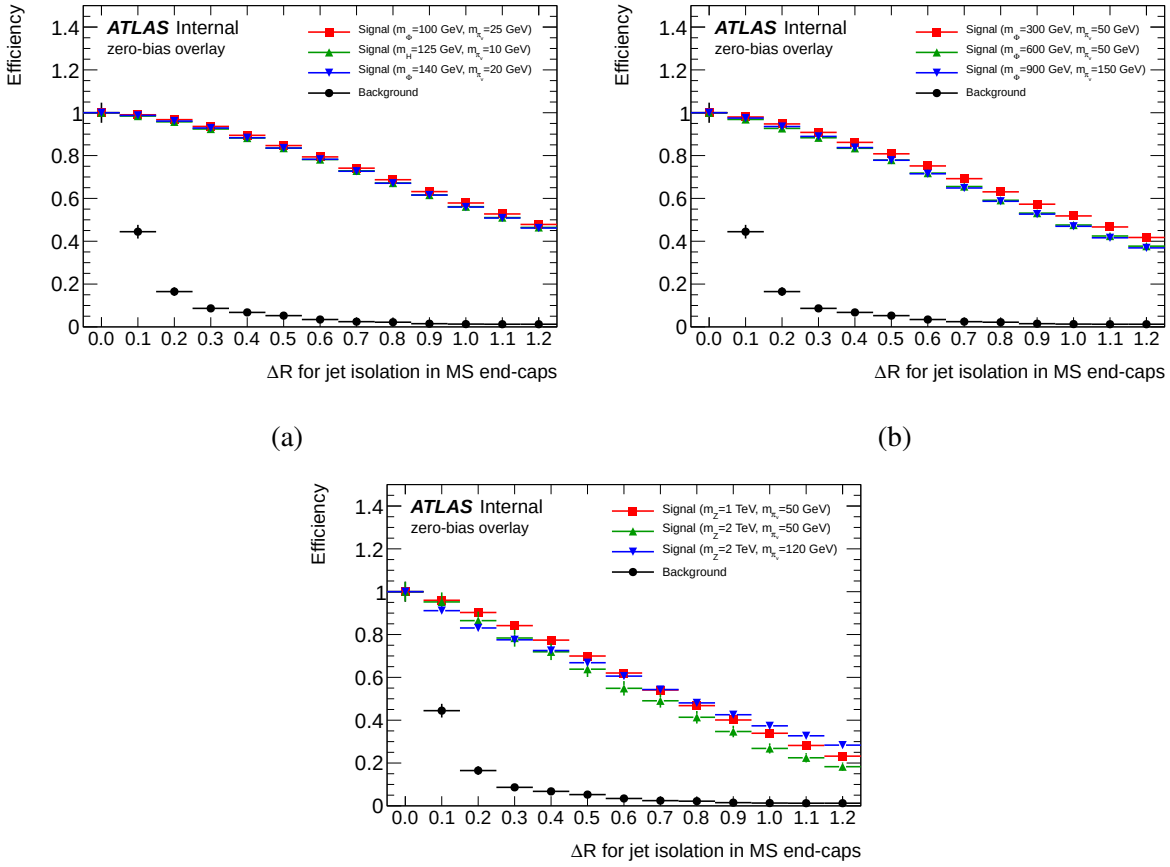

Figure 4.20: MS vertex reconstruction efficiency in the endcaps as a function of ΔR for the jet isolation requirement for various signals. The signals are (a) Scalar boson, (b) high mass Scalar boson, and (c) Z' benchmark samples. The background is MC di-jet events. The chosen value for the jet isolation in the endcaps is $\Delta R < 0.6$.

4.4 Systematic Uncertainties of Signal Selection

4.4.1 Systematic Uncertainty of the Muon RoI Cluster Trigger

To evaluate the systematic uncertainty of the Muon RoI Cluster trigger, a data-driven approach is employed that compares the properties of punch-through jets from data to those from MC. The

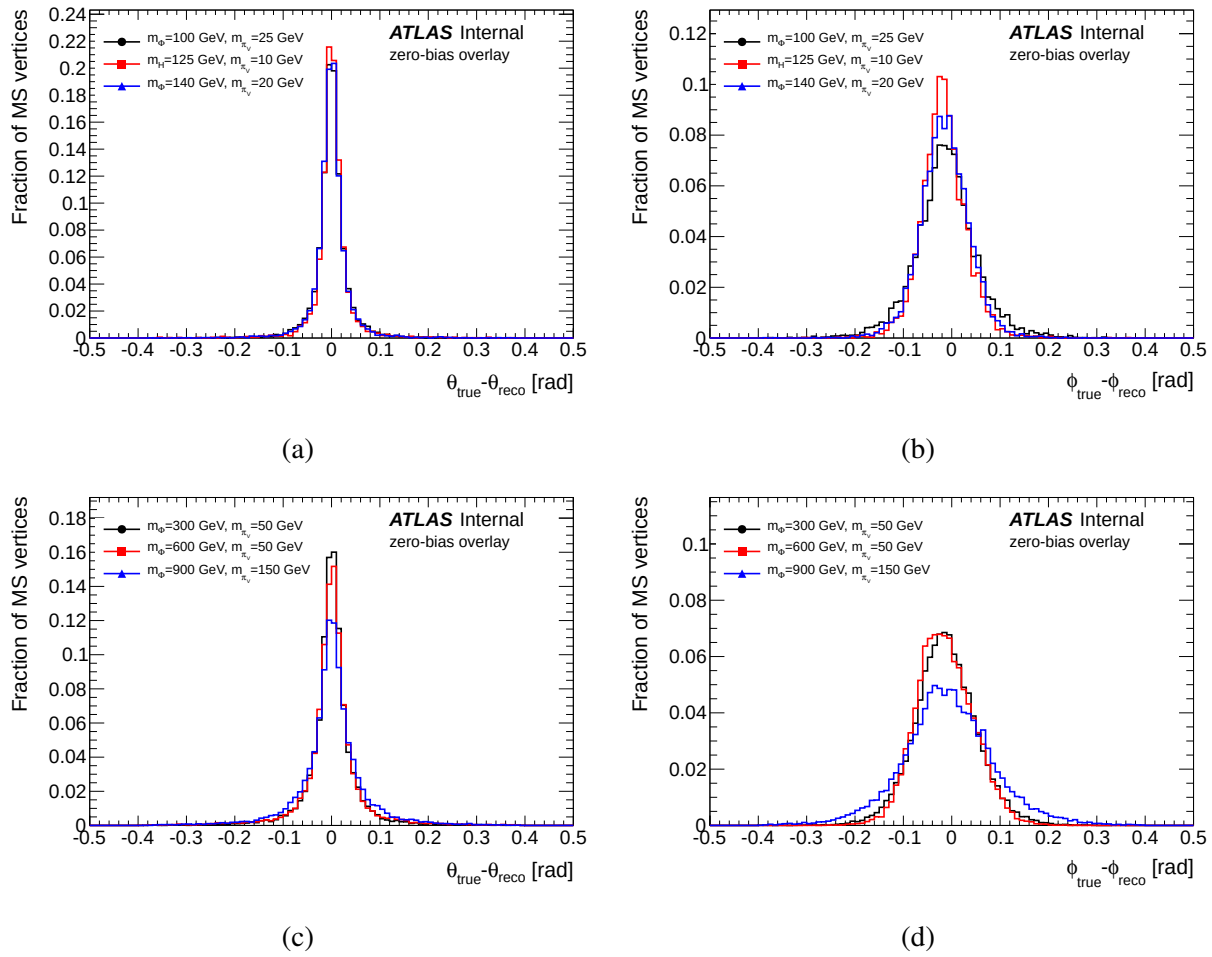

Figure 4.21: Angular difference between the long-lived particle true line of flight and reconstructed line of flight. Differences for π_v are shown for θ (left) and ϕ (right).

punch-through jet sample is similar to signal events as it contains both low energy photons and charged hadrons in a localized region of the MS. Because the trigger has a different requirement on the number of RoIs in the barrel and endcaps, separate systematic uncertainties, using the same procedure, are determined.

Each punch-through jet with at least 300 MDT hits within a cone of $\Delta R < 0.6$ from the jet axis is selected, and the number of RoIs within this cone ($\Delta R < 0.6$) is compared to MC samples. A distribution of the number of muon RoIs is shown in Figure 4.28. The corresponding ratio of data

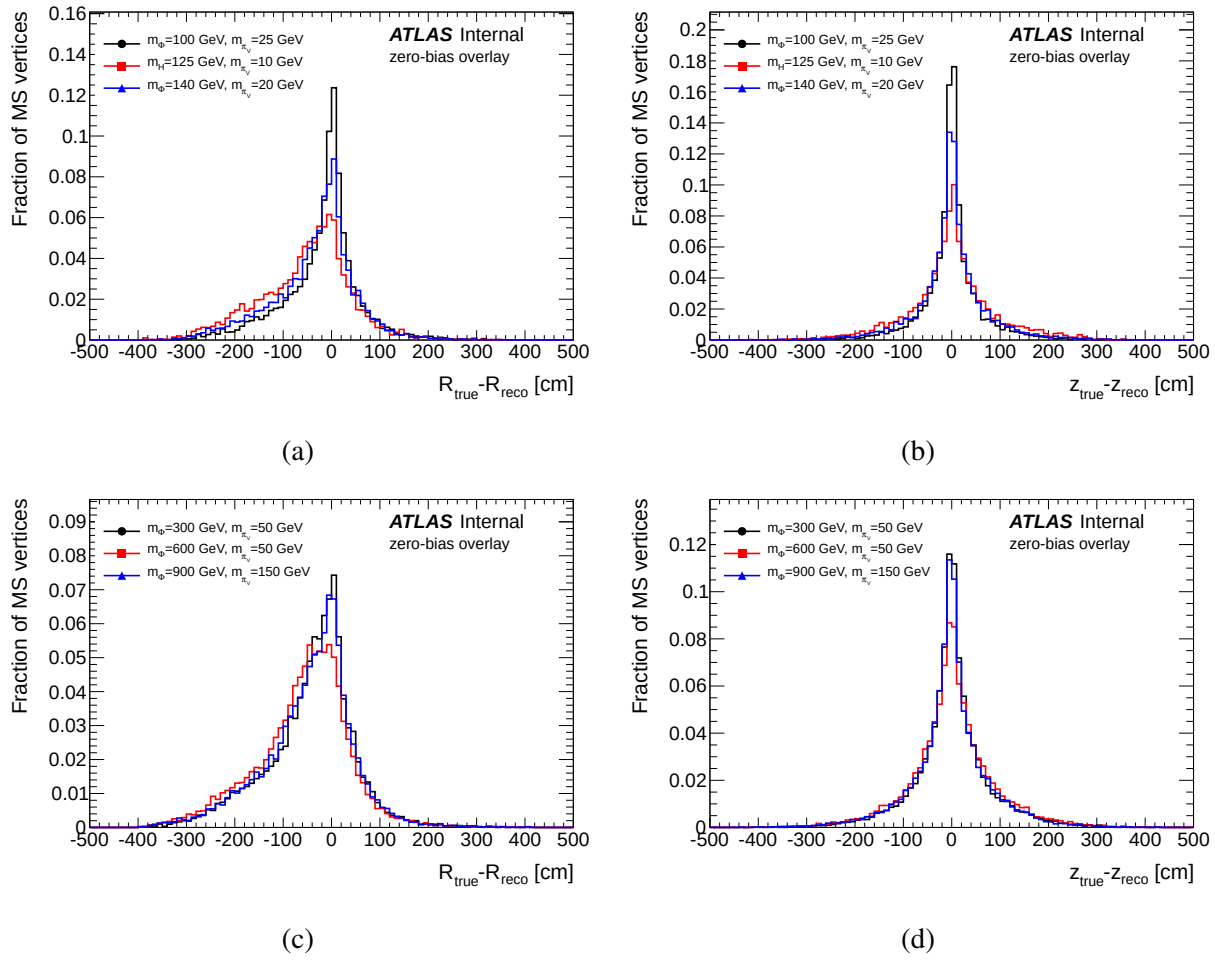

Figure 4.22: Difference between the R coordinate (left) and z coordinate (right) of the reconstructed vertex and the true decay position for decays in the MS barrel for various benchmark samples.

to MC is shown in Figure 4.29. The weighted average of the ratio of data to MC gives a value of 0.91 ± 0.06 in the barrel and 0.99 ± 0.06 in the endcaps. The barrel value differs from 1 by larger than one sigma, so the 9% deviation is taken as the systematic uncertainty. The endcaps value is consistent, within one sigma, to a scale factor of 1, and the 6% statistical uncertainty is taken as the systematic uncertainty.

To understand the effects of the JES uncertainty on the isolation requirement, each jet is increased by its JES uncertainty. The JES uncertainty estimate for each jet is given by the Mul-

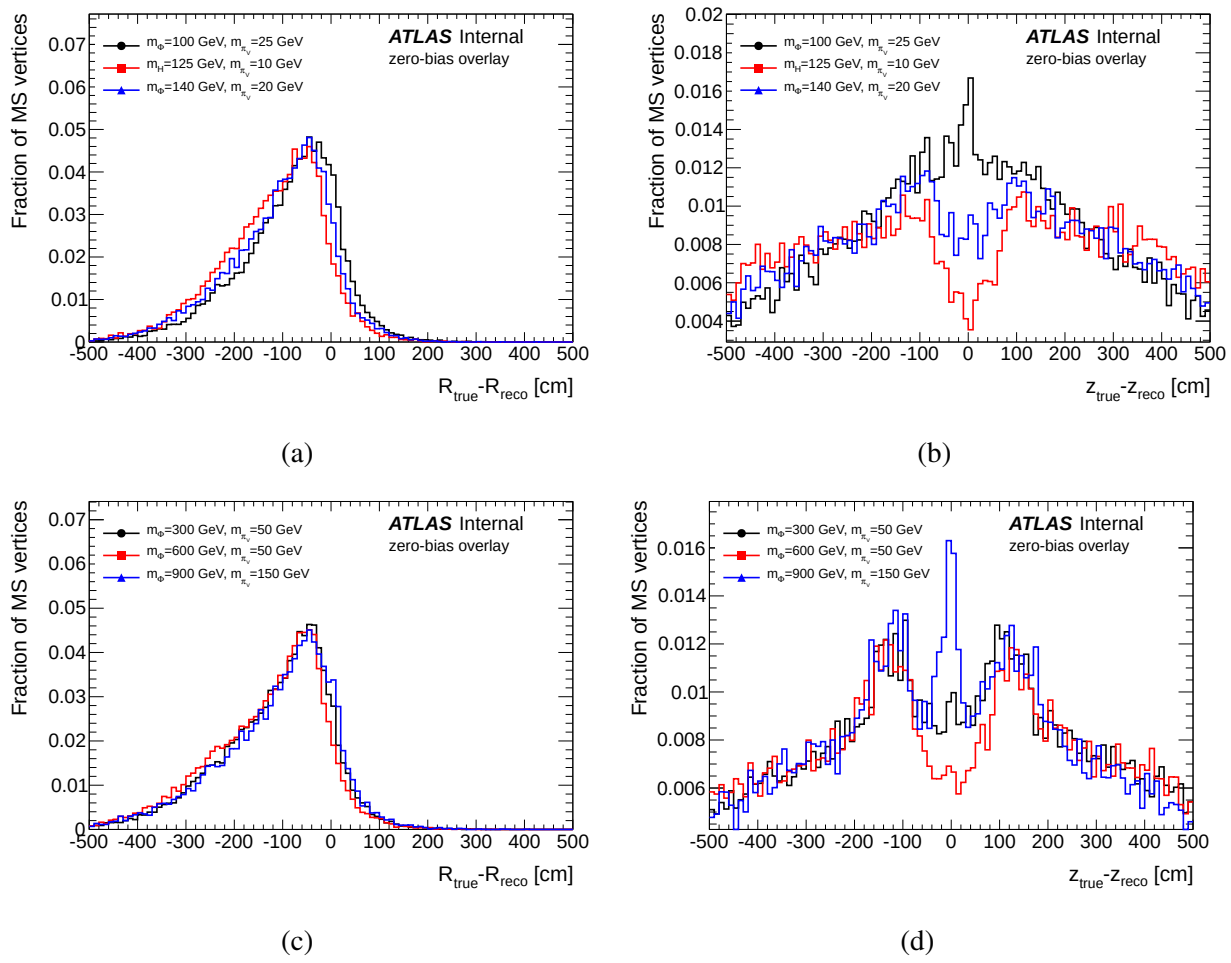

Figure 4.23: Difference between the R coordinate (left) and z coordinate (right) of the reconstructed vertex and the true decay position for decays in the MS endcaps for various benchmark samples.

tijetJESUncertaintyProvider. The resulting change in trigger efficiency is less than 0.1% for the Scalar boson signal MC samples. The pileup effects have been studied by disabling the pileup reweighting tool and comparing the unweighted to reweighted samples. This procedure gave a trigger efficiency systematic uncertainty of less than 0.3% for each of the Scalar boson signal MC samples. Increasing the energy of all jets by 5% to account for ISR uncertainties [34] results in a 0.1% change of the trigger acceptance rate. The small effects of these uncertainties are due to the relatively few number of jets from ISR or pileup with energy near or above the isolation cut. The

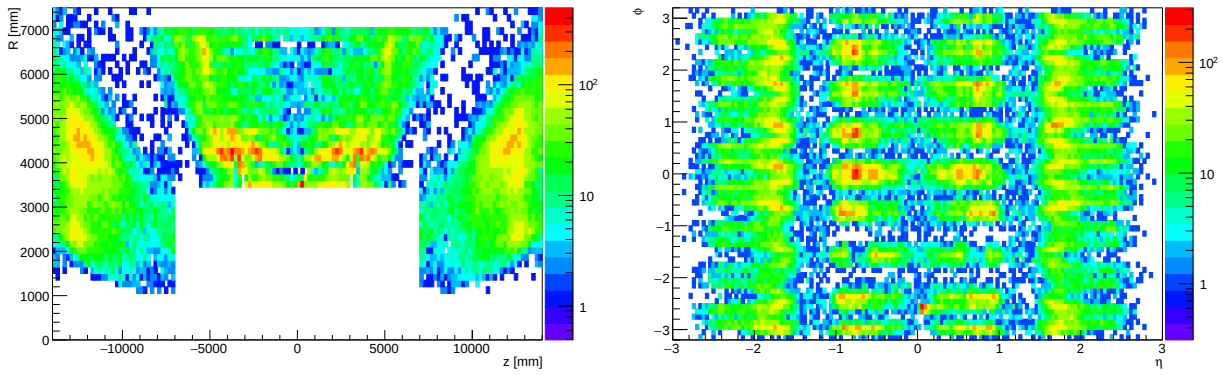

(a) (b)

Figure 4.24: Location of good MS vertices reconstructed from data passing the RoI Cluster trigger in (R, Z) (left) and (η, ϕ) (right).

	d/σ from material	ΔR(vtx,jet)	nTracks
Scalar boson	≥ 6	< 0.4	≥ 5

Table 4.4: Good vertex criteria for vertices reconstructed in the ID.

dominant uncertainty in the trigger algorithm is the MC-data comparison discussed above.

As a consequence of a mismodelling in the MC simulation of the RPC barrel timing response, slow particles ($\beta < 1$) can arrive inside the RPC's MC timing window but outside of the actual window in data, resulting in artificially higher efficiencies in the simulated samples. To correct for this effect, a scale factor is applied to events that pass the trigger. This scale factor is found to have an uncertainty of 0.4% and applies only to decays that occur in the barrel.

The total systematic uncertainty of the Muon RoI Cluster trigger is found by adding in quadrature the contributions to systematic uncertainty from JES, ISR, pileup, RPC timing scaling and number of muon RoIs. The results are summarized in Table 4.5.

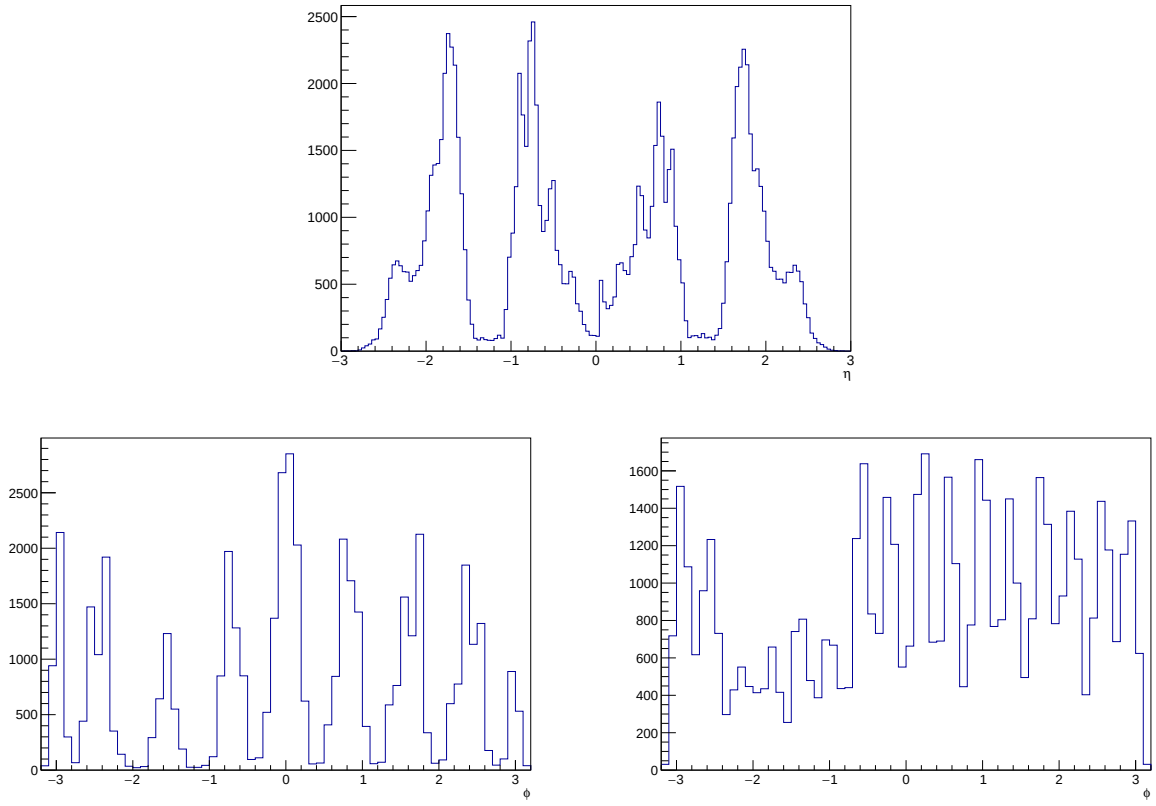

Figure 4.25: Location of good MS vertices reconstructed from data passing the RoI Cluster trigger. The top figure shows the location of all vertices in the η projection. The bottom figures show the location of vertices in in the barrel (left) and endcaps (right) in the ϕ projection.

4.4.2 Systematic Uncertainty of ID Vertex Reconstruction

The efficiency for reconstructing LLP decay vertices in the ID is calculated using signal MC. A dijet control sample is used to understand possible differences in secondary track reconstruction and ID vertex reconstruction efficiencies between MC and data. Dijet events in data were selected from the first 13 fb^{-1} of data collected in 2012. Dijet events in MC were selected from MC12 JZ2W-JZ6W samples. To compare the reconstruction of LLP decays in data and MC, events with K_S^0 decays are found. In both data and MC, a primary vertex with four or more tracks and a dijet

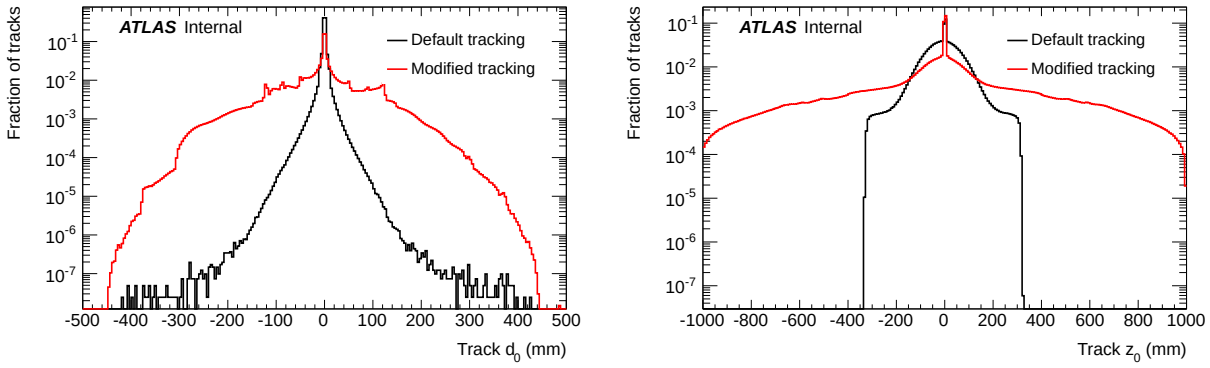

(a) (b)

Figure 4.26: Transverse (left) and longitudinal (right) impact parameter distributions for tracks reconstructed with default and loosened requirements for a LLP MC benchmark sample.

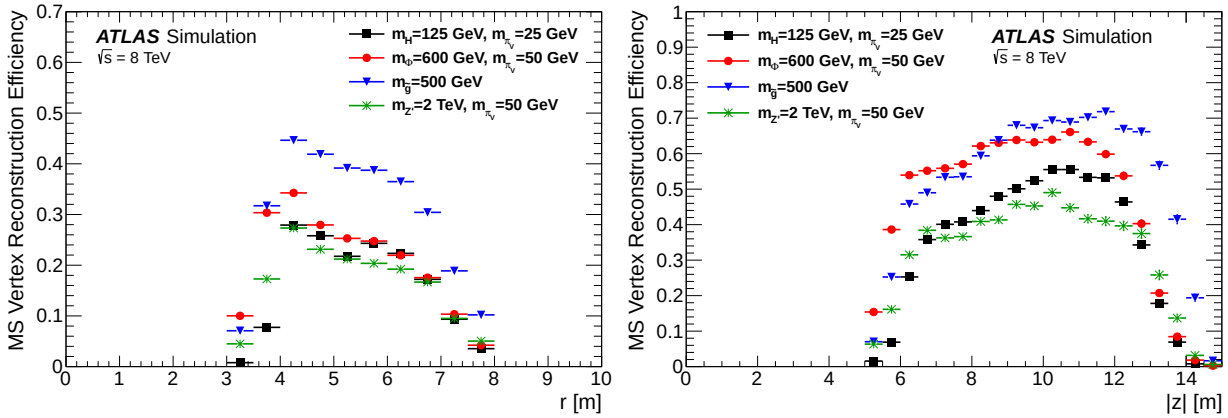

Figure 4.27: Efficiency of MS vertex reconstruction as a function of LLP decay position in the barrel (left figure, in radial distance) and endcaps (right figure, in $|z|$ position).

requirement of two good jets with an opening angle of $|\Delta\phi| > 2.14$ are required. The different JZXW samples are generated for different ranges of the leading jet p_{T} distribution and statistically weighted as described in section 3.2. Figure 4.30 shows the momentum, P, distribution for K_S^0 reconstructed in data and each of the JZXW samples. The shape of the momentum distribution is

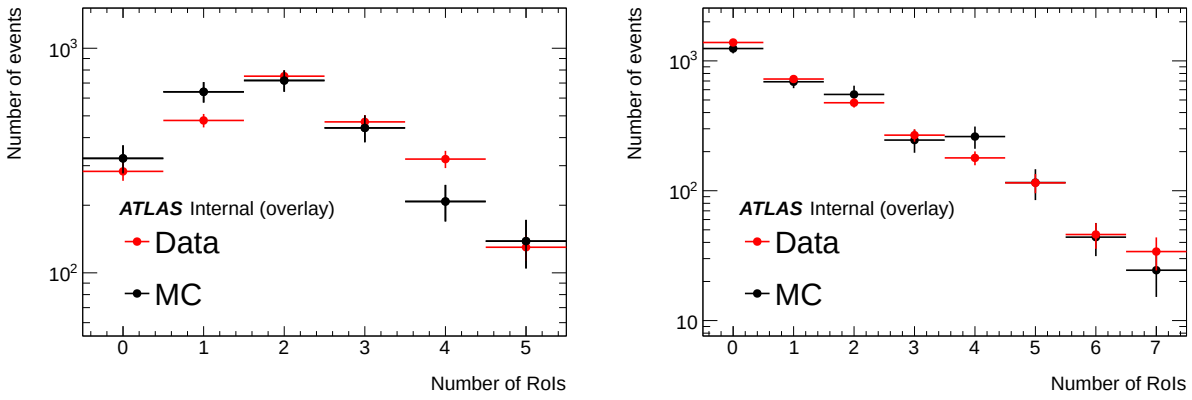

(a) (b)

Figure 4.28: Distribution of the number of muon RoIs found in punch-through jets for (a) the barrel ($|\eta| < 1.0$) and (b) endcaps ($|\eta| > 1.0$).

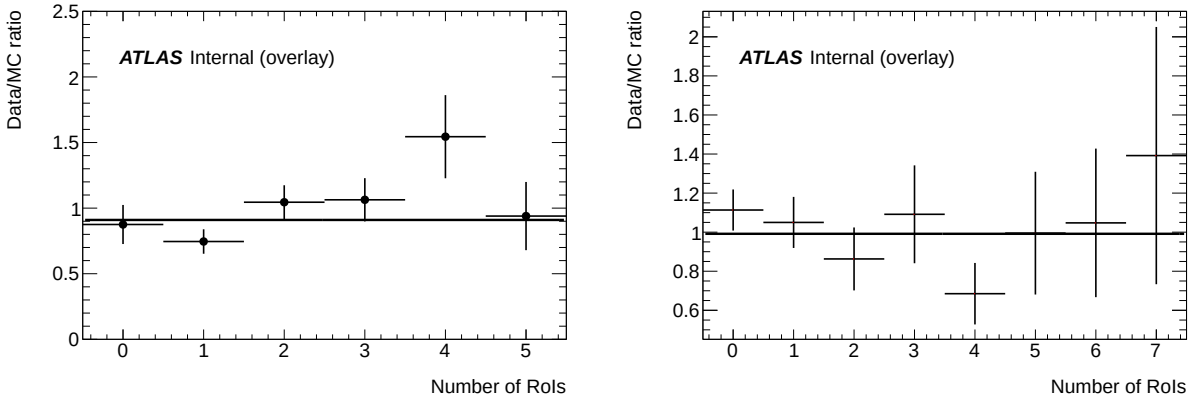

(a) (b)

Figure 4.29: Ratio of data/MC of the number of muon RoIs found within a cone of $\Delta R < 0.6$ of punch-through jets' axes for (a) the barrel ($|\eta| < 1.0$) and (b) endcaps ($|\eta| > 1.0$). The weighted average (red line) gives the data-MC scale factor.

similar up to 20 GeV for all the JZXW MC samples; in order to maximize the statistic significance from MC, the K^0_S distributions are added together without their MC scale factor applied.

Source	Uncertainty - barrel	Uncertainty - endcaps
Data-MC comparison	9%	6%
JES	0.1%	0.1%
Pileup	0.3%	0.3%
ISR	0.1%	0.1%
RPC timing scaling	0.4%	-
Total RoI	9%	6%

Table 4.5: Summary of systematic uncertainty sources contributing to the total systematic uncertainty of the RoI Cluster trigger.

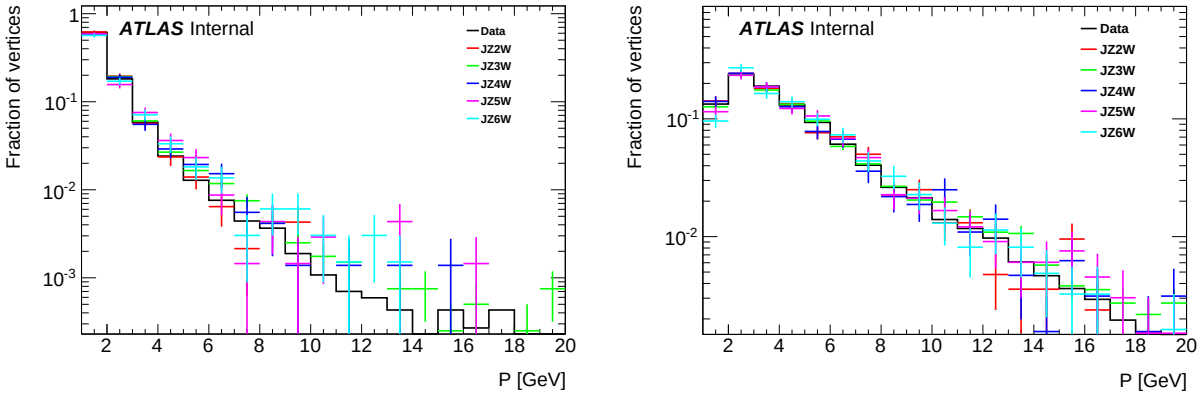

(a) (b)

Figure 4.30: The momentum, P, distribution of K_S^0 reconstructed in data and MC for the JZXW samples (a) in the barrel and (b) in the endcaps.

The ID vertex reconstruction uncertainty is determined in two steps. First, the difference in secondary track reconstruction efficiency between data and MC simulation for tracks with large impact parameters is determined from the observed distributions of K_S^0 decays as a function of vertex position in data versus MC simulation. In order to avoid the assumption that the K_S^0 yield is

identical in data and MC, the decay position distributions are scaled by the number of K_S^0 vertices inside the beampipe for the respective samples. The scaled decay position distributions for data and MC in the barrel and endcap are shown in Figure 4.31. Figure 4.32 shows the data-MC ratio of Figure 4.31. The weighted averages are 0.99 ± 0.03 in the ID barrel, and 1.01 ± 0.05 in the endcaps. The weighted average is consistent with one, and the statistical uncertainty, 3% in the barrel and 5% in the endcaps, is taken as the systematic uncertainty on the K_S^0 vertex reconstruction efficiency. Because each of the two tracks are necessary for K_S^0 vertex reconstruction, the K_S^0 reconstruction efficiency is proportional to the square of the track efficiency, and a per-track reconstruction uncertainty is therefore calculated using the following method:

$$\begin{aligned}
\text{(Data/MC) deviation in reconstructing } K_S^0 &= 1 - \varepsilon_{data}^{K_S^0} / \varepsilon_{MC}^{K_S^0} \\
&= 1 - (\text{Ratio of track reco. efficiency in data and MC})^2 \\
&= 1 - (1 - \text{Ratio of track reco. uncertainty in data and MC})^2
\end{aligned}$$

Inverting the above equation yields systematic uncertainties of 2% and 3% for track reconstruction in the barrel and endcaps, respectively.

The uncertainty of secondary track reconstruction is propagated to an uncertainty on ID vertex reconstruction. To propagate the track reconstruction uncertianty, 2% of barrel tracks and 3% of endcap tracks are randomly removed before running the vertex reconstruction algorithm on the signal MC samples. The difference between the efficiency curves produced with and without the track removal is taken as the systematic uncertainty on the vertex reconstruction efficiency.

Systematic uncertainties from pileup events, jet energy scale resolution and PDF also contribute to the total systematic uncertainty. Since the overlay MC was produced with the 2012 HCP dataset[2], the MC is re-weighted to match the $\langle\mu\rangle$ distribution in the full 2012 dataset. To evaluate the contribution from this re-weigthing, the $\langle\mu\rangle$ distribution in MC is shifted up and down by the

[2]The 2012 HCP dataset is the first 13 fb^{-1} of data that was collected in 2012.

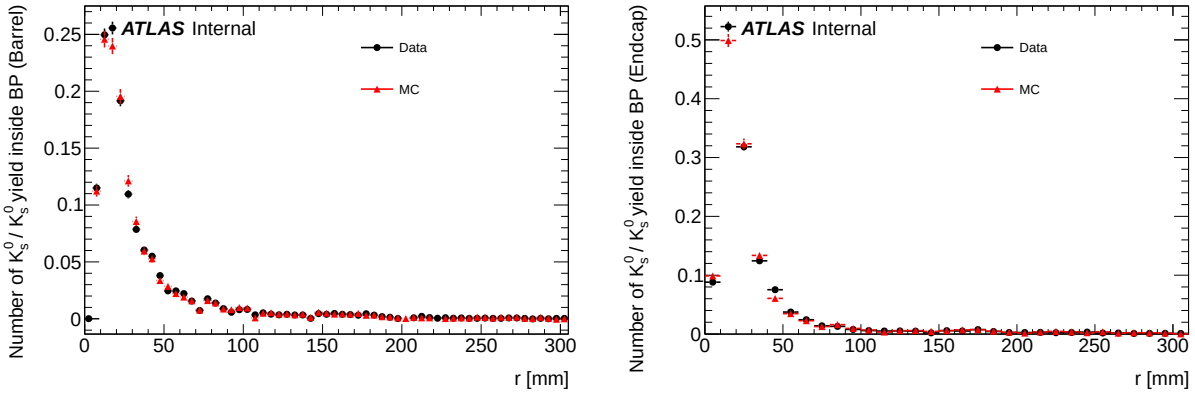

(a) (b)

Figure 4.31: The K_S^0 lifetime distribution normalized by the K_S^0 yield inside the beam pipe (a) in the barrel and (b) in the endcaps.

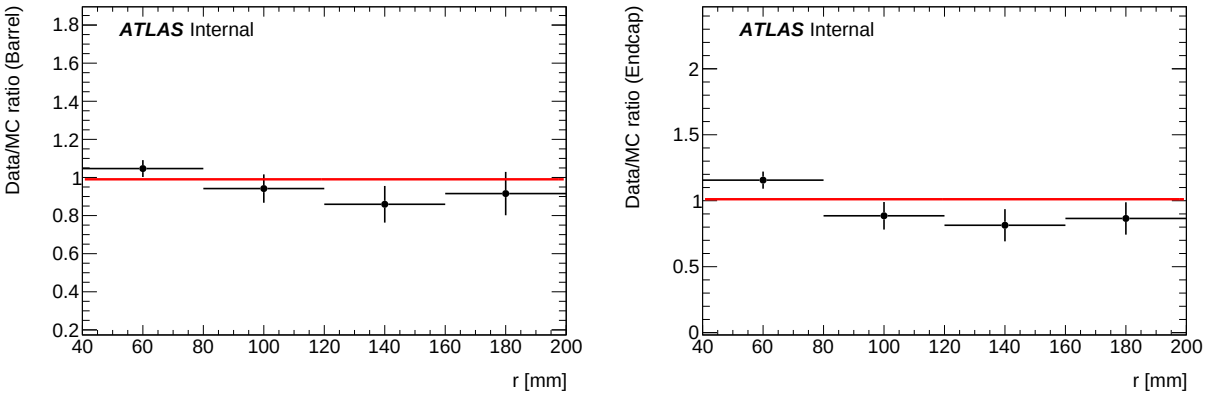

(a) (b)

Figure 4.32: The ratio of data to MC of the normalized lifetime yield (a) in the barrel and (b) in the endcaps. The red line, the weighted average value across all bins, shows the data-MC scale factor.

statistical uncertainty. The difference in the efficiency is calculated for each benchmark model, and the difference from the default efficiency is taken as the systematic uncertainty. The jet energy scale (JES) uncertainty for reconstructed jets is given by the standard "JESUncertaintyProvider"

tool. The p_{T} of all jets are shifted up/down by their relative uncertainty. The maximum difference in vertex reconstruction efficiency from the nominal is taken as the systematic uncertainty.

The PDF uncertainty is evaluated using a standard ATLAS tool that reweights MC events according to the probability of the event being generated if a different PDF were used. Events are assigned a weight by the tool, and the systematics is assigned as the difference in efficiency versus the unweighted efficiency.

All of the systematic uncertainties considered are added in quadrature to produce the total systematic uncertainty. Other possible sources of systematic uncertainty are negligible compared to the uncertainty related to the vertex reconstruction. Table 4.6 summarizes the ID vertex reconstruction systematic uncertainties for signal MC.

m_{Φ} [GeV]	$m_{\pi_{\mathrm{v}}}$ [GeV]	Vertex reconstruction	Pileup	JES	PDF	Total
100	10	1.6%	<0.1%	2.1%	0.4%	**2.7%**
100	25	2.0%	<0.1%	0.4%	0.2%	**2.1%**
125	10	2.1%	<0.1%	1.3%	0.4%	**2.5%**
125	25	2.4%	<0.1%	0.8%	0.2%	**2.5%**
125	40	2.3%	<0.1%	0.4%	0.3%	**2.4%**
140	10	2.2%	<0.1%	1.5%	0.2%	**2.7%**
140	20	2.6%	<0.1%	0.7%	0.2%	**2.7%**
140	40	1.5%	0.1%	0.5%	0.4%	**1.6%**
300	50	2.7%	<0.1%	0.4%	0.1%	**2.7%**
600	50	2.9%	<0.1%	0.2%	0.1%	**2.9%**
600	150	3.0%	0.1%	0.5%	0.2%	**3.1%**
900	50	3.5%	<0.1%	0.2%	0.2%	**3.5%**
900	150	2.9%	<0.1%	0.8%	0.2%	**3.0%**

Table 4.6: Summary of ID vertex systematic uncertainties for the Scalar boson benchmark samples.

4.4.3 Systematic Uncertainty of MS Vertex Reconstruction

A tracklet reconstruction systematic uncertainty is considered that follows the general procedure for ID vertex reconstruction. First, a comparison between data and MC is done on the distributions of number of tracklets found within a $\Delta R < 0.6$ cone of a punch-through jet. Figure 4.33 shows the distribution of number of tracklets. Figure 4.34 shows the ratio of data to MC. The weighted average of the ratio is 0.96 ± 0.05 in the barrel and 0.89 ± 0.05 in the endcaps, from which a systematic uncertainty for tracklet finding of 5% is assigned to the barrel and 11% to the endcaps.

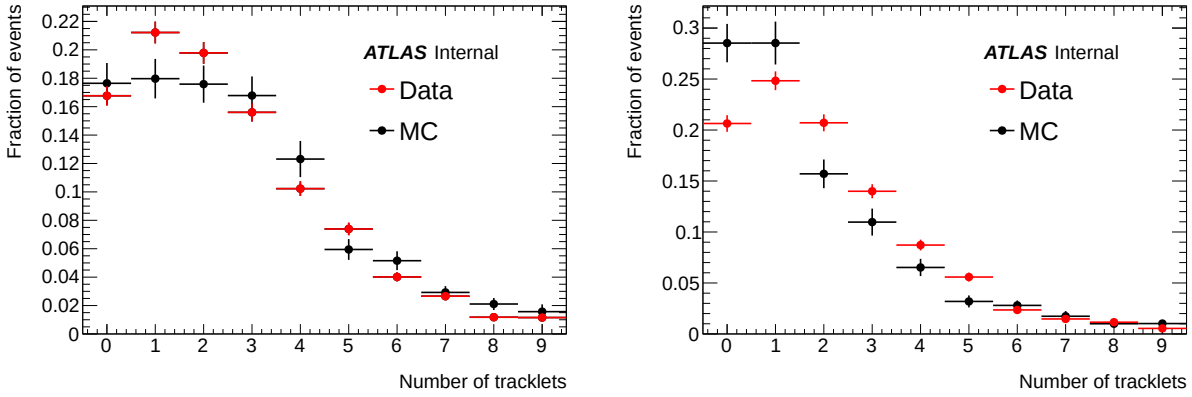

(a) (b)

Figure 4.33: The distribution on number of tracklets found within $\Delta R < 0.6$ of the jet axis (a) in the barrel and (b) in the endcaps.

The systematic uncertainty of tracklet reconstruction is propagated to MS vertex reconstruction by randomly removing tracklets with a probability equal to the tracklet reconstruction systematic uncertainty. The change in efficiency of reconstruction MS vertices gives the systematic uncertainty for each MC signal. This effect is illustrated for one signal sample in Figure 4.35 and Figure 4.36 and summarized in Table 4.7 and Table 4.8.

To understand the effects of JES uncertainty, pile-up uncertainty, PDF and ISR uncertainty on MS vertex reconstruction, the same procedure used for the Muon RoI Cluster trigger and the vertexing in the ID is applied. When the energy of each jet is increased by its JES uncertainty, the acceptance rate of MS vertices changes up to 0.2%. Shifting the $\langle\mu\rangle$ distribution in MC up and

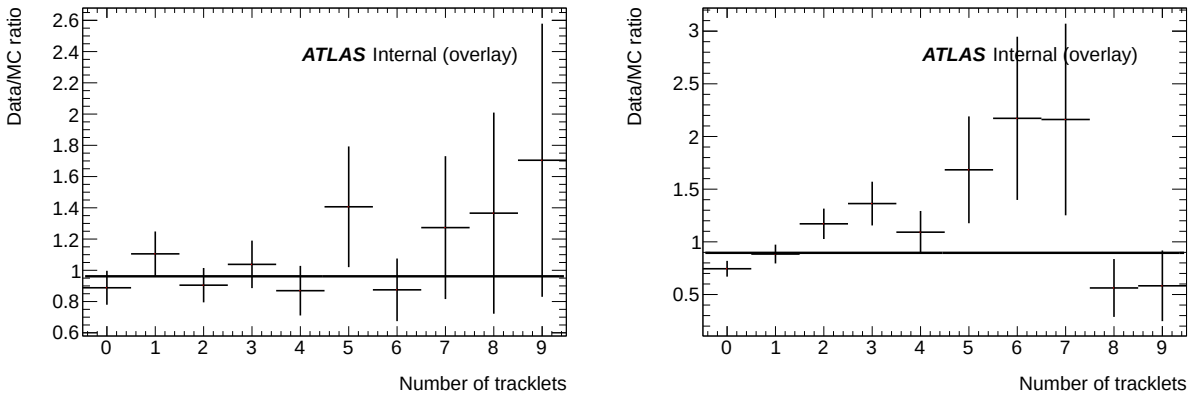

(a) (b)

Figure 4.34: The ratio of data to MC distributions on number of tracklets found within $\Delta R < 0.6$ of the jet axis (a) in the barrel and (b) in the endcaps.

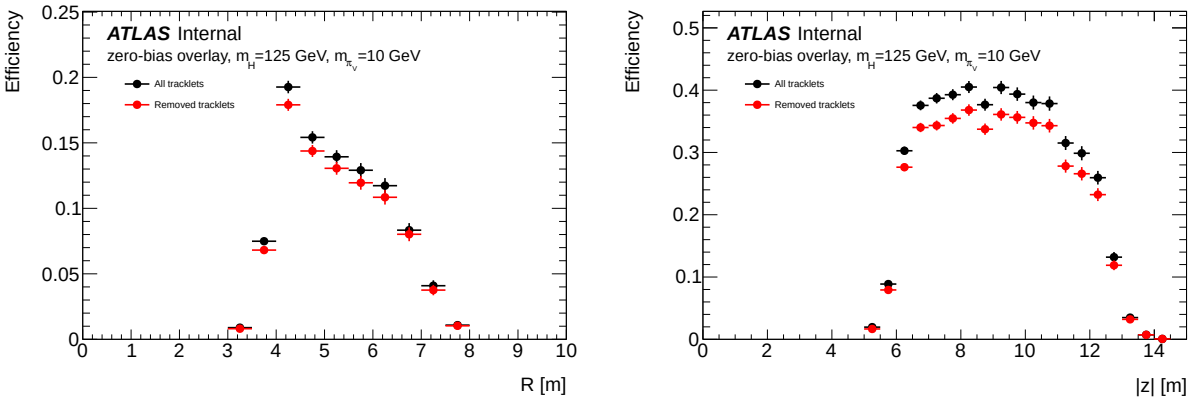

(a) (b)

Figure 4.35: Efficiency of MS vertex reconstruction for $m_H = 125$ GeV, $m_{\pi_v} = 10$ GeV sample with and without tracklets randomly removed in the (a) barrel and (b) endcaps.

down by the per-bin statistical uncertainties changes the acceptance of MS vertices up to 0.3%. The jet energy is fluctuated by 5% to account for ISR uncertainty [34], which changes the acceptance rate of MS vertices up to 0.3%. Weighting the events as a consequence of the PDF uncertainty,

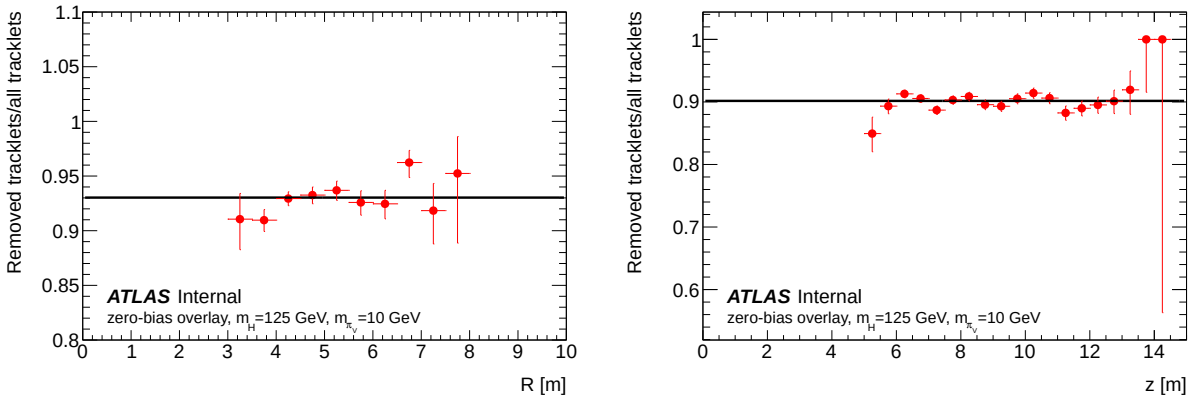

(a) (b)

Figure 4.36: Ratio of MS vertex efficiency for m_H = 125 GeV, m_{π_v} = 10 GeV sample before and after removing tracklets for (a) barrel and (b) endcaps.

results in MS vertex acceptance changes of up to 0.3%.

Other possible sources of systematic uncertainty are negligible compared to the uncertainty related to the vertex reconstruction. These results are summarized in Tables 4.7 and 4.8. As with the Muon RoI Cluster trigger, these effects are all small and the dominant uncertainty is from punch-through jet MC-data comparison. The total systematic uncertainty of reconstructing a vertex is found by adding in quadrature the contributions of all of the above systematic uncertainties.

4.5 Expected Number of Signal Events

Final event selection requires a trigger and two good displaced vertices. Two final-state combination topologies are considered according to the trigger and the combination of displaced vertices. The topologies are comprised of a trigger in combination with either two MS vertices or one ID vertex and one MS vertex. The topology of two ID vertices is not considered for events selected by the Muon RoI Cluster trigger since this trigger selects events with at least one long-lived particle decaying in the MS. The vertices are required to be separated by $\Delta R > 2$ since the π_v's should be well-separated in ΔR in the lab frame.

$m_\Phi(GeV)$	m_{π_v} (GeV)	Vertex reconstruction	Pile-up	ISR	JES	PDF	Total
100	10	6.8%	<0.1%	0.2%	0.1%	0.2%	**6.8%**
100	25	6.4%	<0.1%	<0.1%	<0.1%	0.1%	**6.4%**
125	10	7.0%	<0.1%	0.1%	0.1%	0.2%	**7.0%**
125	25	6.8%	<0.1%	<0.1%	<0.1%	0.1%	**6.8%**
125	40	6.5%	<0.1%	0.1%	0.1%	0.1%	**6.5%**
140	10	7.0%	<0.1%	0.1%	0.1%	0.2%	**7.0%**
140	20	6.6%	<0.1%	0.1%	0.1%	0.1%	**6.6%**
140	40	6.6%	<0.1%	<0.1%	0.1%	0.1%	**6.6%**
300	50	6.9%	<0.1%	<0.1%	0.1%	0.1%	**6.9%**
600	50	6.8%	<0.1%	0.1%	<0.1%	0.1%	**6.8%**
600	150	6.6%	<0.1%	0.1%	<0.1%	0.1%	**6.6%**
900	50	6.6%	<0.1%	0.1%	<0.1%	0.1%	**6.6%**
900	150	5.9%	<0.1%	0.1%	0.1%	0.1%	**5.9%**

Table 4.7: Summary of MS vertex systematic uncertainty in the barrel for the Scalar boson benchmark samples.

A "toy model" technique is used to evaluate the expected number of signal events for an arbitrary lifetime. This approach utilizes Pythia-level event generation without full detector simulation, digitization, and reconstruction. These events are called "toys" because they lack the full event description, but they are useful because they allow production of large statistics of events that correctly model the momenta of the π_v. Samples of two million toy events are generated in Pythia for each benchmark to sample the π_v's momenta for a large number of events. The toy model is then run for mean proper lifetimes between 0 and 1 m in 0.25 cm steps, 1 m and 11 m, in 2.5 cm steps, and 11 m and 100 m in 25 cm steps.

For each mean proper lifetime, the time to decay for each long-lived particle is calculated

$m_\Phi(GeV)$	m_{π_v} (GeV)	Vertex reconstruction	Pile-up	ISR	JES	PDF	Total
100	10	11.2%	<0.1%	0.1%	0.1%	0.1%	**11.2%**
100	25	10.4%	<0.1%	0.1%	0.1%	0.1%	**10.4%**
125	10	9.9%	<0.1%	0.1%	0.1%	0.1%	**9.9%**
125	25	9.7%	<0.1%	0.1%	0.1%	0.1%	**9.7%**
125	40	8.0%	<0.1%	0.1%	0.1%	0.1%	**8.0%**
140	10	9.6%	<0.1%	0.1%	0.1%	0.1%	**9.6%**
140	20	9.6%	<0.1%	0.1%	0.1%	0.1%	**9.6%**
140	40	7.9%	<0.1%	0.1%	0.1%	0.1%	**7.9%**
300	50	6.3%	<0.1%	0.1%	0.1%	0.1%	**6.3%**
600	50	5.4%	<0.1%	0.1%	0.1%	0.1%	**5.4%**
600	150	4.0%	<0.1%	0.1%	0.1%	0.1%	**4.0%**
900	50	5.7%	<0.1%	0.1%	0.1%	0.1%	**5.7%**
900	150	3.8%	<0.1%	0.1%	0.1%	0.1%	**3.8%**

Table 4.8: Summary of MS vertex systematic uncertainty in the endcaps for the Scalar boson benchmark samples.

by sampling a random number from the exponential distribution governing the particle's decay probability, shown in Equation 4.1. Its decay position in the detector is then calculated using the momentum generated by Pythia.

$$P(t) = \exp(-t/(\gamma\tau)) \tag{4.1}$$

Using the known probabilities of reconstructing a Muon RoI Cluster trigger, an ID vertex, and an MS vertex as a function of decay position, the overall probability of each event passing the selection criteria is evaluated. Other important criteria, such as the timing acceptance window for the barrel RoI Cluster trigger, are also taken into account. The procedure is then repeated for

each of the two million generated events, and the expected number of signal events for a particular lifetime is obtained by scaling the number of toy MC events by the production cross section and the 2012 luminosity.

The expected number of signal events at the proper lifetime used in the official MC simulation are shown in Table 4.9 for the $H \to \pi_v \pi_v$ process with $m_H = 125$ GeV and m_{π_v} = 10, 25, 40 GeV. Figure 4.37 shows the expected number of signal events for lifetimes between 0 m and 100 m. The dashed lines represent $\pm 1\sigma$, encompassing all statistical and systematic uncertainties in the analysis.

Sample		Event yields					
m_H [GeV]	m_{π_v} [GeV]	MS_B+ID	MS_E+ID	MS_B+MS_B	MS_B+MS_E	MS_E+MS_E	Total
125	10	0.4 ± 0.3	1.5 ± 0.5	17 ± 2	102 ± 4	115 ± 5	236 ± 7
125	25	25 ± 2	37 ± 3	106 ± 4	285 ± 7	299 ± 7	753 ± 12
125	40	19 ± 2	22 ± 2	45 ± 3	80 ± 4	188 ± 6	354 ± 8

Table 4.9: Expected number of signal events for the $H \to \pi_v \pi_v$ process with $m_H = 125$ GeV and m_{π_v} = 10, 25, 40 GeV, at a proper lifetime of 2 m. In addition to the total number of expected signal events, yields are shown separately for each considered topology. The branching ratio is assumed to be 100% and the SM Higgs cross section for gluon-fusion production is used, $\sigma_{SM} = 18.97$ pb. The numbers for the Scalar boson search are scaled to the 2012 integrated luminosity, 19.5 fb^{-1}. The uncertainties are statistical only.

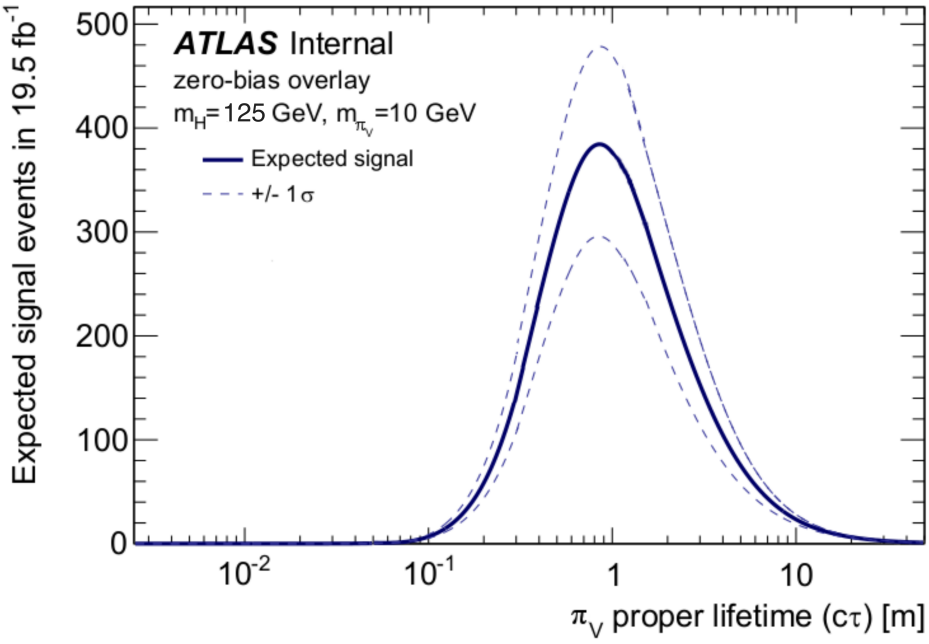

Figure 4.37: Expected number of signal events for the Scalar boson sample with $m_H = 125\,\text{GeV}$, $m_{\pi_v} = 10\,\text{GeV}$ in the 2012 dataset.

Chapter 5

BACKGROUNDS

5.1 Expected number of background events

In order to estimate the background, it is necessary to quantify the frequency at which the ID and MS vertex algorithms reconstruct vertices for non-signal events. Such *fake vertices* identify a vertex in an event that does not contain a long-lived particle decay. In this analysis, the frequency of fake vertex reconstruction is estimated from data events. Calculating the fake rate from data events has the advantages of avoiding possible systematic errors from using simulated events yielding smaller statistical uncertainties because there are relatively few simulated events of the dominant background processes.

5.1.1 ID vertex fake rate

The primary background of ID vertex reconstruction is due to jets containing many charged tracks that fake a displaced decay signature. A fake rate of ID vertex reconstruction is found by looking in a sample of data orthogonal to the signal region.

A control region is defined with events that contain jets of $p_{\mathrm{T}} > 230$ GeV. The per-jet fake rate, found as a function of jet p_{T}, is determined by finding the probability for a nonleading jet to contain an ID vertex. The leading jet's large p_{T} requirement effectively excludes events from the considered long-lived signal. The nonleading jet p_{T} spectrum is comparable with the spectrum found in events passing the RoI Cluster Trigger, which is important since the fake rate is a function of the jet's p_{T}. The probability for a jet to fake an ID vertex ranges from 2×10^{-5} to 3×10^{-4} and is shown in Figure 5.1.

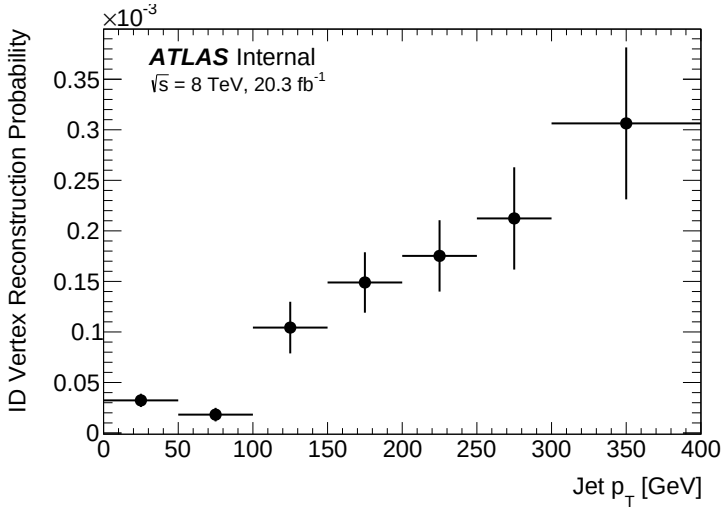

Figure 5.1: The probability of ID vertex reconstruction as a function of jet pT after vertex selection criteria have been applied.

5.1.2 MS vertex fake rate

The fraction of events passing the Muon RoI Cluster trigger or a minimum bias trigger that contain a good, reconstructed MS vertex is determined. Such events with a single vertex are assumed to be fake vertices, not due to displaced decays. Signal events could contaminate the control region, and that would result in the probabilities and the resulting background rates to be overestimated.

The following measurable quantities are calculated from data, with descriptions of how they are calculated to follow:

N(1 MS trig, 1 MSVTX) Number of events with a vertex in the spectrometer

N(2 MS trig, 1 MSVTX, 1 UM barrel trig) Number of events with two distinct RoI Cluster triggers, one matching an MS vertex and the other unmatched trigger located in the barrel

N(2 MS trig, 1 MSVTX, 1 UM endcaps trig) Number of events with two distinct RoI Cluster triggers, one matching an MS vertex and the other unmatched trigger located in the endcaps

P(MSVTX | no MS trig) Probability to reconstruct an MS vertex for events that do not pass the RoI Cluster trigger

P(MSVTX | barrel MS trig) Probability to reconstruct an MS vertex for events that passed the RoI Cluster trigger in the barrel

P(MSVTX | endcaps MS trig) Probability to reconstruct an MS vertex for events that passed the RoI Cluster trigger in the endcaps

To measure P(MSVTX | no MS trig), a sample of minimum bias events were used. Zero events that contained a good MS vertex were found out of 6,168,200 minimum bias events. From this, the best estimate of P(MSVTX | no MS trig) is zero, and the true value of P(MSVTX | no MS trig) is less than 3/6,168,200 = 4.86 x 10^{-7} at the 95% confidence level.[1] The value (0^{+5}_{-0}) x 10^{-7} is taken to be P(MSVTX | no MS trig).

The number of background events that passed the RoI cluster trigger and have two acceptable RoI clusters separated by $\Delta R > 2.0$ and one reconstructed vertex is determined in data. Thirteen such events are found; in nine events, the RoI cluster that does not overlap with the MS vertex is found in the barrel and in four events in an endcap. This gives a value of 9^{+4}_{-3} for N(2 MS trig, 1 MSVTX, 1 UM barrel trig) and 4^{+3}_{-2} for N(2 MS trig, 1 MSVTX, 1 UM endcaps trig). The uncertainties on these values, and other small numbers for which $\sigma_n = \sqrt{n}$ is not appropriate, are the 68% frequentist confidence interval.

The probability of reconstructing a vertex in an event that passes the RoI cluster trigger in the barrel (endcaps) is calculated from data to be the fraction of events that have an MS vertex out of all events with an RoI cluster in the barrel (endcaps). From this, the probability to reconstruct an

[1] The 95% confidence interval is determined by taking the Poisson approximation of the binomial distribution, which is an applicable approximation when the number of events is large and the per-event probability of observation is low. The Poisson distribution gives the probability P of making n observations in a trial with a mean number of observations per trial μ by the equation $\mathrm{P}(n;\mu) = \frac{\mu^n e^{-\mu}}{n!}$. When zero events are observed in a trial, a confidence interval of 95% on μ is given by $P(0,\mu) = \mu^0 e^{-\mu}/0! = 0.05 \Rightarrow \mu = -\log 0.05 = 2.9957... \approx 3$. The approximate result, 3, is thus used when estimating P(MSVTX | no MS trig).

Quantity	Number of Events	Value
N(1 MS trig, 1 MSVTX)	103,999	$(1.04 \pm 0.03) \times 10^5$
N(2 MS trig, 1 MSVTX, 1 UM barrel trig)	9	9^{+4}_{-3}
N(2 MS trig, 1 MSVTX, 1 UM endcaps trig)	4	4^{+3}_{-2}
P(MSVTX | no MS trig)	0/6,168,200	$(0^{+5}_{-0}) \times 10^{-7}$
P(MSVTX | barrel MS trig)	48,127/3,733,031	$(1.289 \pm 0.006) \times 10^{-2}$
P(MSVTX | endcaps MS trig)	55,859/698,489	$(8.00 \pm 0.03) \times 10^{-2}$

Table 5.1: The number of events and probabilities needed to compute the background to fake events containing MS vertices.

MS vertex when an RoI cluster is in the barrel is 48,127/3,733,031 = (1.289 $\pm$ 0.006) x 10^{-2} and in the endcaps is 55,859/698,489 = (8.00 $\pm$ 0.03) x 10^{-2}.

The probability of reconstructing a vertex in events passing the RoI cluster trigger in the barrel was also calculated on data collected from unpaired, isolated bunch crossings[2]. This provides a cross-check that the measured value of P(MSVTX | barrel MS trig) is a reasonable result. The probability was found to be 18/4,290 = $(4.2^{+1.2}_{-1.0}) \times 10^{-3}$. A larger probability was found with collision events than with unpaired, isolated bunch crossings, so the value determined with collision events is used to provide a more conservative estimate of the background when setting exclusion limits.

5.1.3 Expected background of events passing Muon RoI Cluster trigger with two reconstructed vertices

In the Scalar boson scenario, events are selected by the RoI Cluster trigger and final analysis requires two reconstructed vertices separated by $\Delta R > 2.0$. Since at least one long-lived particle

[2]Unpaired and isolated bunches are classifications of special events used to monitor background rates. An unpaired, isolated bunch crossing contains a bunch in only one of the beams and no bunches in the previous 3 bunch crossings (150 ns) [35].

must decay in the MS to pass the RoI Cluster trigger, the search considers combinations of ID+MS and MS+MS vertices.

Muon RoI Cluster trigger + ID vertex + MS vertex

The number of events with a combination of an MS and ID vertex is estimated by multiplying the number of events passing an RoI Cluster trigger with an MS vertex by the probability of finding a fake ID vertex in the event. For each event, the probability of a fake ID vertex being found approximately equals the number of jets in the event multiplied by the ID vertex per-jet fake rate. The total number of expected events with one ID vertex and one MS vertex is given by the following equation, where nJet_i correponds to the number of jets present in event i:

$$N_{\text{Fake}}(\text{MS trig, 1 IDVTX, 1 MSVTX}) = \sum_{i}^{\text{RoI+MSVx events}} \text{nJet}_i * P_{\text{ID,reco}}.$$

There are 39,366 events in data collected in 2012 that pass the event selection requirements and also have a reconstructed MS vertex that passes selection criteria. The per-jet fake ID vertex reconstruction rate shown in Figure 5.1 is applied to all selected jets in these events, and the resulting expected number of events is $N_{\text{Fake}}(\text{MS trig, 1 IDVTX, 1 MSVTX}) = 2.0 \pm 0.4$.

Muon RoI Cluster trigger + MS vertex + MS vertex

The number of events with two MS vertices is calculated as follows:

N_{Fake}(MS trig, 2 MSVTX) =

N(1 MS trig, 1 MSVTX) * P(MSVTX | no MS trig) +

N(2 MS trig, 1 MSVTX, 1 UM barrel trig) * P(MSVTX | barrel MS trig) +

N(2 MS trig, 1 MSVTX, 1 UM endcaps trig) * P(MSVTX | endcaps MS trig)

In this equation, the first term finds the number of events that contain an RoI Cluster trigger and an MS vertex. Such events have a probability of P(MSVTX | no MS trig) of containing a second MS vertex by chance. The second and third terms correspond to events that contain two RoI Clusters, one of which has an overlapping MS vertex. As shown in Figure 5.2, these two terms account for all the topological combinations of RoI Clusters and MS vertices found in

either the barrel or endcaps. The other, unmatched RoI Cluster will contain an MS vertex with a probability P(MSVTX | barrel MS trig) or P(MSVTX | endcaps MS trig), depending on whether the unmatched RoI is found in the barrel or endcaps. Because P(MSVTX | barrel MS trig) and P(MSVTX | endcaps MS trig) $\gg$ P(MSVTX | no MS trig), the possibility of a vertex being present unassociated with the unmatched RoI Cluster trigger is negligible.

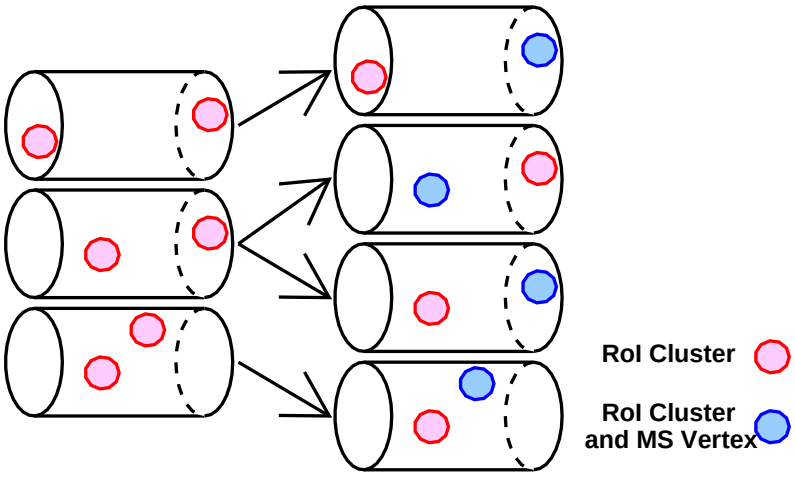

Figure 5.2: For events with two independent RoI clusters present, the clusters can be found both in the barrel, both in the endcaps, or one in each. When one of the two RoI clusters has an overlapping MS vertex, there are four resulting combinations of matched and unmatched RoI cluster locations.

From this equation, the expected number of events is N_{Fake}(MS trig, 2 MSVTX) = $0.4^{+0.3}_{-0.2}$.

Chapter 6

RESULTS AND CONCLUSION

6.1 Observed events

After applying all selection criteria, two events are found containing two reconstructed MS vertices in events passing the Muon RoI Cluster trigger. Table 6.1 summarizes the number of events observed and the expected number of events from background.

Trigger	Topology	Predicted	Observed
Muon RoI Cluster	ID+MS	2.0 ± 0.4	0
Muon RoI Cluster	MS+MS	$0.4^{+0.3}_{-0.2}$	2

Table 6.1: Number of events predicted and observed for different final-state topologies.

The events that contain two reconstructed vertices can be shown using ATLAS event display Persint [36]. Figure 6.1 shows one of the data events with two reconstructed MS vertices. In this event, one MS vertex is reconstructed in an endcap and the other MS vertex is reconstructed in the barrel. This event shows a very high level of activity throughout the muon spectrometer, particularly in the upper half. There are regions of the muon spectrometer that contain greater than 3000 MDT hits, so if an MS vertex were reconstructed there, the vertex would not pass the good vertex criteria. Since this event has significant activity throughout the detector, it is not consistent with the signature of two separated, distinct MS vertices that is being searched for. This event is consequently considered to be a background event. Future studies could implement a good event criteria, requiring that there not be large amounts of continuous MS detector activity. The specifics of such a criteria requires further study. This event could be due to a cosmic particle that interacts

inside the detector cavern and showers across the entire detector.

Figure 6.2 shows a second event with two reconstructed MS vertices. Both vertices are reconstructed in a single endcap. This event contains a Moore track in the opposite MS endcap, roughly parallel to the beamline, near the same ϕ position as the MS activity that reconstructs two vertices. A plausible explanation is that this is a beam halo event that survives the beam halo cut because it did not deposit energy in the calorimeter. The MS vertex reconstruction algorithm finds two vertices on the outer edges of a single region of activity in the MS endcap. The two vertices are separated by $\Delta R = 2.03$. Since there is a single region of MS activity that finds two vertices barely above the required ΔR separation of 2.0, this is also assumed to be a background event. Such an event could possibly be removed from future analyses if a different beam halo cut were implemented or by requiring a larger $\Delta\phi$ between MS vertices found in a single endcap.

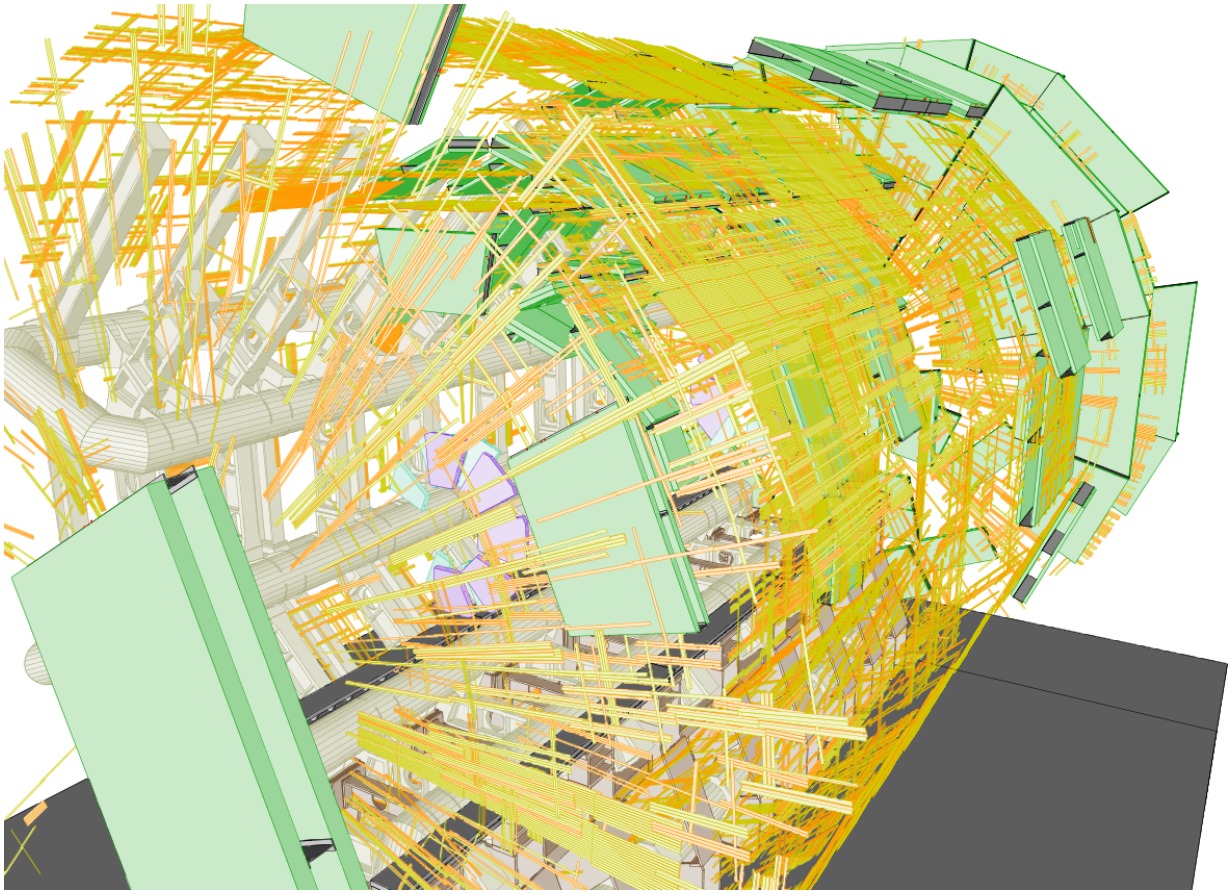

(a)

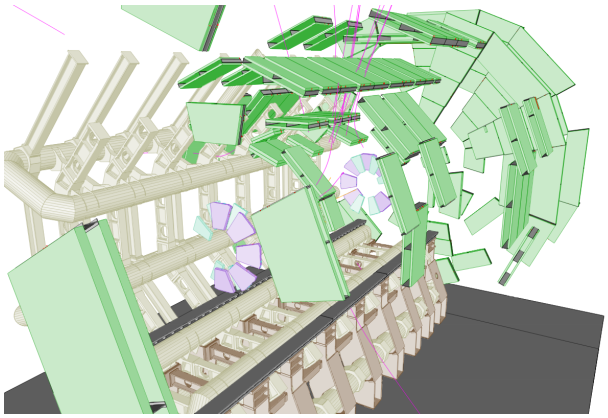

(b)

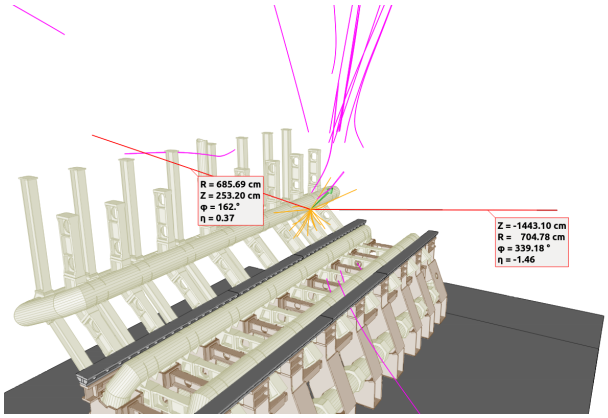

(c)

Figure 6.1: Event display of a data event containing two MS vertices. One vertex is reconstructed in the endcap and the other is reconstructed in the barrel. Trigger RPC/TGC hits are drawn in yellow and orange in (a). Green muon spectrometer chambers are drawn if a muon segment is reconstructed within the chamber in (a) and (b). Moore tracks are drawn in magenta. Red lines connect the nominal interaction point to the reconstructed MS vertex in (c).

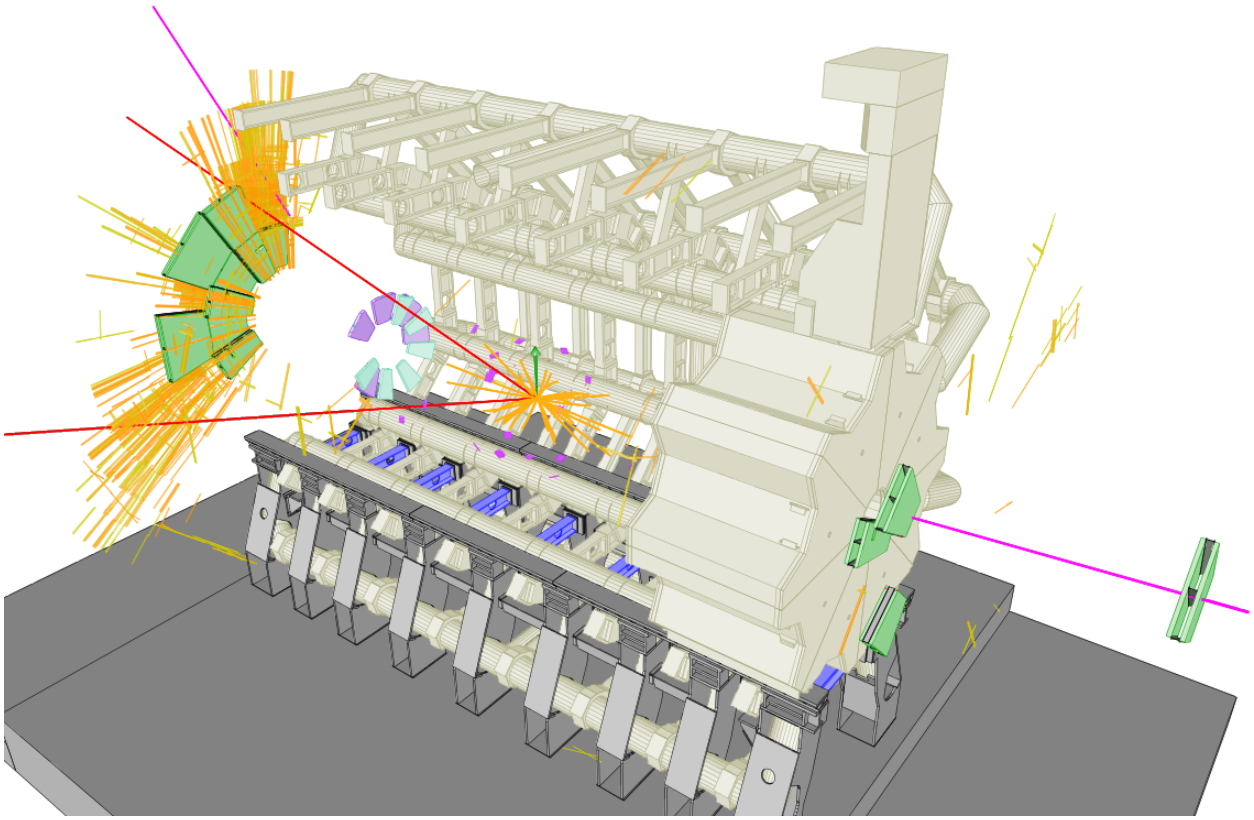

(a)

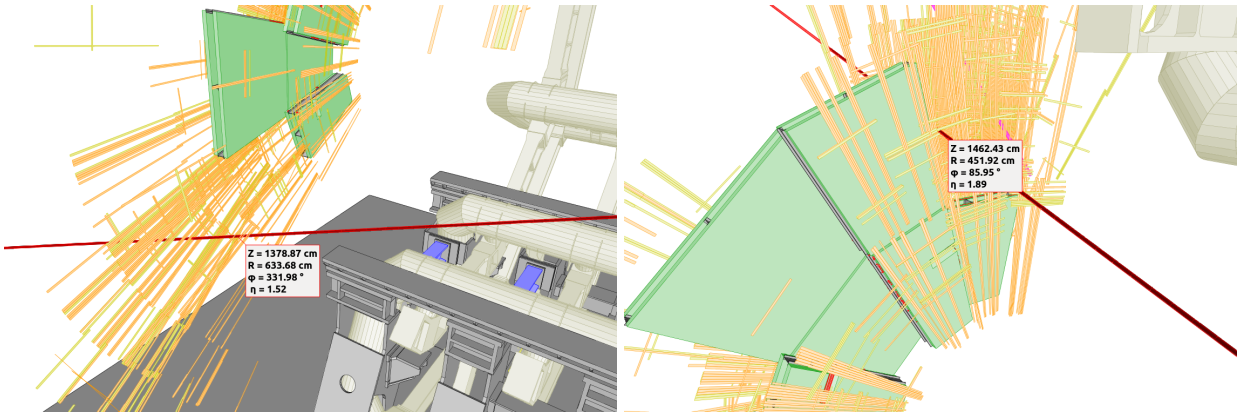

(b) (c)

Figure 6.2: Event display of a data event containing two MS vertices. Both vertices are found in close proximity in one endcap. Trigger RPC/TGC hits are drawn in yellow and orange. Green muon spectrometer chambers are drawn if a muon segment is reconstructed within the chamber. Moore tracks are drawn in magenta. Red lines connect the nominal interaction point to the reconstructed MS vertex. The green arrow at the interaction point shows the direction of $E_{\mathrm{T}}^{\mathrm{miss}}$.

6.2 Limits

The number of observed events are compatible with the expected background. The Confidence Limits (CLs) technique is used to determine upper limits on the production rate of each of the signal samples.

The CLs technique finds a value, CL_s, which is the approximate confidence in the signal-only hypothesis. The value for CL_s is found as the ratio of two frequentist probabilities CL_{s+b} and CL_b. The term CL_{s+b} is the probability of making the given observation in the background plus signal hypothesis. Similarly, the term CL_b is the probability of making the given observation in the background-only hypothesis. The terms CL_{s+b} and CL_b are calculated from the probability of finding at least the two observed events from a Poisson distribution with an expected value parameter derived from the signal plus background or background-only caclulation, respectively. All the systematic uncertainties previously described are propagated to derive the corresponding uncertainties in the expected number of signal events. These uncertainties are then included as nuissance parameters in their effect on the mean of the Poisson functions and through convolution with their assumed Gaussian distributions. The number of expected events in signal MC, together with the expected background estimation and all the systematic uncertainties are input for computing the confidence limit values.

Using the CLs technique, the exclusion intervals where $CL_s < 5\%$ are identified as upper limits on production cross section as a function of π_v lifetime. For the $m_H = 125$ GeV Scalar boson, the signal strength is parameterized in terms of σ/σ_{SM}, where $\sigma_{SM} = 18.97$ pb is the cross section of SM Higgs production via gluon fusion. A limit on σ/σ_{SM} is thus a limit on the branching ratio of $H \to \pi_v\pi_v$. For the other scalar boson masses considered, the signal strength is parameterized in terms of $\sigma \times \mathrm{BR}$, a limit on the product of the scalar boson production cross section and the branching ratio of $\Phi \to \pi_v\pi_v$.

Figures 6.3 - 6.10 show the limits for each of the models considered. The limits on lifetime for select branching ratios of the SM Higgs boson are shown in Table 6.2. Figure 6.9 shows that a significant range of π_v lifetimes are excluded to below 5% branching ratio for a SM Higgs boson

decaying to long-lived particles. These results demonstrate strong limits on a scalar boson's ability to decay to back-to-back long-lived particles for a sizable range of lifetimes.

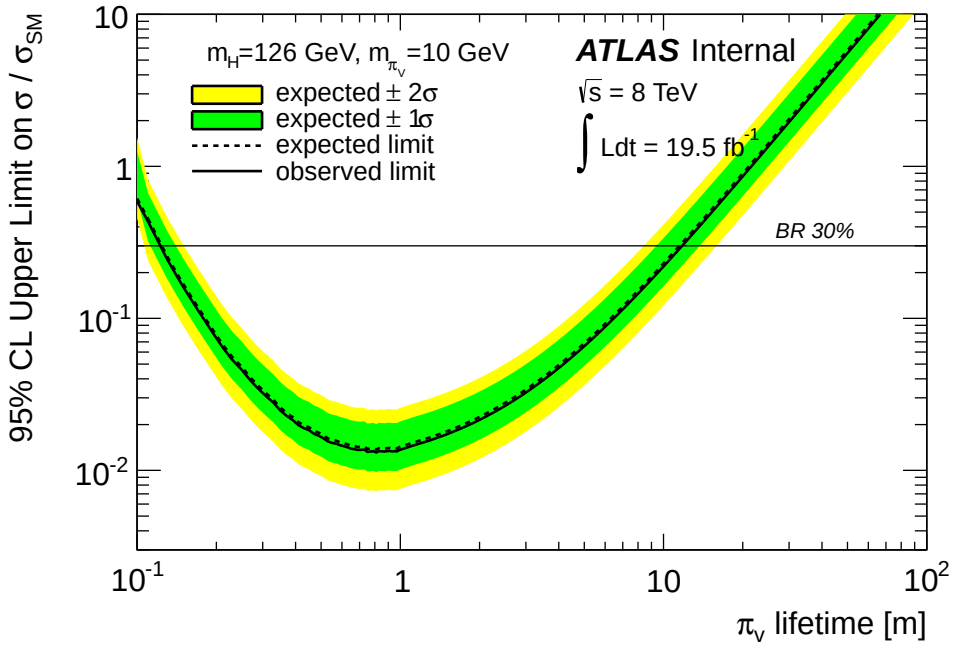

Figure 6.3: Expected and observed 95% CL limits on σ/σ_{SM} as a function of the π_v proper lifetime for m_H = 125 GeV and m_{π_v} = 10 GeV. The horizontal solid line corresponds to a 30% BR.

Table 6.2: Ranges of π_v proper decay lengths excluded at 95% CL assuming a 30%, 15%, or 5% BR for $m_H = 125$ GeV.

$m_H[GeV]$	m_{π_v} [GeV]	Excluded range [m]		
		5% BR	15% BR	30 % BR
125	10	0.24–4.2	0.16–8.1	0.12–11.8
125	25	0.43–18.6	0.28–33.6	0.21–47.7
125	40	1.02–30.6	0.63–56.0	0.52–79.5

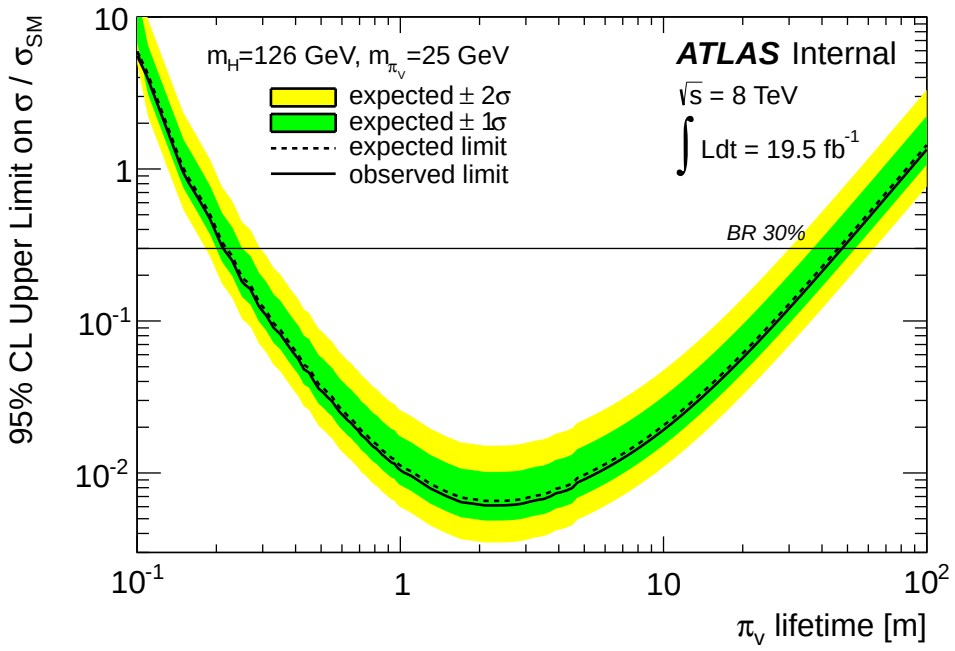

Figure 6.4: Expected and observed 95% CL limits on σ/σ_{SM} as a function of the π_v proper lifetime for m_H = 125 GeV and m_{π_v} = 25 GeV. The horizontal solid line corresponds to a 30% BR.

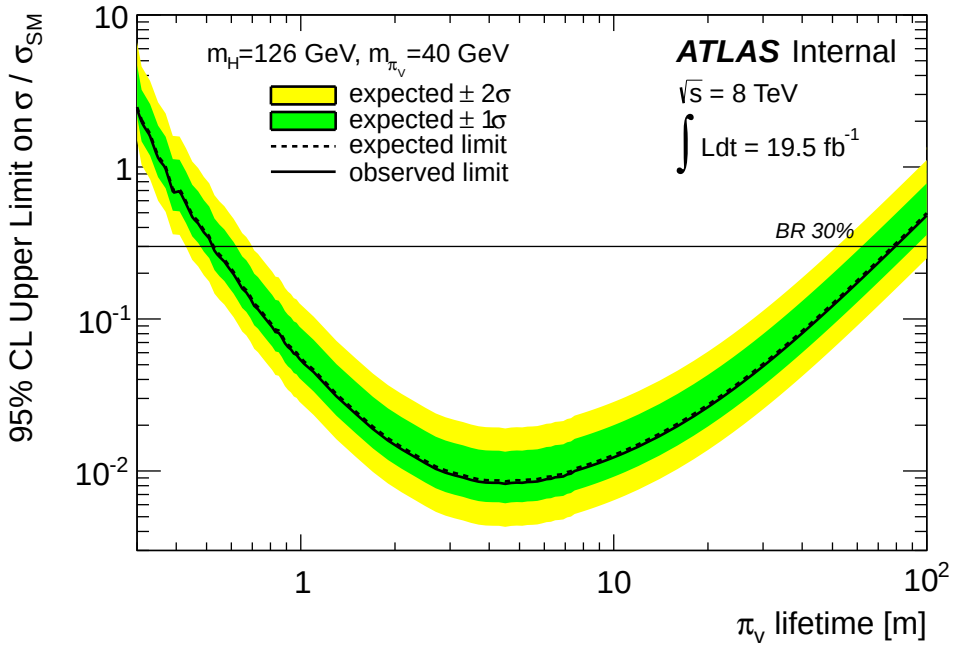

Figure 6.5: Expected and observed 95% CL limits on σ/σ_{SM} as a function of the π_v proper lifetime for m_H = 125 GeV and m_{π_v} = 40 GeV. The horizontal solid line corresponds to a 30% BR.

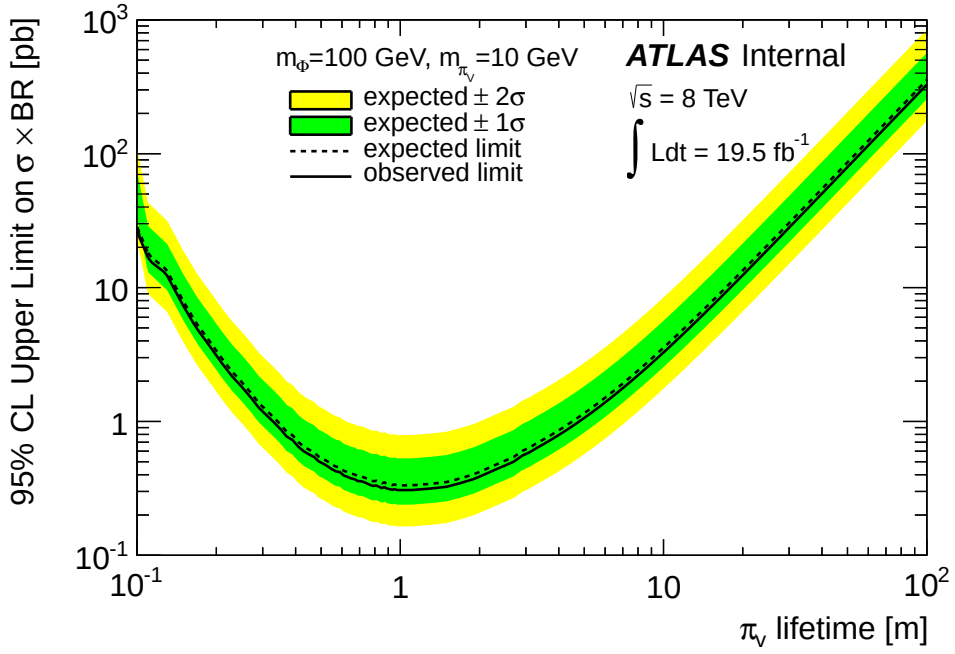

(a)

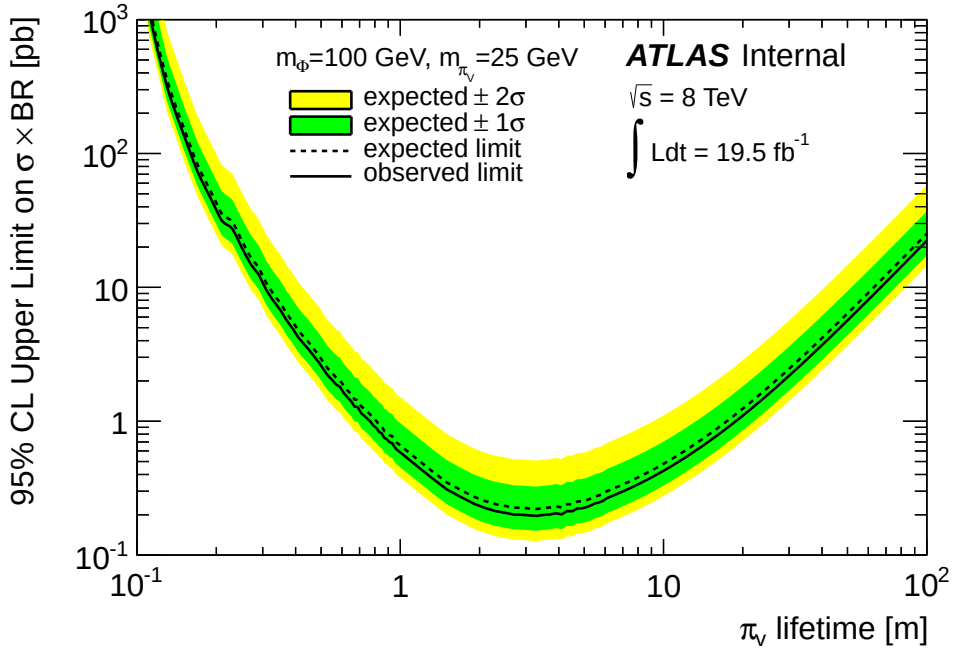

(b)

Figure 6.6: Expected and observed 95% CL limits on $\sigma\times$ BR as a function of the π_v proper lifetime for m_Φ = 100 GeV and m_{π_v} = 10 and 25 GeV.

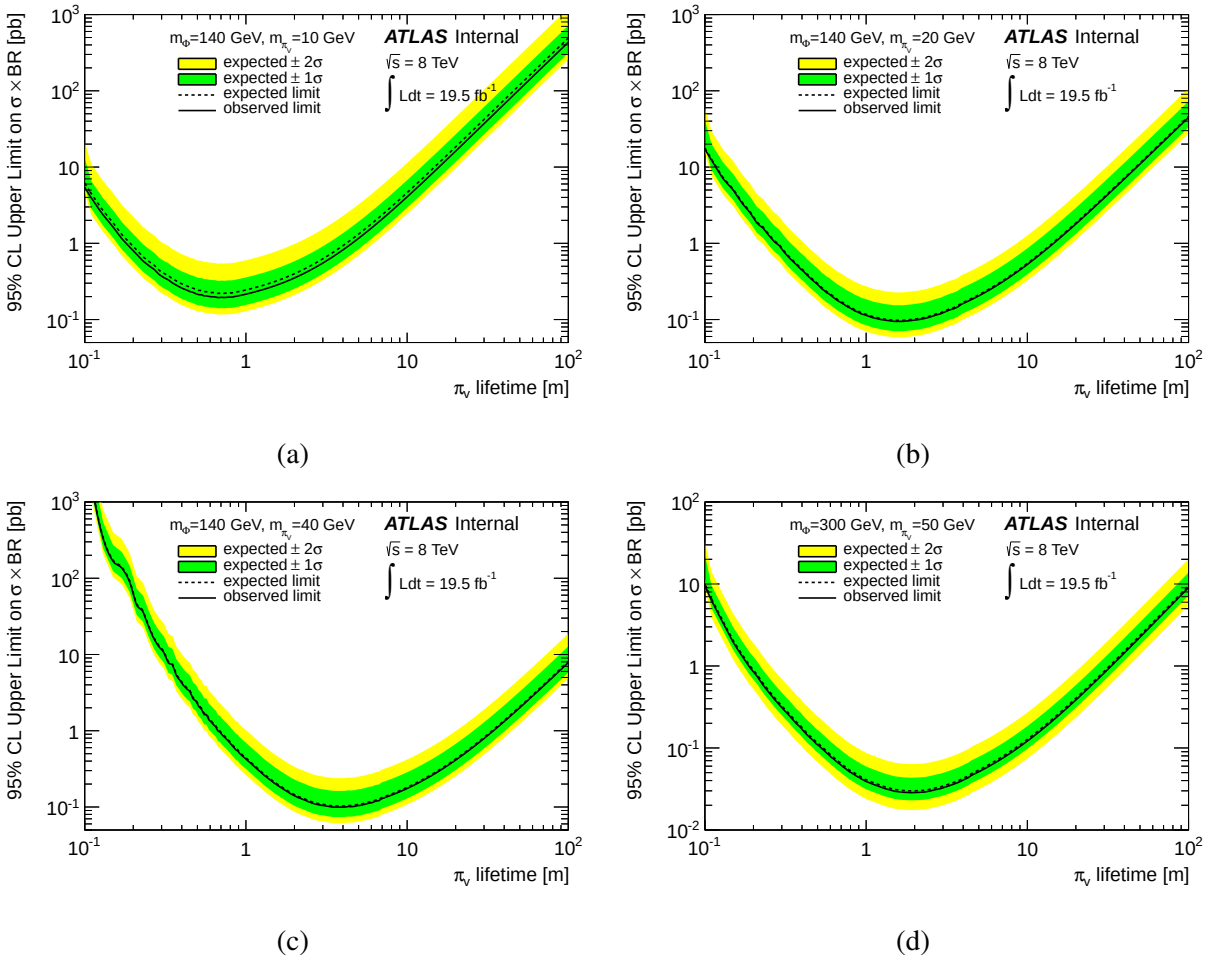

Figure 6.7: Expected and observed 95% CL limits on $\sigma \times$ BR as a function of the π_v proper lifetime for m_Φ = 140 GeV and m_{π_v} = 10,20, and 40 GeV and for m_Φ = 300 GeV and m_{π_v} = 50 GeV.

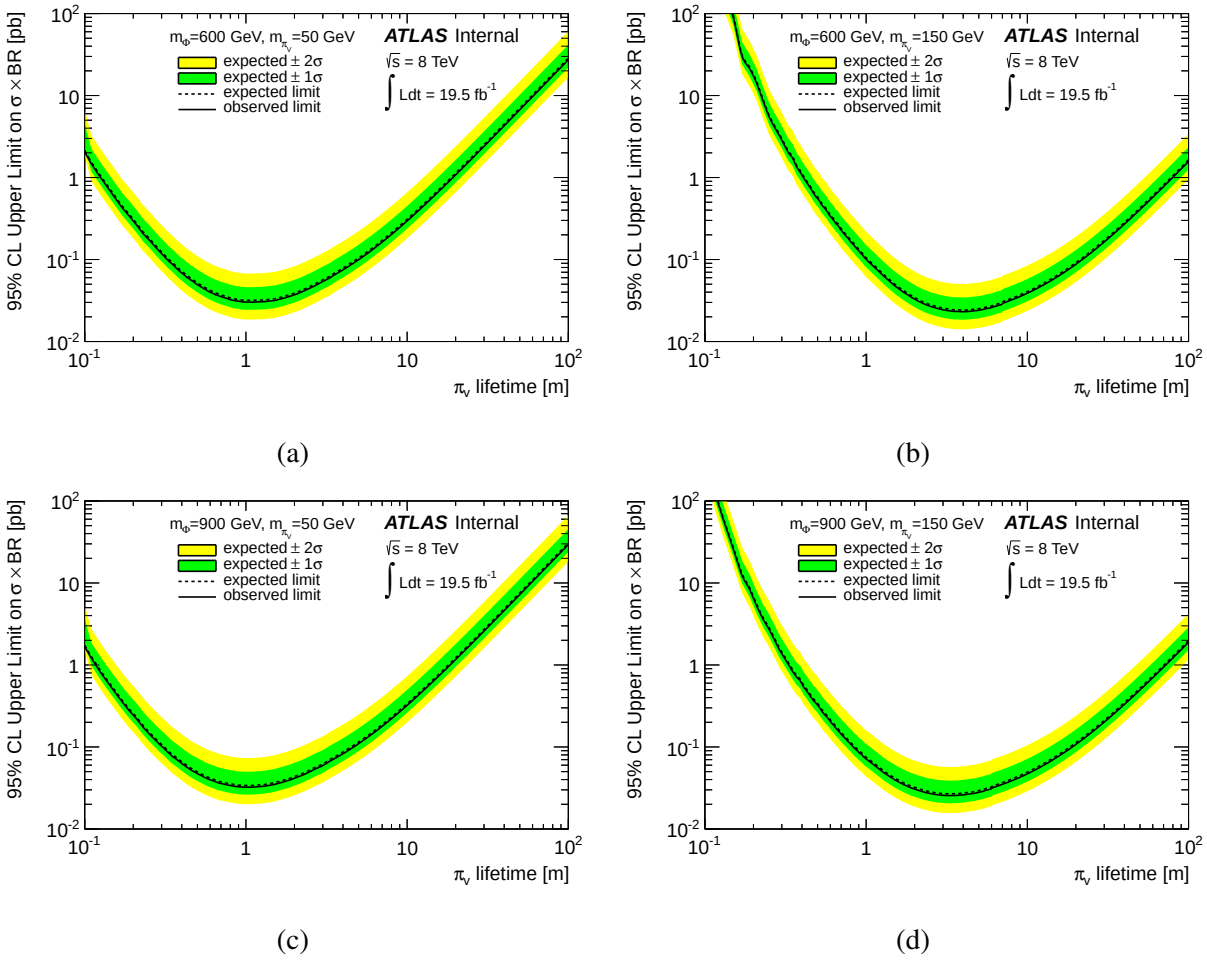

Figure 6.8: Expected and observed 95% CL limits on $\sigma \times$ BR as a function of the π_v proper lifetime for m_Φ = 600 and 900 GeV and m_{π_v} = 50 and 150 GeV.

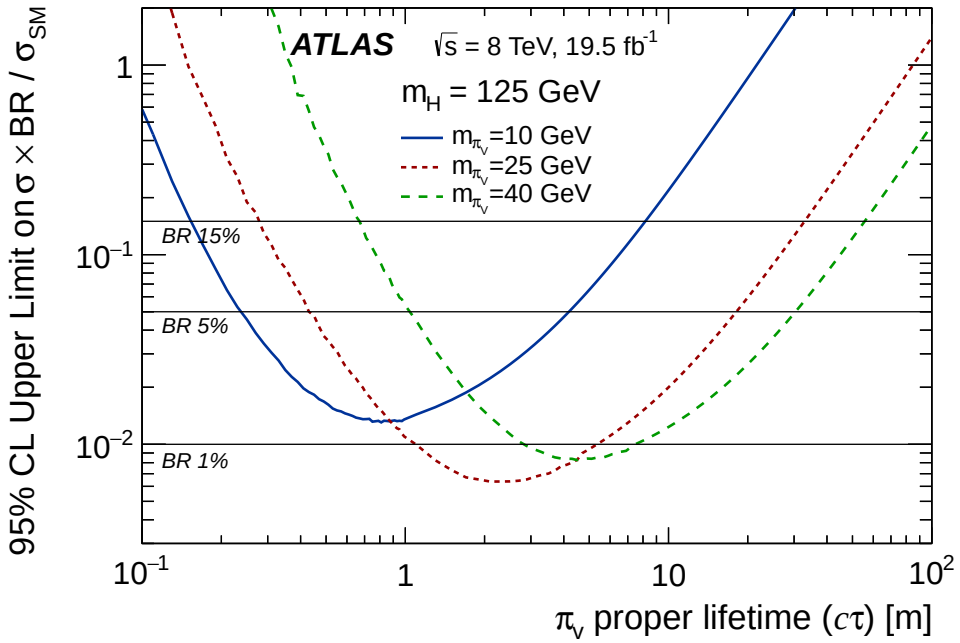

Figure 6.9: Observed 95% CL limits on $\sigma \times \mathrm{BR}/\sigma_{SM}$ as a function of the π_v proper lifetime for m_H = 125 GeV. The horizontal solid lines correspond to 15%, 5%, and 1% branching ratio.

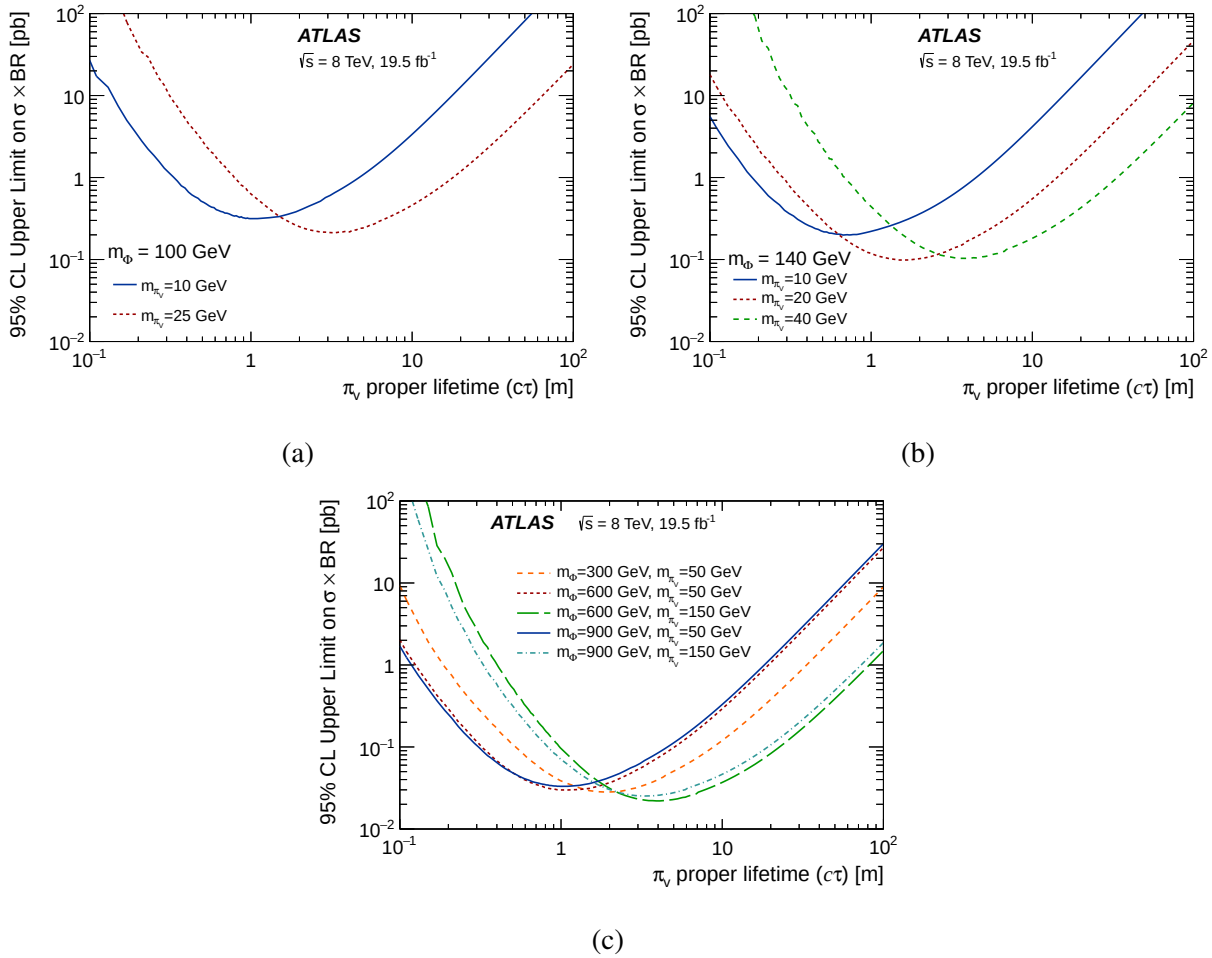

Figure 6.10: Observed 95% CL limits on $\sigma\times$ BR as a function of the long-lived particle proper lifetime.

BIBLIOGRAPHY

[1] J. Pumplin et al., *New generation of parton distributions with uncertainties from global QCD analysis*, JHEP 012 (2002) 0207.

[2] Morrissey, David E. et al., *Physics searches at the LHC*, Phys. Rept. 515 (2012) 1-113.

[3] T. S. van Albada et al., *Distribution of Dark Matter in the Spiral Galaxy NGC 3198*, Astrophysical Journal 295 (1985) 305-313.

[4] D. Curtin et al., *Exotic Decays of the 125 GeV Higgs Boson*, Phys. Rev. D90, 075004 (2014) 075004.

[5] Zhizhong Xing and Shun Zhou, *Neutrinos in Particle Physics, Astronomy and Cosmology*, "How to Generate Tiny Neutrino Masses." Springer & Zhejiang University Press. 125-129.

[6] Particle Data Group, *Review of Particle Physics*, Phys. Rev. D 86 () 1.

[7] G. Alteralli, *A QCD Primer*, arXiv:hep-ph/0204179.

[8] J. Baglio and A. Djouadi, *Higgs production at the lHC*, JHEP 03 (2011) 055.

[9] D. de Florian and M. Grazzini, *Higgs production at the LHC: updated cross sections at* $\sqrt{s} =$ 8 *TeV*, Phys. Lett. B718 (2012) 117.

[10] S. Bentvelsen, E. Laenen, and P. Motylinski, *Higgs production through gluon fusion at leading order*, NIKHEF (2005) 007.

[11] N. Cartiglia, *Measurement of the proton-proton total cross section at 2, 7, 8 and 57 TeV*, arXiv:1303.2927 [hep-ex].

[12] The LHC Higgs Cross Section Working Group, *Handbook of LHC Higgs Cross Sections: 3. Higgs Properties*, arXiv:1307.1347 [hep-ph].

[13] G. Branco et al., Phys. Rept. 516, 1 (2012), arXiv:1106.0034.

[14] S. Dimopoulos et al., *Experimental Signatures of Low Energy Gauge Mediated Supersymmetry Breaking*, Phys. Rev. Lett. 76, 3494-3497 (1996), arXiv:hep-ph/9601367.

[15] R. Barbier et al., *R-parity violating supersymmetry*, Phys. Rept. 420, 1-202 (2005), arXiv:hep-ph/0406039.

[16] D. Tucker-Smith and N. Weiner, *Inelastic Dark Matter*, Phys. Rev. D 64, 043502 (2001), arXiv:hep-ph/0101138.

[17] J. Fan, M. Reece, and J. T. Ruderman, J. High Energy Phys. 11 (2011) 012, arXiv:1105.5135.

[18] J. Fan, M. Reece, and J. T. Ruderman, J. High Energy Phys. 07 (2012) 196, arXiv:1201.4875.

[19] Y. Cui and B. Shuve, J. High Energy Phys. 02 (2015) 049, arXiv:1409.6729.

[20] The CMS Collaboration, *Observation of a new boson at a mass of 125 GeV with the CMS experiment at the LHC*, Phys. Lett. B 716 (2012) 30.

[21] The ATLAS Collaboration, *Observation of a new particle in the search for the Standard Model Higgs boson with the ATLAS detector at the LHC*, Phys. Lett. B 716 (2012) 1-29.

[22] ATLAS Collaboration, *The ATLAS Experiment at the CERN Large Hadron Collider*, JINST 3, S08003 (2008).

[23] The ATLAS Collaboration, *ATLAS detector and physics performance: Technical Design Report*, (1999).

[24] K. Assamagan et al., *Overlay for ATLAS Simulation*, ATL-SOFT-INT-2011-001 (2011).

[25] M. Cacciari, G. P. Salam, and G. Soyez, *The anti-k_t jet clustering algorithm*, JHEP **04** (2008) 063.

[26] T. Sjostrand, S. Mrenna and P. Z. Skands, PHYTHIA 6.4 *Physics and Manual*, JHEP 05 (2006) 026 arXiv:hep-ph/0603175,.

[27] T. Sjostrand, S. Mrenna and P. Z. Skands, *A Brief Introduction to PYTHIA 8.1*, Comput. Phys. Commun. 178, 852 (2008).

[28] The ATLAS Collaboration, *Triggers for displaced decays of long-lived neutral particles in the ATLAS detector*, JINST 8 (2013) P07015.

[29] The ATLAS Collaboration, *Standalone vertex finding in the ATLAS muon spectrometer*, JINST 9 (2014) P02001.

[30] D. Adams et al., *Track reconstruction in the ATLAS Muon Spectrometer with MOORE*, ATL-MUON-2003-012, 2003.

[31] The ATLAS Collaboration, *Search for a light Higgs boson decaying to long-lived weakly-interacting particles in proton-proton collisions at $\sqrt{s}$ = 7 TeV with the ATLAS detector*, PRL 108 (2012) 251801.

[32] Search for massive, long-lived particles using multitrack displaced vertices or displaced lepton pairs in pp collisions at $\sqrt{s}$ = 8 TeV with the ATLAS detector. 2015.

[33] N Pettersson, O Jinnouchi, and V Jain. An updated and extended measurement of the material in the ATLAS Inner Detector using secondary hadronic interactions in 7 TeV collisions. Technical Report ATL-COM-PHYS-2014-059, CERN, Geneva, Feb 2014.

[34] D. de Florian, G. Ferrera, M. Grazzini, and D. Tommasini, *Transverse-momentum resummation: Higgs boson production at the Tevatron and the LHC*, JHEP bf1111 (2011) 064.

[35] The ATLAS Collaboration, *Characterisation and mitigation of beam-induced backgrounds observed in the ATLAS detector during the 2011 proton-proton run*, JINST 8 (2013) P07004.

[36] D. Pomarede and M. Virchaux, *The Persint visualization program for the ATLAS experiment*, arXiv/0305057 [cs.GR].

VITA

Daniel Blackburn was born in Sioux Falls, South Dakota in 1985. He received Bachelor of Science degrees from Iowa State University in physics and chemistry. After receiving a Master of Science degree from the University of Washington in 2011, he moved to Geneva, Switzerland and joined the ATLAS experiment at CERN. Based on his research, in 2015 Daniel earned his Doctor of Philosophy in physics at the University of Washington.